Quantum dynamics and quantum information processing based on helical multiferroics

Dissertation

zur Erlangung des Doktorgrades der Naturwissenschaften
(Dr. rer. nat.)

der
Naturwissenschaftlichen Fakultät II
Chemie, Physik und Mathematik

der Martin-Luther-Universität
Halle-Wittenberg

vorgelegt von

Maryam Azimi
geboren am 21.09.1985 in Marand-Iran

1. Gutachter:	Prof. Dr. Jamal Berakdar
2. Gutachter:	Prof. Dr. Steffen Trimper
3. Gutachter:	Prof. Dr. Vitalii Dugaev

Abgabe der Dissertation: 02. August 2016
Eröffnung des Promotionsverfahrens: 03. November 2016
Öffentliche Verteidigung: 20. Dezember 2016
Vorsitzender der Promotionskommission: Prof. Dr. Kay Saalwächter

Contents

List of Abbreviations and Symbols v

List of Figures vii

List of Tables x

1. Introduction 1

2. Basics 3
- 2.1. Multiferroics 3
  - 2.1.1. Type-I multiferroics 4
  - 2.1.2. Type-II multiferroics 4
  - 2.1.3. Magnetoelectric coupling 5
  - 2.1.4. Magnetoelectric coupling in spin-spiral multiferroics 6
  - 2.1.5. One-dimensional spin-spiral multiferroics 7
- 2.2. Quantum information processing 8
  - 2.2.1. Quantum state transfer 8
  - 2.2.2. Fidelity susceptibility 9
  - 2.2.3. Fidelity of mixed states at finite temperature 10
  - 2.2.4. Entanglement measures 10
- 2.3. Quantum heat engines 13
  - 2.3.1. First law of thermodynamics and definition of work and heat in quantum systems 13
  - 2.3.2. Quantum thermodynamic processes 13
  - 2.3.3. Quantum Otto heat engine 14

3. Theoretical study of multiferroic system 17
- 3.1. The model Hamiltonian 17
- 3.2. Four spins: exact analytical solution 17
  - 3.2.1. Observing different phases in the system 20
  - 3.2.2. Fidelity susceptibilities 20
  - 3.2.3. Evaluating quantum state transfer fidelity 22
- 3.3. Large systems: numerical approach 24
- 3.4. Summary 25

4. Coherent control of the system by electric field pulses 27
- 4.1. Four spins case 28
  - 4.1.1. Quantifying the entanglement measures 30
- 4.2. Numerical simulations 34
- 4.3. Dynamical phase transition 37

4.4. Summary 42

5. Constructing quantum Otto heat engine 43
5.1. Four spins 44
  5.1.1. Magnetic and electric susceptibilities 49
  5.1.2. Efficiency of the Otto cycle 52
  5.1.3. Semi-classical limit 55
5.2. Quantum size effects 59
5.3. Summary 62

6. Superadiabatic quantum Otto heat engine 63
6.1. Introducing the technique 63
6.2. Driving the cycle 64
6.3. The output power and irreversible work 65
6.4. Summary 68

7. Conclusion and Outlook 69

A. Appendix 71

Bibliography 73

List of Publications 83

Presentations 85

Eidesstattliche Erklärung 87

Acknowledgments 89

Curriculum Vitae 91

List of Abbreviations and Symbols

FE	ferroelectric
FM	ferromagnetic
MF	multiferroic
THz	terahertz
ME	magnetoelectric
DM	Dzyaloshinskii-Moriya
NN	nearest neighbor
NNN	next nearest neighbor
PST	perfect state transfer
FS	fidelity susceptibility
VC	vector chirality
CD	counterdiabatic
ad	adiabatic
re	reversible
irr	irreversible

List of Figures

2.1. Multiferroic materials combine magnetic and ferroelectric properties. Reproduced from [20]. 3

2.2. The spin-spiral with spins rotating in the $x - z$ plane. The polarization $\vec{P}$ is produced in z direction. 6

2.3. Left: Crystal structure of $LiCu_2O_2$. Right: Schematic view of the spin configuration of $LiCu_2O_2$. [61] 8

2.4. A pictorial representation of the quantum Otto heat engine cycle with multilevel quantum system as the working substance. 15

3.1. Electric field dependence of chirality κ for the following values of the parameters: $-J_1 = J_2 = 1, B = 0.25$. 21

3.2. Electric field fidelity susceptibility for the following values of the parameters: $-J_1 = J_2 = 1, B = 0.25$. Even a weak electric field leads to a substantial reduction of the fidelity susceptibility. 22

3.3. Time and electric field dependence of the quantum state transfer fidelity for values of $J_1 = -J_2 = 1, B = 0.25$. Left panel: Fidelity for $|1\rangle \longrightarrow |2\rangle$ and $|2\rangle \longrightarrow |1\rangle$. Right panel: Fidelity for $|1\rangle \longrightarrow |3\rangle = |3\rangle \longrightarrow |1\rangle$. 23

3.4. Mean values of magnetization for different size of the system. The plot for $N = 120$ is adapted from [7]. 24

4.1. Chirality Eq. (4.15) for the following values of the parameters: $-J_1 = J_2 = 1, B = 0.25, d_0 = \wp_0 g_{ME} = 0.05, d_1 = d_2/0.1$. 30

4.2. Two-tangle in case of two-excitations ground state $|\phi_7\rangle$ for the following values of the parameters: $-J_1 = J_2 = 1, B = 0.25, d_0 = \wp_0 g_{ME} = 0.05, d_1 = d_0/0.1$. 32

4.3. Von Neumann entropy in case of two-excitations ground state $|\phi_7\rangle$ for the following values of the parameters: $-J_1 = J_2 = 1, B = 0.25, d_0 = \wp_0 g_{ME} = 0.05, d_1 = d_0/0.1$. 32

4.4. Von Neumann entropy in case of two-excitations ground state $|\phi_7\rangle$ for different values of d_1. 33

4.5. Time dependence of chirality(up panel), two-tangle(down left panel) and von Neumann entropy(down right panel) for N=8, with the two-excitations initial state. The parameters are: $-J_1 = J_2 = 1, B = 0.25, d_0 = \wp_0 g_{ME} = 0.05, d_1 = d_0/0.1$. 34

4.6. Von Neumann entropy in case of $N = 8$, with the two-excitations ground state for different values of d_1. 35

4.7. Von Neumann entropy in case of $N = 20$, with $N/2$-excitations ground state for different values of d_1. 35

4.8. Time dependence of the two-tangle (left panel) and the von Neumann entropy (right panel) for $N = 18, 20, 22, 30, 40$. In all cases the system is in a two-excitations ground state. The strength of the pulse is $d_1 = 0.5$. The spin-exchange couplings and initial electric-field strength are $-J_1 = J_2 = 1, d_0 = \wp_0 g_{ME} = 0.05$ respectively. Adapted from [105]. . . 36
4.9. Zeros of $\theta_k = it_k$ in case of 4-spins system with two-excitations ground state for $k = -4, -3, ..., 3$ and $J_1 = -J_2 = -1.0, B = 0.25, d0 = 0.05$. Green squares, blue circles, black diamonds, and red points correspond to $d_1 = 2.5, d_1 = 3.5, d_1 = 5.49$, and $d_1 = 100$ respectively. 39
4.10. Rate function and Schmidt gap in 4-spins system with two-excitations ground state. The parameters are $-J_1 = J_2 = 1, d_0 = \wp_0 g_{ME} = 0.05$. For left panel $d_1 = 5.49$ and for right panel $d_1 = 100$ correspond to black diamond points and red points in Fig. 4.9 respectively. 40
4.11. Left panel: Zeros of $\theta_k = it_k$ in the case of applied pulses to 4-spins system with two-excitations ground state for $k = -4, -3, ..., 3$ and $J_1 = -J_2 = -1.0, B = 0.25, d0 = 0.001$. Green squares, red circles, black diamonds correspond to $d_1 = 0.3, d_1 = 0.5554$, and $d_1 = 0.8$ respectively. Right panel: Rate function and Schmidt gap for $d_1 = 0.5554$ (red circles). 40
4.12. Left panel: The rate function and the Schmidt gap for a periodic chain of size $N = 18$. The parameters are $J_2 = -J_1 = 1, d_1 = 2.34, d_0 = 0.098$. Right panel: The rate function and the Schmidt gap for a periodic chain of size $N = 22$ for the parameters $J_2 = -J_1 = 1, d_1 = 0.44, d_0 = 0.057$. The peaks of the rate function at time $t'' \approx 9.41, 28.36, 47.20, ...$ correspond to the dynamical phase transitions. The inset shows a zoom into the cusp region at one of the non-analytic point. Adapted from [105]. 41

5.1. Scheme of the quantum Otto cycle based on a spin-spiral multiferroic chain. Reproduced from [118]. 43
5.2. Chirality as a function of the temperature for different values of the electric field. The parameters are: $-J_1 = J_2 = 1, B = 0.25$. 44
5.3. Chirality as a function of B for the parameters $-J_1 = J_2 = 1, \wp = 0.5, T = 10$. 45
5.4. Two-tangle as a function of the electric field $\wp$ for different temperatures $T = 2$(red cross line), $T = 5$(blue solid line), $T = 10$(black triangle line). The parameters are: $-J_1 = J_2 = 1, B = 0.25$. 47
5.5. Two-tangle as a function of the temperature for different values of the electric field $\wp = 0.5$(blue solid line), $\wp = 3$(black triangle line), $\wp = 5$(red cross line). The parameters are: $-J_1 = J_2 = 1, B = 0.25$. The threshold temperatures are $T_c = 1.9, \quad T_c = 2.3, \quad T_c = 2.9$, respectively. 47
5.6. One-tangle as a function of the temperature for different values of the electric field $\wp = 0.5$(blue solid line), $\wp = 3$(black triangle line), $\wp = 5$(red cross line). The parameters are: $-J_1 = J_2 = 1, B = 0.25$. . 48

5.7. One-tangle as a function of the electric field $\wp$ for different temperatures $T = 2$(red cross line), $T = 5$(blue solid line), $T = 10$(black triangle line). The parameters are: $-J_1 = J_2 = 1, B = 0.25$. 48
5.8. Ratio between two- and one-tangle as a function of the external electric field for the following values of the parameters $-J_1 = J_2 = 1, B = 0.25, T = 1.9$. 49
5.9. One- and two-tangle as a function of the magnetic filed B. The parameters are: $-J_1 = J_2 = 1, T = 2, \wp = 5.5$. 49
5.10. Magnetic susceptibility as a function of the temperature for different values of the electric field $\wp = 0.5$(blue solid line), $\wp = 3$(black triangle line), $\wp = 5$(red cross line). The parameters are: $-J_1 = J_2 = 1, B = 0.25$. 52
5.11. Electric susceptibility as a function of the temperature for different values of the electric field $\wp = 0.5$(blue solid line), $\wp = 3$(black triangle line), $\wp = 5$(red cross line). The parameters are: $-J_1 = J_2 = 1, B = 0.25$. 52
5.12. The efficiency of the quantum adiabatic Otto cycle as a function of the modulation of the electric field amplitude for the following values of the parameters $-J_1 = J_2 = 1,\ B = 0.25,\ \wp_1 = 0.5,\ T_H = 10,\ T_L = 2$. 53
5.13. The efficiency of the quantum Otto cycle as a function of the modulation of the electric field amplitude for the following values of the parameters $-J_1 = J_2 = 1,\ B = 0.25,\ T_H = 10,\ T_L = 2$. 54
5.14. The efficiency of the quantum Otto cycle as a function of the pair entanglement for the following values of the parameters $-J_1 = J_2 = 1,\ B = 0.25,\ \wp_1 = 2.5$. 55
5.15. Contour plot of entropy as a function of the modulation of the electric field amplitude and the temperature. 57
5.16. The semi-classical efficiency η_{sc} as a function of the electric field $\wp$ and temperature difference between hot and cold baths $\Delta T = T_H - T_L$ for $T_L = 30,\ \wp_1 = 0.5$. 58
5.17. Ratio between two- and one-tangle as a function of the external electric field for the system of 8 spins and the following values of the parameters $-J_1 = J_2 = 1, B = 0.25, T = 1.9$. 59
5.18. Magnetic susceptibility as a function of the temperature for the system of 8 spins and different values of the electric field $\wp = 0.5$(blue solid line), $\wp = 3$(black triangle line), $\wp = 5$(red cross line). The parameters are: $-J_1 = J_2 = 1, B = 0.25$. 59
5.19. Electric susceptibility as a function of the temperature for the system of 8 spins and different values of the electric field $\wp = 0.5$(blue solid line), $\wp = 3$(black triangle line), $\wp = 5$(red cross line). The parameters are: $-J_1 = J_2 = 1, B = 0.25$. 60
5.20. The efficiency of the quantum Otto cycle as a function of the system size N for three different values of the electric field. The other parameters are $-J_1 = J_2 = 1,\ B = 0.25,\ T_H = 10,\ T_L = 2$. 60

6.1. Left panel: The work mean square fluctuations for $B = 0.25$. Right panel: The output power. The other considered parameters are $J_1 = -1, J_2 = 1, d_0 = 5, \epsilon = 1, T_H = 15, T_L = 2$. 66

6.2. $\langle W_{\mathrm{irr}} \rangle$ for the values of parameters $J_1 = -1, J_2 = 1, B = 0.25, d_0 = 5, \epsilon = 1, \tau = 3, T_H = 15, T_L = 2$. 67

List of Tables

2.1. Classical and quantum thermodynamic processes. Here U, V, T, P are indicated to the internal energy, volume, temperature and pressure of the working substance respectively. E_n, P_n are energy levels and occupation probabilities. 15

1. Introduction

Materials characterized by both ferroelectric and ferromagnetic features are known as multiferroics (MF) [1]. Since 1960s, these materials have been shown to have a magnetoelectric response, but only few multiferroics were found and in general the coupling between magnetic and ferroelectric order parameters was weak. With the capabilities of modern material design techniques it has been possible to synthesize nanostructured MF materials and multilayer systems that show a considerable magnetoelectric coupling, enabling so a steering of magnetism with electric fields or electric polarization with magnetic fields [2, 3]. The electric field control of magnetization has received particular attention as it renders possible new spintronic device concepts with low power consumption [4–6]. A relatively less researched aspect is the use of MF nanostructures for quantum information processing. As shown in this thesis MF are excellently suited for this purpose, as they show a multitude of phenomena of a quantum nature, such as polarization controlled spin helical structures and magnetoelectrically controlled quantum phases [7]. Encouraging in this respect is the experimental advance in multiferroic quantum spin chains and nanostructures.

In this thesis, we focus on one dimensional spin chain as a typical example of frustrated spin systems and investigate the properties and applications of such a system. The most studied examples, $LiCuVO_4$ and $LiCu_2O_2$ demonstrated a fascinating effect of the strong quantum fluctuations due to the spin-1/2 nature, as evidenced by recent neutron scattering experiments [8].

The general idea to use spins as permanently coupled quantum systems for quantum information processing was put forward by S. Bose in 2003. The main goal was to use a finite spin chain as a data bus. Later on, many significant studies of propagation of quantum states through spin chains were conducted. It was shown that, perfect state transfer can be achieved in some specially designed systems [9–12]. However, all of these proposals have concentrated on the ideal spin chains with only nearest neighbor couplings. A great deal of attention has also been given to the study of entanglement in such systems. Entanglement is inherent to quantum systems and is at the heart of quantum information and quantum computation research.

On the other hand, with the fast growing field of nanotechnology, which promises to develop portable materials and devices as well as a chance to exploit the novel properties of nanoscale physical systems, questions related to the thermodynamical properties are gaining increased attention. Several theoretical schemes are proposed for Brownian motors [13, 14], refrigerators [15] and quantum heat engines. Additionally the application of the laws of thermodynamics for finite systems, is the subject of intensive debates [16, 17]. Quantum thermodynamics investigate the physical phenomena at the crossover of quantum mechanics and thermodynamics. One of the most interesting topics is that to what extent standard classical thermodynamic cycles such as Carnot or Otto cycles can be reformulated for quantum systems. A key issue, thereby is the difference between thermodynamic and quantum adiabatic processes. For example, a thermodynamical adiabatic process does not necessarily mean that the occupation probabilities are kept invariant during adiabatic transitions. Naturally, thermodynamical adiabatic processes are described in terms of the entropy conservation and the isolation of the system from the heat exchange with the thermal bath. While in the case of quantum adiabatic process an essential requirement is that the population distributions remain unchanged. Therefore, quantum adiabaticity is a stricter requirement than the thermodynamic adiabaticity. The adiabatic quantum process is also adiabatic in the thermodynamic sense, however the opposite statement is not true in general. Thus, quantum adiabaticity entails a relatively low output power from a slowly operating quantum engine, unless the energy spectrum of the working substance has nodal crossing points, however, this is not a generic feature of realistic physical systems. In order to avoid Landau Zener transitions during an adiabatic segment of the cycle, the control parameters should vary slowly [18]. The subtlety of quantum engines is related to the internal connection between essentially quantum phenomena such as entanglement and the thermodynamic characteristics of the cycle [19]. Therefore, the choice of the working substance for the operating quantum engine is an important issue. This is where we think that MF quantum structures can serve as a useful working substance with external knobs, such as electric and magnetic fields to control the thermodynamic cycle.

A desirable feature of a quantum heat engine is not a high efficiency and a slow cycle, but rather a good efficiency at maximal power. To achieve it, a quantum thermodynamic cycle should be carried out within a finite time. In this respect the concept of shortcuts to quantum adiabaticity is useful. This technique quenches the effect of inter-level transitions that are of a pure quantum origin.

The present thesis consists of five main parts. The first part entitled Basics, introduces multiferroics as needed for the application in the thesis. The concepts of quantum information processing, entanglement measures and fidelity are summarized for the use in the following chapters. In addition, we discuss quantum heat engines with a focus on quantum Otto heat engine. In the second part the Hamiltonian of the one dimensional frustrated spin chain is described and the system is analyzed both analytically and numerically. The third part is devoted to imposing ultrashort terahertz (THz) pulses on the system and obtaining the time evolution of the system. The dynamics of different quantities that are relevant to quantum information processing are analyzed. Studying a quantum Otto heat engine on the basis of a helical multiferroic chain is done in chapter five. It is shown that the steering of the cycle by an external electric field which is coupled to the electric polarization can be achieved. In chapter six the special technique of shortcuts to quantum adiabaticity is presented, to obtain a finite output power of the quantum Otto heat engine. The final chapter contains a summary of the current work and an outlook.

2. Basics

2.1. Multiferroics

Multiferroic materials commonly are known as materials with combined ferroelectric and ferromagnetic properties. They are interesting due to the magnetoelectric (ME) effect that allows control of the induced magnetization (M) by applying an electric field (E) or controlling electric polarization (P) by applying a magnetic field (H). See Fig. 2.1.

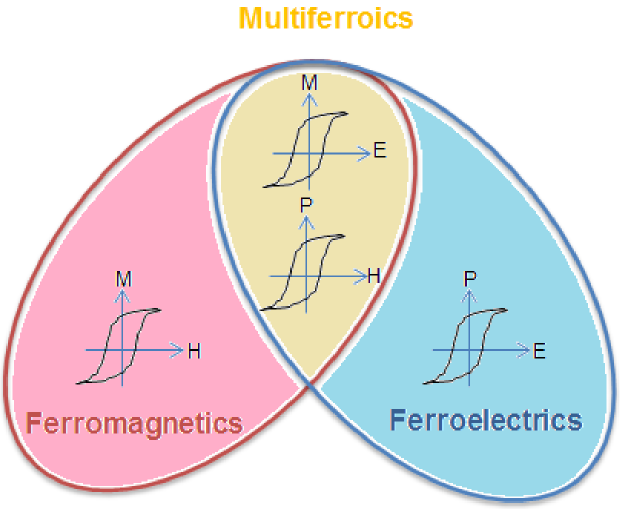

Figure 2.1. – Multiferroic materials combine magnetic and ferroelectric properties. Reproduced from [20].

The magnetoelectric effect was observed by Röntgen in 1888 [21]. He noticed that a moving dielectric body in an electric field, was changed to magnetized body. The reverse effect i.e. the polarization of a moving dielectric body in a magnetic field, was detected by Wilson in 1905 [22]. However, these two observations were not intrinsic effects of the materials. In 1894 Curie predicted the possibility of an intrinsic magnetoelectric effect of crystals based on symmetry considerations [23]. Many decades later, Landau and Lifshitz realized that the time reversal symmetry has to be considered when studying the magnetoelectric behavior [24]. Dzyaloshinskii predicted the occurrence of magnetoelectric coupling in Cr_2O_3 [25] which was confirmed experimentally by Astrov [26] by measuring the electric field induced magnetization in Cr_2O_3 [26]. After ten years of theoretical and experimental works on magnetoelectric effect the summary of the efforts were published in a book by O'Dell in 1970 [27]. However, due to the difficulties of using the magnetoelectric coupling in useful applications, researches in this field declined for about two decades. The impressive revival of interest was started again when artificially grown composite multiferroics became available showing a sizable magnetoelectric coupling and further theoretical works pointing to systematically combine materials to achieve new functionalities [28]. Also the discovery of new mechanisms of ferroelectricity in a novel class of multiferroics $TbMnO_3$ [29], $TbMn_2O_5$ [30], YMn_2O_3 [31] and $Ni_2V_3O_8$ [32] gave a new impetus to the field. The general discussion of several features of the multiferroics can be found in [33–37].

2.1.1. Type-I multiferroics

The type-I multiferroics are materials with different origins of ferroelectricity and magnetism and these two effects appear quite independent of each other, however there is a small coupling between them. In the following, the most common multiferroics of type-I are reviewed.

Compounds with provskite structure ABO_3: The transition metal provskite are some of the most promising multiferroic materials in which the ferroelectricity is usually generated by transition metal compounds with empty d-shells (d^0). The important ferroelectrics such as $BaTiO_3$ and $(Pb,Zr)TiO_3$ belong to this group. In $BaTiO_3$ as an example, the empty d-shells of the transition metal Ti^{4+}, stabilizes the strong covalent bonding with the surrounding oxygen $2p$ orbitals and the ferroelectricity is produced by shifting of the Ti^{4+} cation from the center of O_6 octahedral towards oxygen anions [37, 38].

Compounds with lone pairs mechanism: In materials like $BiFeO_3$ and $BiMnO_3$, the existence of $6s$ lone pair of Bi^{3+} induces the ferroelectricity [39, 40]. In other words, those ions with two valence electrons cause a shifting of the Bi^{3+} from the centrosymmetric position with respect to the surrounding oxygen ions and induce ferroelectricity, i.e. the ferroelectricity is due to the A-site cation. This is unlike the case of perovskite ferroelectrics like $BaTiO_3$, $(Pb,Zr)TiO_3$ where the ferroelectricity is caused due to the B-site cation shift [41].

Compounds with geometric ferroelectricity: Hexagonal manganites with the general formula $RMnO_3$ where R is a small rare earth element, such as Y, Ho, Lu and Yb, violating the d^0-ness, belong to this group. In these structures the ferroelectricity is induced by tilting the trigonal biprymids MnO_5 resulting in large R-O dipole moments and forming a close packed structure. Such a rotation of MnO_5 breaks the inversion symmetry and yields ferroelectricity [31, 42, 43].

An extended discussion of type-I multiferroics can be found in [20, 44].

2.1.2. Type-II multiferroics

The type-II multiferroics are materials in which the ferroelectricity is induced by magnetic ordering. In this class of multiferroics the coupling between the magnetism and ferroelectricity is especially strong and making them a suitable candidate for various applications. Based on the mechanism of multiferroic behavior, this type of multiferroics can be classified into two groups. The first group are those in which the ferroelectricity is induced by a particular type of magnetic spiral and the second one are those in which the ferroelectricity is present in the collinear magnetic structures. In the following we review these two groups.

Spiral multiferroics: Most of the well known type-II multiferroics belong to this group. In 2003, Kimura et al., discovered the presence of spontaneous polarization induced by spin-spiral structure on the Mn sublattice in $TbMnO_3$ [29]. This material shows different magnetic structures. It is an incommensurate antiferromagnetic phase with sinusoidal spin density wave propagation between 27 and 42 K. Below 27 K, magnetic structure changes from sinusoidal to commensurate helicoidal and the non-zero polarization appears [45]. The orientation of the polarization in the crystal lattice can be controlled by applying an external magnetic field [46]. A similar situation is specified in recently found multiferroics with different structures like $Ni_2V_3O_8$ [32], $CuFeO_2$ [47], $MnWO_4$ [48], CuO [49]. The common feature to this type of multiferroics is the presence of magnetic frustration, which results from the competition between ferromagnetic nearest neighbor and antiferromagnetic next nearest neighbor interactions inducing the spiral magnetic structure [50].

Multiferroics with collinear magnetic structures: Along with the progressive growth of spiral multiferroics, another type of multiferroics with collinear magnetic structures have also received a great attention. In this class of multiferroics, ferroelectricity appears in collinear magnetic structures. In these materials, the polarization emerges as a result of exchange interactions. The most important examples of this class are $TbMn_2O_5$ [30], Ca_3CoMnO_6 [51].

2.1.3. Magnetoelectric coupling

According to Landau theory the magnetic and electric order parameters in a system with magnetoelectric coupling can be described with the free energy

$$\begin{aligned} F(E,H) =& F_0 - P_i^s E_i - M_i^s H_i - \frac{1}{2}\epsilon_0\epsilon_{ij}E_iE_j - \frac{1}{2}\mu_0\mu_{ij}H_iH_j \\ & - \alpha_{ij}E_iH_j - \frac{1}{2}\beta_{ijk}E_iH_jH_k - \frac{1}{2}\gamma_{ijk}H_iE_jE_k - \dots , \end{aligned} \tag{2.1}$$

where F_0 is the ground state free energy and E, H are the electric and magnetic fields respectively. P_i^s and M_i^s are the spontaneous polarization and magnetization in the system. Here ϵ and μ are the dielectric permitivity and magnetic premeability respectively. In the sixth term α_{ij} describes the linear magnetoelectric coupling while the last two terms with β_{ijk} and γ_{ijk}(the third-order tensors) stand for the higher order magnetoelectric coupling. The polarization $P_i(E,H)$ and magnetization $M_i(E,H)$ can be obtained after differentiating of Eq. (2.1) with respect to the electric and magnetic fields respectively

$$\begin{aligned} P_i(E,H) &= -\frac{\partial F}{\partial E_i} = P_i^s + \epsilon_0\epsilon_{ij}E_j + \alpha_{ij}H_j + \frac{1}{2}\beta_{ijk}H_jH_k + \gamma_{ijk}H_iE_j + \dots , \\ M_i(E,H) &= -\frac{\partial F}{\partial H_i} = M_i^s + \mu_0\mu_{ij}H_j + \alpha_{ij}E_j + \beta_{ijk}H_jE_i + \frac{1}{2}\gamma_{ijk}E_jE_k + \dots . \end{aligned} \tag{2.2}$$

2.1.4. Magnetoelectric coupling in spin-spiral multiferroics

The mechanism of magnetically induced ferroelectricity in frustrated structures has been studied by Katsura et al. using a microscopic approach [52], and Mostovy using a phenomenological approach [53]. The microscopic mechanism considers the spin-orbit coupling in the superexchange interaction between nearest neighbor spins. The induced polarization is proportional to the vector product of the spin current $\vec{J}(\vec{J} \propto \vec{S}_i \times \vec{S}_j)$ and the unit vector $\vec{e}_{ij}$ connecting the two neighboring spins $\vec{S}_i$ and $\vec{S}_j$

$$\vec{P} \propto \vec{e}_{ij} \times \left[\vec{S}_i \times \vec{S}_j\right] \tag{2.3}$$

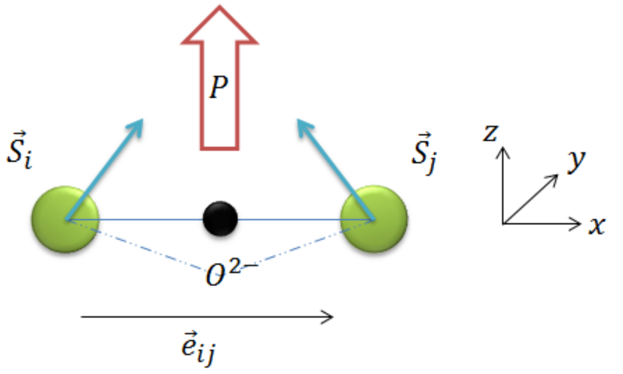

Figure 2.2. – The spin-spiral with spins rotating in the $x - z$ plane. The polarization $\vec{P}$ is produced in z direction.

This effect is sometimes called the inverse Dzyaloshinskii-Moriya (DM) interaction, which was proposed by Sergienko et al. [54]. In this approach the oxygen ion is displaced between two localized magnetic moments via the electronic interaction.
In the phenomenological approach, the form of the coupling between the electric polarization and magnetization is obtained using general symmetry considerations [25]. While the polarization is unaffected by time reversal $t \longrightarrow -t$, the magnetization is reversed. Therefore the lowest order magnetoelectric coupling term must be quadratic in M. On the other hand, in order to preserve the spatial inversion $r \longrightarrow -r$, upon which the magnetization remains unaffected and the polarization changes the sign,

the coupling of the polarization to the magnetization can be linear in P and have one gradient of M. Then the third order magnetoelectric coupling term in Landau free energy is allowed [53, 55].

$$\Phi_{ME}(\mathbf{r}) = \mathbf{P} \cdot \{\gamma \cdot \nabla(\mathbf{M}^2) + \gamma'[\mathbf{M}(\nabla \cdot \mathbf{M}) - (\mathbf{M} \cdot \nabla)\mathbf{M}] + \dots\}\,, \tag{2.4}$$

where $\mathbf{r}$, $\mathbf{P}$ and $\mathbf{M}$ are spatial coordinate, polarization and magnetization. γ and γ' are the coupling coefficients. The first term in Eq. (2.4) is valid when $\mathbf{P}$ is assumed to be independent of the spatial coordinate $\mathbf{r}$. Assuming that in the absence of magnetism, the system shows no instability towards ferroelectricity, we are allowed to keep only the quadratic term in the electric part of the potential $\Phi_e(P) = \frac{P^2}{2\chi_e}$, where χ_e is the dielectric susceptibility in the absence of magnetization. In the case of cubic crystals, the magnetically induced electric polarization is derived by minimizing the free energy with respect to $\mathbf{P}$

$$\mathbf{P} = \gamma'\chi_e[(\mathbf{M} \cdot \nabla)\mathbf{M} - \mathbf{M}(\nabla \cdot \mathbf{M})]\,. \tag{2.5}$$

The spin-spiral structure can be described by

$$\mathbf{M} = S_1\mathbf{e}_1 \cos(Q \cdot x) + S_2\mathbf{e}_2 \sin(Q \cdot x), \tag{2.6}$$

where $\mathbf{e}_1$ and $\mathbf{e}_2$ are the unit vectors and Q is the propagation vector of the spiral. The polarization is orthogonal to spin rotation axis($\mathbf{e}_3 = \mathbf{e}_1 \times \mathbf{e}_2$) and wave vector Q

$$\mathbf{P} = \gamma'\chi_e S_1 S_2(\mathbf{e}_3 \times \mathbf{Q})\,. \tag{2.7}$$

This equation is analogous to Eq. (2.3) where P is proportional to the cross product of the spins. We can deduce that the Katsura et al. approach is a microscopic interpretation of Mostovoy phenomenological model. Therefore, the spin-orbit interaction is regarded as the origin of the coupling between the ferroelectric and magnetic orders in these kind of multiferroics.

2.1.5. One-dimensional spin-spiral multiferroics

Here we are dealing with One-dimensional spin-spiral spin chain with competing nearest neighbor (NN) ferromagnetic interaction and next nearest neighbor (NNN) antiferromagnetic interaction resulting in frustrated spiral spin system.

One of the most reported One-dimensional spiral magnetic ferroelectrics is $LiCu_2O_2$ [56–60]. As shown in Fig. 2.3 left panel, $LiCu_2O_2$ has an orthorhombic crystal structure. The Cu^{2+} ions carrying spin $S = \frac{1}{2}$ locate in the center of CuO_4 squares and form spin chains along the b-axis, See Fig. 2.3 right panel. The chains of Cu^{2+} are well separated by planar chains of Li^+ ions and interpolation layers of Cu^+ ions. Due to the frustration, the spin-spiral structure is produced below $T \sim 23\,\mathrm{K}$. The spontaneous electric polarization has been realized along the c-axis [60].

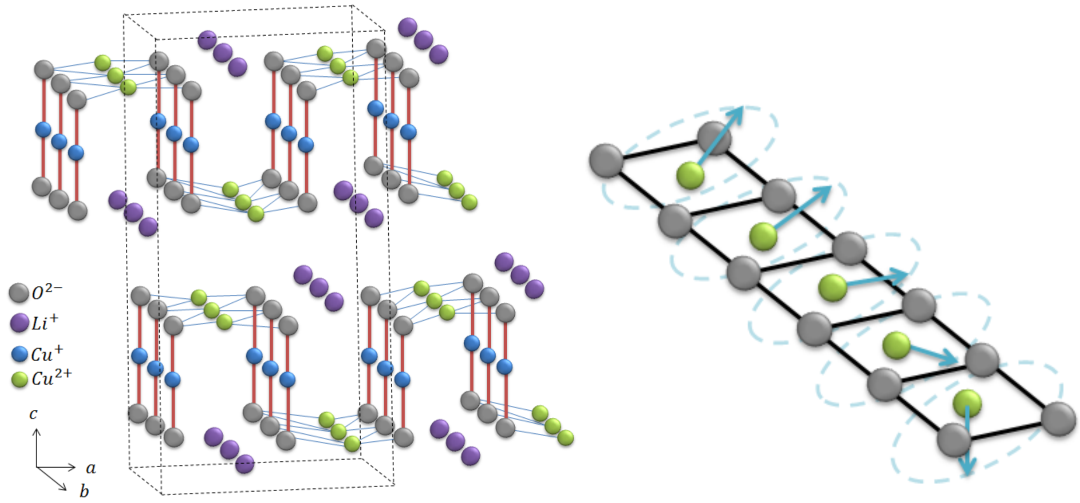

Figure 2.3. – Left: Crystal structure of $\mathrm{LiCu_2O_2}$. Right: Schematic view of the spin configuration of $\mathrm{LiCu_2O_2}$. [61]

2.2. Quantum information processing

Quantum information theory is dealing with the transmission, storage and processing of information using quantum mechanical systems [62]. So the mathematical description of quantum systems is completely different from classical systems. Dissimilar to the classical case, most of the information is stored in the form of correlations in the systems. In the following some main concepts in quantum information theory are reviewed.

2.2.1. Quantum state transfer

One of the most important tasks in quantum information processing is transferring a quantum state from one point to another. Among the several quantum state transfer protocols, the schemes based on the spin chains with controllable coupling strengths are particularly attractive for short distance communication [63–69]. The reason behind this is that in spin systems, quantum phase transitions and their relations to entanglement can be well studied [70–72]. A basic operation consists of encoding the state at one end of the spin chain and propagating it for a specific amount of time to the other end of the chain. For a linear chain of N spins with the Hamiltonian H, the state $|\boldsymbol{i}\rangle = |00...0\underbrace{1}_{i}0...0\rangle$ is defined as a state in which the spin at site i is flipped to the state $|1\rangle$. The remaining $N-1$ spins are in the state $|0\rangle$. In this notation the state $|0\rangle$ and $|1\rangle$ denote the spin-up and the spin-down respectively. Consider that a quantum state $|\psi\rangle_a = \alpha|0\rangle_a + \beta|1\rangle_a$ with $|\alpha|^2 + |\beta|^2 = 1$ is created on the site a. So that the state of the total system at the initial time is $|\psi(t=0)\rangle = \alpha|\mathbf{0}\rangle + \beta|\boldsymbol{a}\rangle$, with $|\mathbf{0}\rangle = |00...0\rangle$ and $|\boldsymbol{a}\rangle$ stands for the spin at the site a is flipped. Now the Hamiltonian of the system is switched on and the system is allowed to evolve under the unitary operator $U(t) = e^{-iHt}$ for a given time $t = t_0$. The final state of the system is obtained by

$$|\psi(t=t_0)\rangle = \alpha|\mathbf{0}\rangle + \beta\sum_{i=1}^{N} f_{ia}(t_0)|\boldsymbol{i}\rangle, \tag{2.8}$$

where $f_{ia}(t_0) = \langle\boldsymbol{i}|e^{-iHt}|\boldsymbol{a}\rangle$ is the transition amplitude between two sites. The average fidelity of quantum communication is defined by [63]

$$F(t_0) = \frac{|f_{ia}(t_0)|\cos\gamma}{3} + \frac{|f_{ia}(t_0)|^2}{6} + \frac{1}{2}, \quad \gamma = arg\{f_{ia}(t_0)\}. \tag{2.9}$$

This quantity can be interpreted as a signature of the perfect state transfer (PST) between two points, i.e. when $|F(t_0)| = 1$, the perfect state transfer is obtained which means that the output is identical to the input and the chance of distinguishing them by any quantum measurement tends to zero. If $|F(t_0)| < 1$, the state transfer is imperfect.

2.2.2. Fidelity susceptibility

Fidelity susceptibility (FS) defines the sensitivity of the system with respect to changes of the driving parameters of the Hamiltonian like the external driving fields [73–76]. Consider the general Hamiltonian of a quantum system with a driving parameter λ as

$$\hat{H}(\lambda) = \hat{H}_0 + \lambda\hat{H}_I. \tag{2.10}$$

Changing λ, leads to a phase transition in the system because of the competition between $\hat{H}_0$ and $\hat{H}_I$. The eigenstates of the system $|\psi_n(\lambda)\rangle$ satisfy

$$\hat{H}(\lambda)|\psi_n(\lambda)\rangle = E_n(\lambda)|\psi_n(\lambda)\rangle. \tag{2.11}$$

Changing the driving parameter λ as $\lambda \longrightarrow \lambda + \delta\lambda$ where $\delta\lambda$ is so small, we can use the perturbation theory. Therefore the first order perturbation for the ground state $|\psi_0(\lambda+\delta\lambda)\rangle$ gives

$$\begin{aligned} &|\psi_0(\lambda+\delta\lambda)\rangle = |\psi_0(\lambda)\rangle + \delta\lambda\sum_{n\neq 0}\frac{H_{n0}(\lambda)|\langle\psi_n(\lambda)\rangle}{E_0(\lambda)-E_n(\lambda)}, \\ &H_{n0}(\lambda) = \langle\psi_n(\lambda)|H_I|\psi_0(\lambda)\rangle. \end{aligned} \tag{2.12}$$

The fidelity can be defined as the overlap between the ground state wavefunctions at two different values of the driving parameter λ

$$F(\lambda,\delta\lambda) = |\langle\psi_0(\lambda)|\psi_0(\lambda+\delta\lambda)\rangle|. \tag{2.13}$$

Since generally in many body systems the fidelity $F(\lambda, \delta\lambda)$ vanishes exponentially with the system size, it's more suitable to study the change of its logarithm with respect to the driving parameter λ. From this point the concept of fidelity susceptibility is introduced as

$$\chi_F(\lambda) = -\frac{\partial^2 \ln F}{\partial \delta\lambda^2}\bigg|_{\delta\lambda=0}. \tag{2.14}$$

The fidelity susceptibility exhibits a maximum or even diverges at the critical point which indicates a quantum phase transition. It can be finally written as

$$\chi_F(\lambda) = \sum_{n\neq 0} \frac{|\langle\psi_n(\lambda)|H_I|\psi_0(\lambda)\rangle|^2}{[E_n(\lambda) - E_0(\lambda)]^2}. \tag{2.15}$$

2.2.3. Fidelity of mixed states at finite temperature

The mixed state fidelity at finite temperature, which characterizes a second order thermal phase transition is defined in the following way [77, 78]

$$F_\lambda(\beta, \lambda_0, \lambda_1) = \mathrm{Tr}\sqrt{\sqrt{\hat{\rho_0}}\hat{\rho_1}\sqrt{\hat{\rho_0}}}, \tag{2.16}$$

where $\hat{\rho_0}(\beta, \lambda_0), \hat{\rho_1}(\beta, \lambda_1)$ are the density matrices of the system corresponding to slightly change of the control parameters $\lambda_1 = \lambda_0 + \delta\lambda$ and $\beta = \frac{1}{k_B T}$. This expression can be simplified to the following form

$$F_\lambda(\beta, \lambda, \lambda + \delta\lambda) = \exp\left[-\frac{\beta(\delta\lambda)^2}{8}\chi(\lambda)\right], \tag{2.17}$$

where $\chi(\lambda) = -\frac{\partial^2 F}{\partial \lambda^2}$ is the susceptibility to the corresponding external driving parameter λ at constant temperature and $F = -k_B T \ln Z(k_B T)$ is the free energy of the system and $Z(k_B T)$ is the partition function.

2.2.4. Entanglement measures

Entanglement is an important resource in quantum information processing and has been widely applied in many aspects of it like quantum computation [79], quantum cryptography [80] and telportation [81, 82].

A quantum mechanical system consisting of two parts A and B and having the density matrix ρ is entangled if ρ cannot be written as a direct product of the density operators $\rho_A^{(i)}$, $\rho_B^{(i)}$ of the sub-systems A and B, i.e. one cannot write

$$\rho = \sum_i p_i \rho_A^{(i)} \otimes \rho_B^{(i)}, \tag{2.18}$$

where $p_i \geq 0$ and $\sum_i p_i = 1$.

In the following, some important entanglement measures are defined.

One- and two-tangles: One of the mostly used measures to quantify entanglement in many-body systems is one-tangle which evaluates the nonlocal correlations in the system. It is defined as follows

$$\tau_A = 4\mathrm{det}\rho_A \tag{2.19}$$

Here $\rho_A = \mathrm{Tr}_{s\neq A}(\rho)$ is the one site reduced density matrix after tracing out the states of all sites $s \neq A$.

Another measure of entanglement which contains the local information in the system is the concurrence. The concurrence is known as entanglement between two sites of the system and is obtained from the two-qubit reduced density matrix after all the spins except those at two certain positions have been traced out. The general definition of the concurrence is

$$C_{nm} = \max(0, \sqrt{R_{nm}^{(1)}} - \sqrt{R_{nm}^{(2)}} - \sqrt{R_{nm}^{(3)}} - \sqrt{R_{nm}^{(4)}}), \tag{2.20}$$

where $R_{nm}^{(\alpha)}$, $\alpha = 1, 2, 3, 4$ are the eigenvalues of the matrix

$$R_{nm} = \rho_{nm}^R(\sigma_1^y \otimes \sigma_2^y)(\rho_{nm}^R)^*(\sigma_1^y \otimes \sigma_2^y), \tag{2.21}$$

in decreasing order $R_{nm}^{(1)} \geq R_{nm}^{(2)} \geq R_{nm}^{(3)} \geq R_{nm}^{(4)}$ and ρ_{nm}^R is the reduced density matrix of the system of two spins obtained from the density matrix of the system ρ. The asterisk in density matrix indicates the complex conjugation and σ^y is a Pauli matrix. Now we can define the more informative and universal quantity called the two-tangle τ_2, which contains information on the total pair correlations in the spin chain as

$$\tau_2 = \sum_m^L C_{nm}^2 \tag{2.22}$$

Where L denotes the number of spins.

Von Neumann entropy: The other measure of the entanglement, which also quantifies multiparticle entanglement, is von Neumann entropy. It is defined as

$$S = -\mathrm{Tr}[\rho \log_2 \rho] \tag{2.23}$$

This quantity serves as the connection between quantum statistical mechanics and thermodynamics when ρ is the Gibbs state described by $\rho = e^{-\beta H}/Z$. If λ_i are the eigenvalues of the density matrix ρ, then von Neumann entropy reads

$$S = -\sum_i \lambda_i \log_2 \lambda_i. \tag{2.24}$$

Some interesting properties of von Neumann entropy are

- It is always positive. The von Neumann entropy is zero if and only if the state is pure.
- In a d dimensional Hilbert space the maximum of the von Neumann entropy is $\log_2 d$.
- For a pure composite system AB, S(A) = S(B).
- It is invariant under unitary transformation $S(\rho) = S(U\rho U^{\dagger})$.
- Additivity, i.e. $S(\rho_A \otimes \rho_B) = S(\rho_A) + S(\rho_B)$.
- Suppose p_i are probabilities, then $S(\sum_i p_i\rho_i) = H(p_i)+\sum_i p_i S(\rho_i)$, where $H(p_i)$ is the Shannon entropy of the distribution p_i.

For more information about different local and nonlocal entanglement measures one can refer to the references [83–90].

2.3. Quantum heat engines

The classical heat engine played a crucial role in the development of the classical thermodynamics. Similarly the quantum heat engine serves also as a tool for exploring the essential thermodynamic properties of quantum systems. Generally quantum heat engines produce work using quantum material as a working substance [91–100]. The quantum nature of the working substance may cause the quantum heat engine to show properties untypical for classical engines. For example a close connection between the efficiency of the cycle and quantum correlations in the system is quantified in terms of entanglement. Like classical thermodynamics, the basic quantum thermodynamic processes are isothermal, adiabatic, isochoric, and isobaric processes. The corresponding thermodynamic variables which are kept constant during these classical processes are temperature, entropy, volume, and pressure respectively. They can be used to construct all the main heat cycles like Carnot, Otto, Stirling, Brayton, Diesel cycles. In the following subsections, The first law of thermodynamics in quantum-mechanical systems and a brief definition of the quantum thermodynamic processes are reviewed.

2.3.1. First law of thermodynamics and definition of work and heat in quantum systems

The Hamiltonian of a quantum system with finite number of energy levels E_n can be written as

$$H = \sum_n E_n |\Psi_n\rangle\langle\Psi_n|, \tag{2.25}$$

where $|\Psi_n\rangle$ is the nth eigenstate of the system. Therefore the internal energy U of the system is derived from the expectation value of the Hamiltonian

$$U = \langle H\rangle = \sum_n E_n P_n, \tag{2.26}$$

where P_n are the occupation probabilities. From Eq. (2.26) the first law of thermodynamics can be expressed as a function of eigenenergies E_n and occupation probabilities P_n as

$$dU = dQ + dW = \sum_n E_n dP_n + \sum_n P_n dE_n \tag{2.27}$$

So $dQ = \sum_n E_n dP_n$ and $dW = \sum_n P_n dE_n$ interpret the heat exchange and work performed by the quantum system respectively.

2.3.2. Quantum thermodynamic processes

Here we give a short description of the main three quantum processes, i.e. isothermal, isochoric and adiabatic:

Quantum isothermal process: In quantum isothermal process, the working substance is placed in contact with a heat bath at a constant temperature. The system can absorb heat from the bath and perform positive work to the outside. In order to maintain the temperature of the system, the occupation probability of the energy level need to change as the energy level varies. Consider the energy eigenvalues change from E_i to E_i' where i runs from 1 to N and N is the dimension of the Hilbert space of the working substance. Therefore the corresponding populations change from P_i to P_i' such that

$$\frac{P_n'}{P_m'} = e^{\beta(E_m' - E_n')} \tag{2.28}$$

where $\beta = \frac{1}{k_B T}$, k_B and T are the Boltzmann constant and the temperature respectively. It means that at every instant the system remains in thermodynamic equilibrium with the heat bath (quasi-static process).

Quantum isochoric process: Both in quantum and classical isochoric process, no work is done by the system and the energy as a form of heat is exchanged between the working substance and the heat bath. At the end of the process, the system equilibrates with the bath. During the process, the occupation probabilities P_i and thus the entropy S change as the system exchanges heat with the heat bath until reaching thermal equilibrium. The occupation probabilities at the end of the isochoric process satisfy Boltzmann distribution.

Quantum adiabatic process: The quantum adiabatic process proceeds slowly enough such that the quantum adiabatic theorem is satisfied [101–103]. Therefore the population of the eigenstates of the Hamiltonian remains unchanged, i.e. $dP_n = 0$ and there is no heat exchange $dQ = 0$, meaning that there is no energy exchanged between the system and the bath but according to Eq. (2.27) the work can be still done.

The differences between the classical and quantum thermodynamic processes are summarized in Table 2.1.

2.3.3. Quantum Otto heat engine

In this thesis, we just focus on the quantum Otto heat engine. Consider a multilevel quantum system with energies E_n in equilibrium with a hot bath at temperature T_H. The arrow (2) in Fig. 2.4 shows an adiabatic process in which the energy levels are changed adiabatically and hence the population in each energy level is unchanged. In the next step (3), the system is attached to a cold bath with temperature T_L. The occupation probabilities are changed and the system reaches equilibrium. For the second adiabatic process (step (4)), the energy levels change again adiabatically while the population are fixed. To complete the cycle, the system is again attached to the hot bath (arrow(1)). Therefore work is done on or by the system during the adiabatic processes and the heat exchange takes place during the thermalization steps.

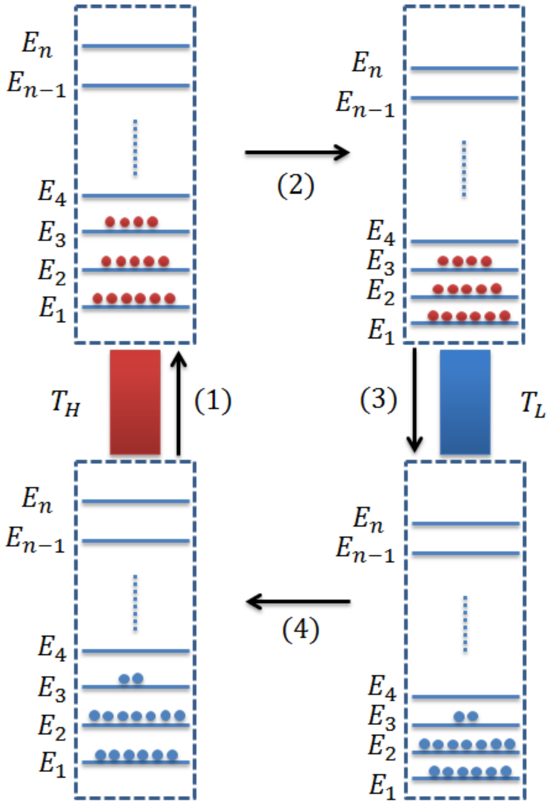

Figure 2.4. – A pictorial representation of the quantum Otto heat engine cycle with multilevel quantum system as the working substance.

Table 2.1. – Classical and quantum thermodynamic processes. Here U, V, T, P are indicated to the internal energy, volume, temperature and pressure of the working substance respectively. E_n, P_n are energy levels and occupation probabilities.

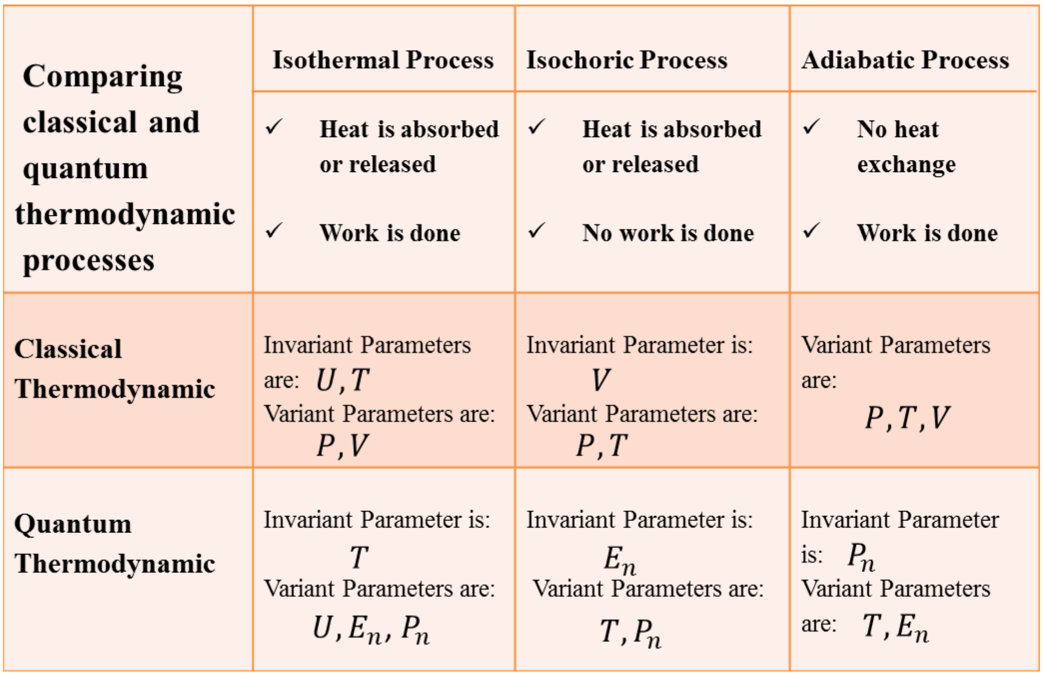

Comparing classical and quantum thermodynamic processes	**Isothermal Process**	**Isochoric Process**	**Adiabatic Process**
	✓ **Heat is absorbed or released** ✓ **Work is done**	✓ **Heat is absorbed or released** ✓ **No work is done**	✓ **No heat exchange** ✓ **Work is done**
Classical Thermodynamic	Invariant Parameters are: U, T Variant Parameters are: P, V	Invariant Parameter is: V Variant Parameters are: P, T	Variant Parameters are: P, T, V
Quantum Thermodynamic	Invariant Parameter is: T Variant Parameters are: U, E_n, P_n	Invariant Parameter is: E_n Variant Parameters are: T, P_n	Invariant Parameter is: P_n Variant Parameters are: T, E_n

3. Theoretical study of multiferroic system

3.1. The model Hamiltonian

We consider one-dimensional frustrated multiferroic spin-1/2 chain along the x axis with ferromagnetic nearest neighbor interactions $J_1 < 0$ and antiferromagnetic next nearest neighbor interactions $J_2 > 0$. The chain is subjected in external magnetic field B in z direction and external electric field $\wp$ in y direction.

$$\hat{H} = J_1 \sum_{i=1}^{N} \vec{S}_i \cdot \vec{S}_{i+1} + J_2 \sum_{i=1}^{N} \vec{S}_i \cdot \vec{S}_{i+2} - \wp \mathbf{P} - \gamma_e \hbar B \sum_{i=1}^{N} S_i^z. \tag{3.1}$$

S_i, γ_e and $\hbar$ are spin operator, gyromagnetic ratio and Planck's constant respectively. The coupling of the electric field to the induced polarization can be written as $-\wp\mathbf{P} = \wp g_{ME} \sum_i (\vec{S}_i \times \vec{S}_{i+1})^z$, where g_{ME} is the magnetoelectric coupling strength. The quantity $\kappa = \langle \kappa_i \rangle = \langle (\vec{S}_i \times \vec{S}_{i+1})^z \rangle$ is known as the z component of the vector chirality (VC), which we simply call chirality. In the following, the Zeeman energy and the interaction energy with the electric field are considered in units of the exchange constant, i.e. we assume that $-J_1 = J_2 = J$, $B \to \gamma_e \hbar B/J$, $\wp \to \wp g_{ME}/J$, and go over to dimensionless units.

3.2. Four spins: exact analytical solution

In the case of four spins, Hamiltonian Eq. (3.1) has the form

$$\begin{aligned} \hat{H} =& J_1(\vec{S}_1 \cdot \vec{S}_2 + \vec{S}_2 \cdot \vec{S}_3 + \vec{S}_3 \cdot \vec{S}_4 + \vec{S}_4 \cdot \vec{S}_1) \\ &+ J_2(\vec{S}_1 \cdot \vec{S}_3 + \vec{S}_2 \cdot \vec{S}_4 + \vec{S}_3 \cdot \vec{S}_1 + \vec{S}_4 \cdot \vec{S}_2) \\ &- \wp g_{ME}(S_1^y S_2^x + S_2^y S_3^x + S_3^y S_4^x + S_4^y S_1^x - S_1^x S_2^y - S_2^x S_3^y - S_3^x S_4^y - S_4^x S_1^y) \\ &- \gamma_e \hbar B (S_1^z + S_2^z + S_3^z - S_4^z). \end{aligned} \tag{3.2}$$

Because of the relation $[\sum_{i=1}^{N} S_i^z, \hat{H}] = 0$, one can write the Hamiltonian Eq. (3.2) in up ($|\uparrow\rangle$) and down ($|\downarrow\rangle$) basis

$$\begin{aligned}
&|\varphi_1\rangle = |\uparrow\uparrow\uparrow\uparrow\rangle,\ |\varphi_2\rangle = |\downarrow\uparrow\uparrow\uparrow\rangle,\ |\varphi_3\rangle = |\uparrow\downarrow\uparrow\uparrow\rangle,\ |\varphi_4\rangle = |\uparrow\uparrow\downarrow\uparrow\rangle,\\
&|\varphi_5\rangle = |\uparrow\uparrow\uparrow\downarrow\rangle,\ |\varphi_6\rangle = |\downarrow\downarrow\uparrow\uparrow\rangle,\ |\varphi_7\rangle = |\downarrow\uparrow\downarrow\uparrow\rangle,\ |\varphi_8\rangle = |\downarrow\uparrow\uparrow\downarrow\rangle,\\
&|\varphi_9\rangle = |\uparrow\downarrow\downarrow\uparrow\rangle,\ |\varphi_{10}\rangle = |\uparrow\downarrow\uparrow\downarrow\rangle,\ |\varphi_{11}\rangle = |\uparrow\uparrow\downarrow\downarrow\rangle,\ |\varphi_{12}\rangle = |\downarrow\downarrow\downarrow\uparrow\rangle,\\
&|\varphi_{13}\rangle = |\downarrow\downarrow\uparrow\downarrow\rangle,\ |\varphi_{14}\rangle = |\downarrow\uparrow\downarrow\downarrow\rangle,\ |\varphi_{15}\rangle = |\uparrow\downarrow\downarrow\downarrow\rangle, |\varphi_{16}\rangle = |\downarrow\downarrow\downarrow\downarrow\rangle.
\end{aligned} \tag{3.3}$$

In this basis the Hamiltonian Eq. (3.2) has a block diagonal form

$$H = \begin{pmatrix} E_g & 0 & 0 & \dots & 0 \\ 0 & D_1 & \ddots & \ddots & \vdots \\ 0 & \ddots & D_2 & \ddots & 0 \\ \vdots & \ddots & \ddots & D_3 & 0 \\ 0 & \dots & 0 & 0 & E_a \end{pmatrix}. \tag{3.4}$$

Here $E_g = J_1 + J_2 - 2B$, $E_a = J_1 + J_2 + 2B$ and the block matrices D_1, D_2, D_3 correspond to the one-, two- and three-excitations cases

$$D_1 = \begin{pmatrix} -B & J_1/2 - i\wp/2 & J_2 & J_1/2 + i\wp/2 \\ J_1/2 + i\wp/2 & -B & J_1/2 - i\wp/2 & J_2 \\ J_2 & J_1/2 + i\wp/2 & -B & J_1/2 - i\wp/2 \\ J_1/2 - i\wp/2 & J_2 & J_1/2 + i\wp/2 & -B \end{pmatrix},$$

$$D_2 = \begin{pmatrix} -J_2 & J_1/2 - i\wp/2 & J_2 & J_2 & J_1/2 + i\wp/2 & 0 \\ J_1/2 + i\wp/2 & -J_1 + J_2 & J_1/2 - i\wp/2 & J_1/2 - i\wp/2 & 0 & J_1/2 + i\wp/2 \\ J_2 & J_1/2 + i\wp/2 & -J_2 & 0 & J_1/2 - i\wp/2 & J_2 \\ J_2 & J_1/2 + i\wp/2 & 0 & -J_2 & J_1/2 - i\wp/2 & J_2 \\ J_1/2 - i\wp/2 & 0 & J_1/2 + i\wp/2 & J_1/2 + i\wp/2 & -J_1 + J_2 & J_1/2 - i\wp/2 \\ 0 & J_1/2 - i\wp/2 & J_2 & J_2 & J_1/2 + i\wp/2 & -J_2 \end{pmatrix},$$

$$D_3 = \begin{pmatrix} B & J_1/2 - i\wp/2 & J_2 & J_1/2 + i\wp/2 \\ J_1/2 + i\wp/2 & B & J_1/2 - i\wp/2 & J_2 \\ J_2 & J_1/2 + i\wp/2 & B & J_1/2 - i\wp/2 \\ J_1/2 - i\wp/2 & J_2 & J_1/2 + i\wp/2 & B \end{pmatrix}. \tag{3.5}$$

Notice that $B \to \gamma_e \hbar B$, $\wp \to \wp g_{ME}$ are used above. Eigenstates and eigenvalues of the Hamiltonian Eq. (3.2) in the case of one-excitation, read

$$\begin{aligned}
&|\psi_2\rangle = \frac{i}{2}|\downarrow\uparrow\uparrow\uparrow\rangle + \frac{-1}{2}|\uparrow\downarrow\uparrow\uparrow\rangle + \frac{-i}{2}|\uparrow\uparrow\downarrow\uparrow\rangle + \frac{1}{2}|\uparrow\uparrow\uparrow\downarrow\rangle,\\
&|\psi_3\rangle = \frac{-i}{2}|\downarrow\uparrow\uparrow\uparrow\rangle + \frac{-1}{2}|\uparrow\downarrow\uparrow\uparrow\rangle + \frac{i}{2}|\uparrow\uparrow\downarrow\uparrow\rangle + \frac{1}{2}|\uparrow\uparrow\uparrow\downarrow\rangle,\\
&|\psi_4\rangle = \frac{1}{2}|\downarrow\uparrow\uparrow\uparrow\rangle + \frac{-1}{2}|\uparrow\downarrow\uparrow\uparrow\rangle + \frac{1}{2}|\uparrow\uparrow\downarrow\uparrow\rangle + \frac{-1}{2}|\uparrow\uparrow\uparrow\downarrow\rangle,\\
&|\psi_5\rangle = \frac{1}{2}|\downarrow\uparrow\uparrow\uparrow\rangle + \frac{1}{2}|\uparrow\downarrow\uparrow\uparrow\rangle + \frac{1}{2}|\uparrow\uparrow\downarrow\uparrow\rangle + \frac{1}{2}|\uparrow\uparrow\uparrow\downarrow\rangle,\\
&E_2 = -J_2 - B - \wp, E_3 = -J_2 - B + \wp,\\
&E_4 = -J_1 + J_2 - B, E_5 = J_1 + J_2 - B.
\end{aligned} \tag{3.6}$$

In the case of two-excitations, we have

$$
\begin{aligned}
|\psi_6\rangle &= \alpha\big(|\downarrow\downarrow\uparrow\uparrow\rangle - i\mu|\downarrow\uparrow\downarrow\uparrow\rangle - |\downarrow\uparrow\uparrow\downarrow\rangle - |\uparrow\downarrow\downarrow\uparrow\rangle + i\mu|\uparrow\downarrow\uparrow\downarrow\rangle + |\uparrow\uparrow\downarrow\downarrow\rangle\big),\\
|\psi_7\rangle &= \gamma\big(|\downarrow\downarrow\uparrow\uparrow\rangle - i\lambda|\downarrow\uparrow\downarrow\uparrow\rangle - |\downarrow\uparrow\uparrow\downarrow\rangle - |\uparrow\downarrow\downarrow\uparrow\rangle + i\lambda|\uparrow\downarrow\uparrow\downarrow\rangle + |\uparrow\uparrow\downarrow\downarrow\rangle\big),\\
|\psi_8\rangle &= \frac{1}{\sqrt{6}}\big(|\downarrow\downarrow\uparrow\uparrow\rangle + |\downarrow\uparrow\downarrow\uparrow\rangle + |\downarrow\uparrow\uparrow\downarrow\rangle + |\uparrow\downarrow\downarrow\uparrow\rangle + |\uparrow\downarrow\uparrow\downarrow\rangle + |\uparrow\uparrow\downarrow\downarrow\rangle\big),\\
|\psi_9\rangle &= \frac{1}{\sqrt{12}}\big(|\downarrow\downarrow\uparrow\uparrow\rangle - 2|\downarrow\uparrow\downarrow\uparrow\rangle + |\downarrow\uparrow\uparrow\downarrow\rangle + |\uparrow\downarrow\downarrow\uparrow\rangle - 2|\uparrow\downarrow\uparrow\downarrow\rangle + |\uparrow\uparrow\downarrow\downarrow\rangle\big),\\
|\psi_{10}\rangle &= \frac{-1}{\sqrt{2}}|\downarrow\downarrow\uparrow\uparrow\rangle + \frac{1}{\sqrt{2}}|\uparrow\uparrow\downarrow\downarrow\rangle,\\
|\psi_{11}\rangle &= \frac{-1}{\sqrt{2}}|\downarrow\uparrow\uparrow\downarrow\rangle + \frac{1}{\sqrt{2}}|\uparrow\downarrow\downarrow\uparrow\rangle,\\
E_6 &= -\frac{J_1}{2} - J_2 + \frac{1}{2}\sqrt{J_1^2 + 16J_2^2 - 8J_1J_2 + 8\wp^2},\\
E_7 &= -\frac{J_1}{2} - J_2 - \frac{1}{2}\sqrt{J_1^2 + 16J_2^2 - 8J_1J_2 + 8\wp^2},\\
E_8 &= J_1 + J_2, E_9 = -2J_1 + J_2, E_{10} = -J_2, E_{11} = -J_2.
\end{aligned}
\tag{3.7}
$$

Where we introduced the following notations

$$
\begin{aligned}
\alpha &= \frac{1}{\sqrt{4+2\mu^2}}, \mu = \frac{-2J_2 + \frac{J_1}{2} - \frac{1}{2}\sqrt{{J_1}^2 + 16{J_2}^2 - 8J_1J_2 + 8\wp^2}}{\wp},\\
\gamma &= \frac{1}{\sqrt{4+2\lambda^2}}, \lambda = \frac{-2J_2 + \frac{J_1}{2} + \frac{1}{2}\sqrt{{J_1}^2 + 16{J_2}^2 - 8J_1J_2 + 8\wp^2}}{\wp}.
\end{aligned}
\tag{3.8}
$$

And in the case of three-excitations, we have

$$
\begin{aligned}
|\psi_{12}\rangle &= \frac{i}{2}|\downarrow\downarrow\downarrow\uparrow\rangle + \frac{-1}{2}|\downarrow\downarrow\uparrow\downarrow\rangle + \frac{-i}{2}|\downarrow\uparrow\downarrow\downarrow\rangle + \frac{1}{2}|\uparrow\downarrow\downarrow\downarrow\rangle,\\
|\psi_{13}\rangle &= \frac{-i}{2}|\downarrow\downarrow\downarrow\uparrow\rangle + \frac{-1}{2}|\downarrow\downarrow\uparrow\downarrow\rangle + \frac{i}{2}|\downarrow\uparrow\downarrow\downarrow\rangle + \frac{1}{2}|\uparrow\downarrow\downarrow\downarrow\rangle,\\
|\psi_{14}\rangle &= \frac{1}{2}|\downarrow\downarrow\downarrow\uparrow\rangle + \frac{1}{2}|\downarrow\downarrow\uparrow\downarrow\rangle + \frac{1}{2}|\downarrow\uparrow\downarrow\downarrow\rangle + \frac{1}{2}|\uparrow\downarrow\downarrow\downarrow\rangle,\\
|\psi_{15}\rangle &= \frac{1}{2}|\downarrow\downarrow\downarrow\uparrow\rangle + \frac{-1}{2}|\downarrow\downarrow\uparrow\downarrow\rangle + \frac{1}{2}|\downarrow\uparrow\downarrow\downarrow\rangle + \frac{-1}{2}|\uparrow\downarrow\downarrow\downarrow\rangle,\\
E_{12} &= -J_2 + B + \wp, E_{13} = -J_2 + B - \wp,\\
E_{14} &= J_1 + J_2 + B, E_{15} = -J_1 + J_2 + B.
\end{aligned}
\tag{3.9}
$$

3.2.1. Observing different phases in the system

In a strong magnetic field $B \gg |J_1|, J_2, \wp$ the ground state of the system is the fully polarized state $|F\rangle = |\uparrow\uparrow\uparrow\uparrow\rangle$ with the corresponding energy $E_F = J_1 + J_2 - 2B$. The chirality and pair entanglement between any two arbitrary spins are equal to zero. By decreasing the magnetic field as

$$B_0 < B < \wp + J_1 + 2J_2, \quad B_0 = \frac{\sqrt{(J_1 - 4J_2)^2 + 8\wp^2} + J_1 - 2\wp}{2}, \tag{3.10}$$

the ground state becomes the state

$$|\psi_2\rangle = \frac{i}{2}|\downarrow\uparrow\uparrow\uparrow\rangle + \frac{-1}{2}|\uparrow\downarrow\uparrow\uparrow\rangle + \frac{-i}{2}|\uparrow\uparrow\downarrow\uparrow\rangle + \frac{1}{2}|\uparrow\uparrow\uparrow\downarrow\rangle, \tag{3.11}$$

with the corresponding energy $E_2 = -J_2 - B - \wp$. The chirality jumps to $\langle\psi_2|\kappa|\psi_2\rangle = \frac{1}{4}$, and a finite entanglement is generated. The ratio between two- and one-tangle which quantifies amount of the entanglement stored in the pair correlations τ_2 compare to the total multi spin entanglement τ_1 is $\tau = \frac{\tau_2}{\tau_1} = 1$. In calculating this ratio we used the definitions in Eq. (2.19) and Eq. (2.22) in the previous chapter. This result means that half of the entanglement generated by increasing external electric field or decreasing the magnetic field is stored in the collective multi spin entanglement and only half is stored in the pair correlations. Further decreasing the magnetic field below B_0, the ground state becomes

$$|\psi_7\rangle = \gamma\big(|\downarrow\downarrow\uparrow\uparrow\rangle - i\lambda|\downarrow\uparrow\downarrow\uparrow\rangle - |\downarrow\uparrow\uparrow\downarrow\rangle - |\uparrow\downarrow\downarrow\uparrow\rangle + i\lambda|\uparrow\downarrow\uparrow\downarrow\rangle + |\uparrow\uparrow\downarrow\downarrow\rangle\big). \tag{3.12}$$

In this case, for total chirality we have $\kappa = \langle\psi_7|\kappa_i|\psi_7\rangle = 2\lambda\gamma^2$. Its electric field dependence is plotted in Fig. 3.1.
The ratio between one-tangle τ_1 and two-tangle τ_2, for $0 < \wp \leq \frac{8J_2 - 2J_1}{7}$ reads

$$\tau = \frac{\tau_2}{\tau_1} = (\frac{2 - \lambda^2}{2 + \lambda^2})^2 < 1. \tag{3.13}$$

Therefore, in this case the entanglement generated by the electric field is basically stored in many spin correlations rather than in two spin correlations.

3.2.2. Fidelity susceptibilities

In order to examine the sensitivity of the multiferroic spin chain with respect to the tiny change of the driving fields we evaluate the fidelity susceptibility [73–76]. The stability of the multiferroic spin chain with respect to a tiny change of the magnetic field δB is quantified by the following equation

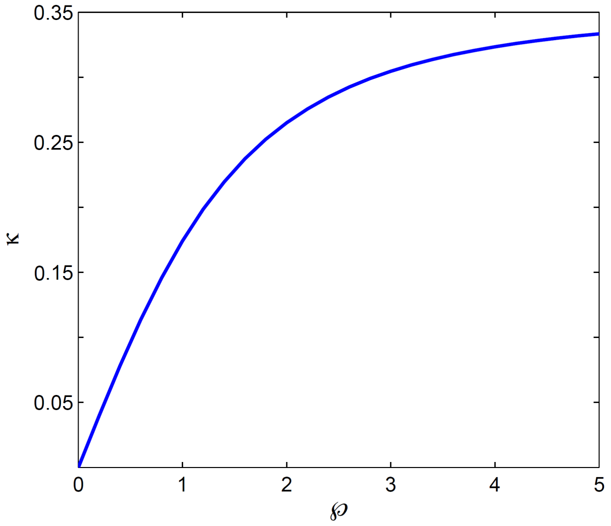

Figure 3.1. – Electric field dependence of chirality κ for the following values of the parameters: $-J_1 = J_2 = 1, B = 0.25$.

$$\begin{aligned} F_F^B &= \sqrt{1-\chi_F^B}, \\ \chi_F^B &= \sum_{n\neq g} \frac{|\langle\psi_n(\wp,B)|H_I^B|\psi_g(\wp,B)\rangle|^2}{[E_n(\wp,B)-E_g(\wp,B)]^2}. \end{aligned} \tag{3.14}$$

Here $|\psi_n(\wp,B)\rangle$, E_n are eigenfunctions and eigenvalues of the Hamiltonian (3.2), $|\psi_g(\wp,B)\rangle$, E_g correspond to the ground state and ground energy of the system and $H_I^B = -\delta B\sum_{i=1}^{N} S_i^z$ describes small perturbations of the system corresponding to a slight change of the magnetic field δB. Sensitivity to a slight change of the electric field is also quantified by

$$\begin{aligned} F_F^\wp &= \sqrt{1-\chi_F^\wp}, \\ \chi_F^\wp &= \sum_{n\neq g} \frac{|\langle\psi_n(\wp,B)|H_I^\wp|\psi_g(\wp,B)\rangle|^2}{[E_n(\wp,B)-E_g(\wp,B)]^2}. \end{aligned} \tag{3.15}$$

Where $H_I^\wp = -\delta\wp\sum_{i=1}^{N}[\hat{e}_x \times (\vec{S}_i \times \vec{S}_{i+1})]$ is the perturbation corresponding to a slight change of the electric field $\delta\vec{\wp}$. In the case of a four spins system we observe that the system is not sensitive to the $\delta\vec{B}$. Magnetic fidelity susceptibility is zero $\chi_F^B = 0$ for all ground states corresponding to different values of the driving fields B, $\wp$ and therefore $F_F^B = 1$. However, the electric field fidelity susceptibility $\chi_F^\wp$ is finite if the ground state of the system is the state $|\psi_7\rangle$

$$\chi_F^{\wp} = \frac{(-J_2 + \frac{J_1}{4})^2}{(-J_2 + \frac{J_1}{4})^2 + \frac{\wp^2}{2}} (\frac{4\alpha\gamma}{\wp})^2. \tag{3.16}$$

Its electric field dependence is depicted in Fig. 3.2.

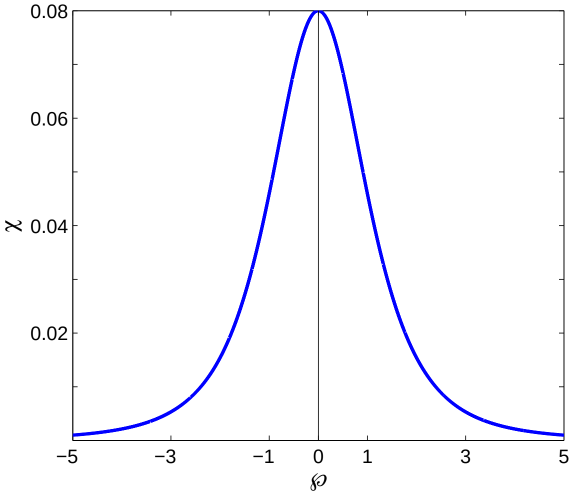

Figure 3.2. – Electric field fidelity susceptibility for the following values of the parameters: $-J_1 = J_2 = 1, B = 0.25$. Even a weak electric field leads to a substantial reduction of the fidelity susceptibility.

This result shows that in the case of an even number of excitations corresponding to the state $|\psi_7\rangle$ the system becomes sensitive to a small perturbation of the electric field amplitude.

3.2.3. Evaluating quantum state transfer fidelity

Let us evaluate the quantum state transfer fidelity in the case of one-excitation in the system utilizing the proposal developed by S. Bose [63] which was explained in details in section 2.2.1. The time dependence of the quantum state transfer fidelity between the initial state $|1\rangle = |\downarrow\uparrow\uparrow\uparrow\rangle$ and final states $|2\rangle = |\uparrow\downarrow\uparrow\uparrow\rangle$ and $|3\rangle = |\uparrow\uparrow\downarrow\uparrow\rangle$ are presented in Fig. 3.3.

The corresponding transition amplitudes read

$$f_{1,2}(\wp, B, t) = \tfrac{1}{4}(\exp[-iE_5t] - \exp[-iE_4t]) - \tfrac{i}{4}(\exp[-iE_2t] - \exp[-iE_3t]),$$
$$f_{2,1}(\wp, B, t) = -\tfrac{1}{4}(\exp[-iE_4t] - \exp[-iE_5t]) - \tfrac{i}{4}(\exp[-iE_2t] - \exp[-iE_3t]),$$

$$f_{1,3}(\wp, B, t) = f_{3,1}(\wp, B, t) = \\ -\frac{1}{4}(\exp[-iE_2t] + \exp[-iE_3t] - \exp[-iE_4t] - \exp[-iE_5t]). \tag{3.17}$$

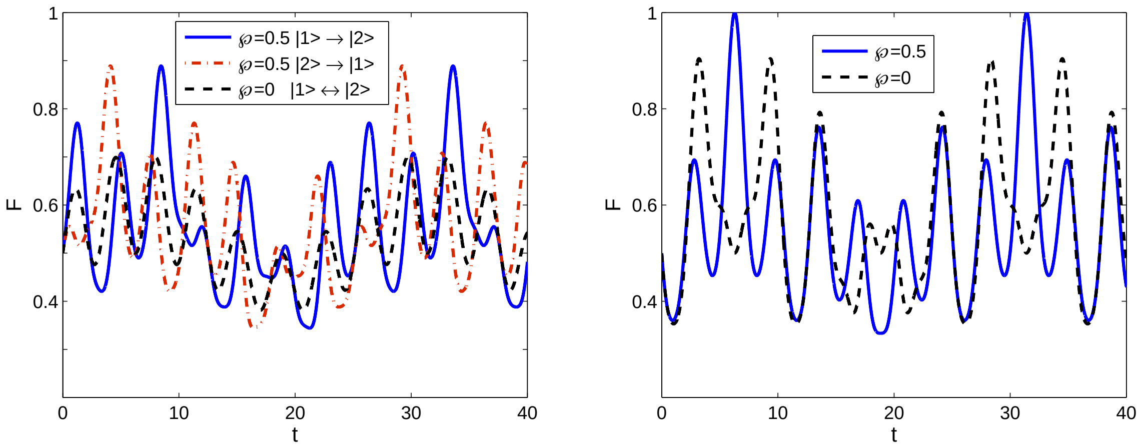

Figure 3.3. – Time and electric field dependence of the quantum state transfer fidelity for values of $J_1 = -J_2 = 1, B = 0.25$. Left panel: Fidelity for $|1\rangle \longrightarrow |2\rangle$ and $|2\rangle \longrightarrow |1\rangle$. Right panel: Fidelity for $|1\rangle \longrightarrow |3\rangle = |3\rangle \longrightarrow |1\rangle$.

From Fig. 3.3 one can see that the electric field increases the quantum state transfer fidelity, particularly from $|1\rangle$ to $|3\rangle$. The oscillating behavior of fidelity is related to the interference effect between different quantum states $E_n(\wp)$. The transition $|1\rangle \longleftrightarrow |3\rangle$ shows no directional dependence for the fidelity because of the boundary condition $S_{N+1} = S_1$.

3.3. Large systems: numerical approach

In this section we present some numerical results using exact diagonalization technique for different multiferroic chain N=8,10,... spins.

We show the mean magnetization versus magnetic field for various electric fields. In all cases for a given magnetic field, we search for the lowest energy for all the excited states. Wherever the mean magnetization jumps with two steps, a transition to nematic phase happens. However if the mean magnetization jumps with unit steps, a chiral feature can be predicted. See Fig. 3.4.

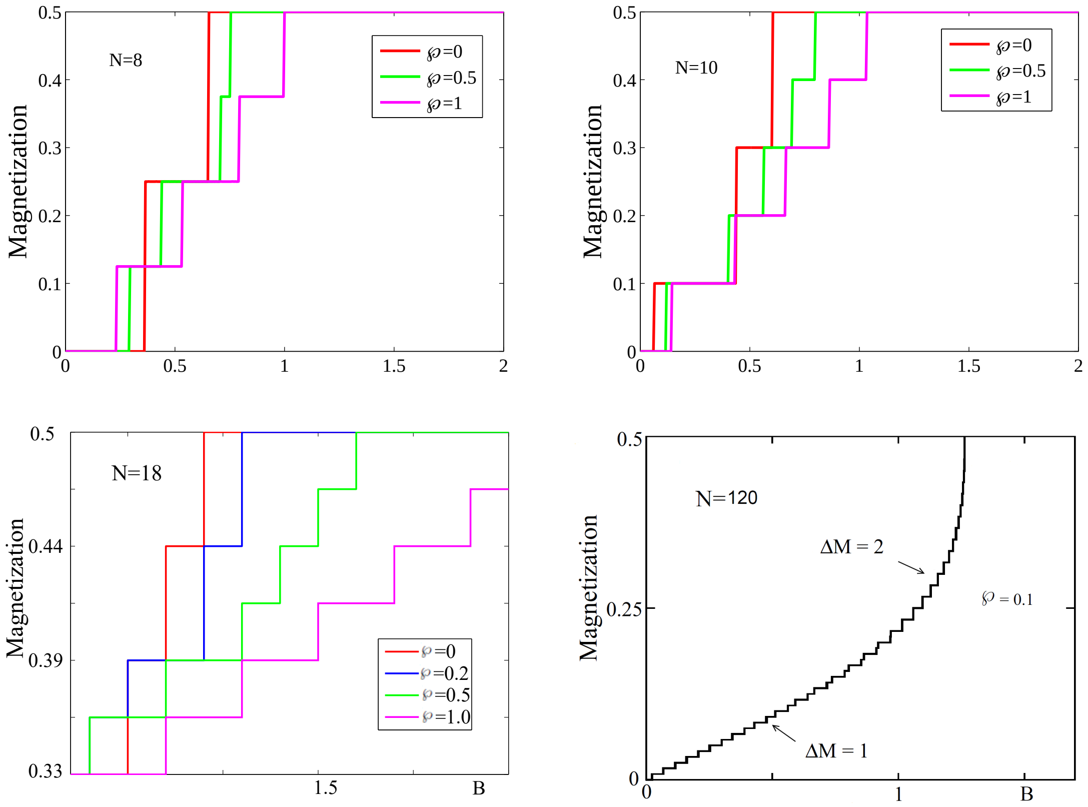

Figure 3.4. – Mean values of magnetization for different size of the system. The plot for $N = 120$ is adapted from [7].

Comparing quantum phase transitions caused by the modulation of the amplitude of electric and magnetic fields respectively, we see that in the case of electric field, even a tiny change of the amplitude leads to a phase transition. This result is consistent with the results obtained in the previous section, where we showed the sensitivity of fidelity susceptibility concerning to the slight modulation of the electric field amplitude.

3.4. Summary

It was shown that ground state phases of one dimensional frustrated ferromagnetic spin-1/2 chain are extremely sensitive to the driving electric field. Tiny values of the electric field are sufficient to change nematic phases of helical multiferroics in favor of the chiral phase. This steering of the spin order with electric field is due to the magnetoelectric coupling in such systems. We analyzed the fidelity susceptibility and quantum state transfer fidelity and showed that the system is more sensitive to the small changes of the electric field. It enables us to transmit quantum state through the multiferroic spin chain with higher fidelity by proper tuning of the external electric driving field. These findings can be potentially important for the practical application of multiferoics in quantum information processing.

4. Coherent control of the system by electric field pulses

Control of the spin dynamics in multiferroic material ($\mathrm{TbMnO_3}$) via intense THz light pulses was realized recently in the experimental work by Kubacka et al. [104]. They showed that the manipulation of the magnetic structure with the electric field of THz pulse is possible on a sub-picoseconds time scale. In this chapter we study both analytically and numerically the influence of short electric field pulses switching the system into an incommensurate chiral phase. It is instructive to study the entanglement and chirality behavior when the ground state of the system undergoes time evaluation after applying the pulse. For this purpose we consider that the electric field in Eq. (3.1) consists of two static $\wp_0$ and dynamic $\wp_1(t)$ parts respectively, i.e. $\wp = \wp_0 + \wp_1(t)$. So the Hamiltonian Eq. (3.1) becomes

$$\begin{aligned}
&\hat{H} = \hat{H}_0 + \hat{H}_1, \\
&\hat{H}_0 = J_1 \sum_{i=1}^{N} \vec{S}_i \cdot \vec{S}_{i+1} + J_2 \sum_{i=1}^{N} \vec{S}_i \cdot \vec{S}_{i+2} - \gamma_e \hbar B \sum_{i=1}^{N} S_i^z + \wp_0 g_{ME} \sum_{i=1}^{N} (\vec{S}_i \times \vec{S}_{i+1})^z, \\
&\hat{H}_1 = \wp_1(t) g_{ME} \sum_{i=1}^{N} (\vec{S}_i \times \vec{S}_{i+1})^z.
\end{aligned} \tag{4.1}$$

Where $\hat{H}_0$ is unperturbed Hamiltonian with the static electric field $\wp_0$ and $\hat{H}_1$ is the perturbation Hamiltonian with time dependent electric field $\wp_1(t)$. To proceed further, we assume that the pulse is applied at $t = 0$ and has the following shape

$$\wp_1(t) = \begin{cases} \frac{\wp_1^0}{\epsilon} & \text{if} - \frac{\epsilon}{2} < t < \frac{\epsilon}{2} \\ 0 & \text{otherwise} \end{cases}. \tag{4.2}$$

For very small ϵ, the pulse is expressible as a δ-kick with the strength $\wp_1^0$. The time evolution of the system is given by the Schrödinger equation

$$i\frac{\partial}{\partial t}|\psi(t)\rangle = \hat{H}|\psi(t)\rangle, \tag{4.3}$$

with the initial condition $|\psi(t = -\frac{\epsilon}{2})\rangle = |\psi_0\rangle$. Where $|\psi_0\rangle$ is the ground state of the system before applying the pulse. For $t > \frac{\epsilon}{2}$ we have a pulse free propagation with Hamiltonian $\hat{H}_0$. One can rescale the time as $T = (t + \frac{\epsilon}{2})/\epsilon$. Hence right before the pulse ($t = -\frac{\epsilon}{2}$), $T = 0$ and right after the pulse ($t = \frac{\epsilon}{2}$), $T = 1$. Therefore, the Schrödinger equation in the new variables describes the evolution as

$$i\frac{\partial}{\partial T}|\psi(T)\rangle = \hat{O}|\psi(T)\rangle, \quad \hat{O} = \underbrace{\wp_1^0 g_{ME}}_{d_1} \sum_{i=1}^{N} (\vec{S}_i \times \vec{S}_{i+1})^z. \tag{4.4}$$

The solution to Eq. (4.4) is written in a closed form

$$|\psi(T)\rangle = e^{-iT\hat{O}}|\psi(T=0)\rangle. \tag{4.5}$$

This means that right after the pulse $|\psi(t = \frac{\epsilon}{2})\rangle = e^{-i\hat{O}}|\psi(T = 0)$ and at any arbitrary time $t = t'$ after the pulse we have

$$|\psi(t = t')\rangle = \sum_n e^{-i\mathcal{E}_n t'}|\phi_n\rangle \underbrace{\langle\phi_n|e^{-i\hat{O}}|\psi(0)\rangle}_{G_n}. \tag{4.6}$$

Where $|\phi_n\rangle$ and $\mathcal{E}_n$ are n-th eigenstate and eigenvalue of the Hamiltonian $\hat{H}_0$ in Eq. (4.1).

4.1. Four spins case

Here we analyze the prototype model of four spins. In this case we know exactly all eigenstates $|\phi_n\rangle$ and eigenvalues $\mathcal{E}_n$ in Eq. (4.6). As we discussed in chapter 3, one can engineer the external electric and magnetic fields and get the one spin flipped ground state $|\phi_2\rangle = \frac{i}{2}|\downarrow\uparrow\uparrow\uparrow\rangle + \frac{-1}{2}|\uparrow\downarrow\uparrow\uparrow\rangle + \frac{-i}{2}|\uparrow\uparrow\downarrow\uparrow\rangle + \frac{1}{2}|\uparrow\uparrow\uparrow\downarrow\rangle$. Therefore with choosing the initial state of the system $|\psi(0)\rangle = |\phi_2\rangle$, we need to find the state of the system at any time $t = t'$ after pulse using Eq. (4.6)

$$|\psi(t = t')\rangle = \sum_n e^{-i\mathcal{E}_n t'}|\phi_n\rangle\langle\phi_n|e^{-i\hat{O}}|\phi_2\rangle. \tag{4.7}$$

Among the 16 coefficients of G_n , only G_2 is non-zero

$$G_2 = \langle\phi_2|e^{-i\hat{O}}|\phi_2\rangle = 1 + 2iy_1 - 2y_2 - 2iy_3 + 2y_4. \tag{4.8}$$

Where

$$y_1 = \tfrac{1}{4}(-\sin[d_1] - \sinh[d_1]), \quad y_2 = \tfrac{1}{4}(-\cos[d_1] - \cosh[d_1]), \tag{4.9}$$

$$y_3 = \tfrac{1}{4}(\sin[d_1] - \sinh[d_1]), \quad y_4 = \tfrac{1}{4}(-2 + \cos[d_1] - \cosh[d_1]). \tag{4.10}$$

After the simplification of Eq. (4.8) we get $G_2 = -i\sin[d_1] + \cos[d_1]$. Using the state Eq. (4.7) the chirality can be calculated as $\langle\psi(t')|\kappa_i|\psi(t')\rangle = 1/4$. This time in-dependency behavior can be understood by observing the structure of the vector chirality operator $\kappa_i = (S_i^- S_{i+1}^+ - S_i^+ S_{i+1}^-)/2i$, where raising and lowering operators S_i^+ and S_i^- are defined by $S_i^+|\uparrow\rangle = 0$, $S_i^+|\downarrow\rangle = |\uparrow\rangle$, $S_i^-|\downarrow\rangle = 0$ and $S_i^-|\uparrow\rangle = |\downarrow\rangle$. For one-excitation initial state $|\phi_2\rangle$, the expectation values of correlation terms $S_i^- S_{i+1}^+$ and $S_i^+ S_{i+1}^-$ are respectively $i/4$ and $-i/4$ which finally adds up to 1/4.

The two spins flipped initial state $|\phi_7\rangle = \gamma\big(|\downarrow\downarrow\uparrow\uparrow\rangle - i\lambda|\downarrow\uparrow\downarrow\uparrow\rangle - |\downarrow\uparrow\uparrow\downarrow\rangle - |\uparrow\downarrow\downarrow\uparrow\rangle + i\lambda|\uparrow\downarrow\uparrow\downarrow\rangle + |\uparrow\uparrow\downarrow\downarrow\rangle\big)$ can be derived by manipulating with the electric and magnetic fields. In this case the state of the system at any time $t = t'$ after the pulse using Eq. (4.6) reads

$$|\psi(t=t')\rangle = e^{-i\mathcal{E}_6 t'}|\phi_6\rangle \underbrace{\langle\phi_6|e^{-i\hat{O}}|\phi_7\rangle}_{G_6} + e^{-i\mathcal{E}_7 t'}|\phi_7\rangle \underbrace{\langle\phi_7|e^{-i\hat{O}}|\phi_7\rangle}_{G_7}. \tag{4.11}$$

We calculate the matrix elements G_6 and G_7 below

$$\begin{aligned} G_6 = \langle\phi_6|e^{-i\hat{O}}|\phi_7\rangle &= 4\alpha\gamma[1 - 4X_1 - 2i\lambda X_2 + 4X_3 + 2i\lambda X_4] + \\ &\quad 2i\alpha\mu\gamma[-i\lambda + 4i\lambda X_1 - 4X_2 - 4i\lambda X_3 + 4X_4], \end{aligned}$$

$$\begin{aligned} G_7 = \langle\phi_7|e^{-i\hat{O}}|\phi_7\rangle &= 4\gamma^2[1 - 4X_1 - 2i\lambda X_2 + 4X_3 + 2i\lambda X_4] + \\ &\quad 2i\gamma^2\lambda[-i\lambda + 4i\lambda X_1 - 4X_2 - 4i\lambda X_3 + 4X_4]. \end{aligned} \tag{4.12}$$

Where

$$\begin{aligned} X_1 &= \frac{1}{8}\big(-\cos[\sqrt{2}d_1] + \cosh[\sqrt{2}d_1]\big), \\ X_2 &= \frac{1}{8}\big(-\sqrt{2}\sin[\sqrt{2}d_1] + \sinh[\sqrt{2}d_1]\big), \\ X_3 &= \frac{1}{8}\big(\cos[\sqrt{2}d_1] + \cosh[\sqrt{2}d_1]\big), \\ X_4 &= \frac{1}{8}\big(\sqrt{2}\sin[\sqrt{2}d_1] + \sinh[\sqrt{2}d_1]\big). \end{aligned} \tag{4.13}$$

Substituting Eq. (4.13) in Eq. (4.12) we obtain

$$\begin{aligned} G_6 &= \frac{4i\alpha\gamma(\lambda+\mu)}{\sqrt{2}}\sin[\sqrt{2}d_1], \\ G_7 &= \cos[\sqrt{2}d_1] + \frac{8i\gamma^2\lambda}{\sqrt{2}}\sin[\sqrt{2}d_1]. \end{aligned} \tag{4.14}$$

The expectation value of chirality at any time $t = t'$ after the pulse is given by

$$\begin{aligned} \langle\kappa_i\rangle &= 2\alpha^2\mu|G_6|^2 + 2\gamma^2\lambda|G_7|^2 + \\ \alpha\gamma(\mu+\lambda)&\Bigg(2\Re(G_7^* G_6)\cos[(\mathcal{E}_7 - \mathcal{E}_6)t'] + 2\Im(G_7^* G_6)\sin[(\mathcal{E}_7 - \mathcal{E}_6)t']\Bigg). \end{aligned} \tag{4.15}$$

Here $\Re$ and $\Im$ are ‘Real’ and ‘Imaginary’ part of $G_7^* G_6$, respectively. The time dependence of chirality Eq. (4.15) is plotted in Fig. 4.1. We see that the chirality oscillates with time.

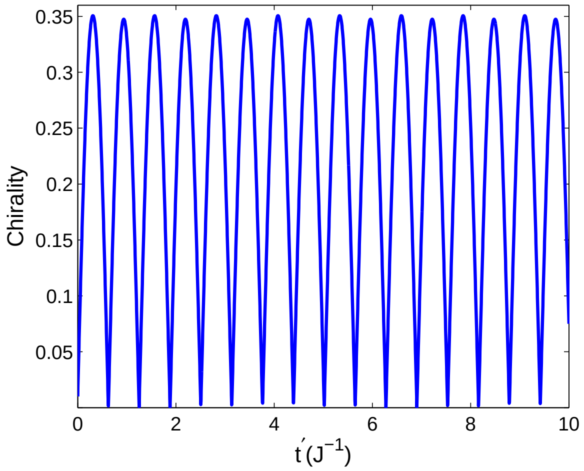

Figure 4.1. – Chirality Eq. (4.15) for the following values of the parameters: $-J_1 = J_2 = 1, B = 0.25, d_0 = \wp_0 g_{ME} = 0.05, d_1 = d_0/0.1$.

The extremum of the chirality Eq. (4.15) are located at the time given by

$$t'_{ext} = \frac{1}{(\mathcal{E}_7 - \mathcal{E}_6)} \left[\arctan[\frac{\Im(G_7^* G_6)}{\Re(G_7^* G_6}] + k\pi \right]. \tag{4.16}$$

Where k is an integer. The chirality time period of oscillations is $\pi/(\mathcal{E}_7 - \mathcal{E}_6)$.

4.1.1. Quantifying the entanglement measures

In this subsection we study the entanglement and analyze the time evolution of it after applying the short electric field pulse. For the ground states $|\phi_2\rangle$ or $|\phi_7\rangle$, which were used earlier to calculate chirality, the one-tangle $\tau_1 = 4\det\rho_1$ is unity and is independent of time. This can be explained by looking at the structure of single qubit reduced density matrix. The off-diagonal elements $\langle S_k^+\rangle$ and $\langle S_k^-\rangle$ will be zero for $|\phi_2\rangle$ and $|\phi_7\rangle$ states and therefore the determinant of the reduced density matrix ρ_1 i.e. $\frac{1}{4} - \langle S_1^z\rangle^2$ is constant.

In the case of one-excitation ground state $|\phi_2\rangle$ the two-tangle $\tau_2 = C_{12}^2 + C_{13}^2 + C_{14}^2$ is invariable, however for two-excitations ground state $|\phi_7\rangle$ it varies with time. Calculation of the concurrences C_{12}, C_{13}, C_{14}, can be done by obtaining the reduced density matrices $\rho_{12}, \rho_{13}, \rho_{14}$ after tracing out of the rest spins from the total density matrix $\hat{\rho} = |\psi(t)\rangle\langle\psi(t)|$, which is constructed using Eq. (4.11). These three reduced density matrices $\rho_{12}, \rho_{13}, \rho_{14}$ are presented below

$$
\begin{aligned}
\rho_{12} = {} & \big(|G_6|^2\alpha^2 + G_7G_6^*\alpha\gamma e^{-i(\mathcal{E}_7-\mathcal{E}_6)t'} + G_6G_7^*\alpha\gamma e^{-i(\mathcal{E}_6-\mathcal{E}_7)t'} + |G_7|^2\gamma^2\big)|\uparrow\uparrow\rangle\langle\uparrow\uparrow| \\
& +\big(|G_6|^2\alpha^2(1+\mu^2) - G_7G_6^*\alpha\gamma e^{-i(\mathcal{E}_7-\mathcal{E}_6)t'} - G_6G_7^*\alpha\gamma e^{-i(\mathcal{E}_6-\mathcal{E}_7)t'} + \\
& |G_7|^2\gamma^2(1+\lambda^2)\big)|\uparrow\downarrow\rangle\langle\uparrow\downarrow| + \big(2i|G_6|^2\alpha^2\mu + iG_7G_6^*\alpha\gamma(\lambda+\mu)e^{-i(\mathcal{E}_7-\mathcal{E}_6)t'} + \\
& iG_6G_7^*\alpha\gamma(\lambda+\mu)e^{-i(\mathcal{E}_6-\mathcal{E}_7)t'} + 2i|G_7|^2\gamma^2\lambda\big)|\downarrow\uparrow\rangle\langle\uparrow\downarrow| + \big(-2i|G_6|^2\alpha^2\mu - \\
& iG_7G_6^*\alpha\gamma(\lambda+\mu)e^{-i(\mathcal{E}_7-\mathcal{E}_6)t'} - iG_6G_7^*\alpha\gamma(\lambda+\mu)e^{-i(\mathcal{E}_6-\mathcal{E}_7)t'} - \\
& 2i|G_7|^2\gamma^2\lambda\big)|\uparrow\downarrow\rangle\langle\downarrow\uparrow| + \big(|G_6|^2\alpha^2(1+\mu^2) - G_7G_6^*\alpha\gamma e^{-i(\mathcal{E}_7-\mathcal{E}_6)t'} - \\
& G_6G_7^*\alpha\gamma e^{-i(\mathcal{E}_6-\mathcal{E}_7)t'} + |G_7|^2\gamma^2(1+\lambda^2)\big)|\downarrow\uparrow\rangle\langle\downarrow\uparrow| + \big(|G_6|^2\alpha^2 + \\
& G_7G_6^*\alpha\gamma e^{-i(\mathcal{E}_7-\mathcal{E}_6)t'} + G_6G_7^*\alpha\gamma e^{-i(\mathcal{E}_6-\mathcal{E}_7)t'} + |G_7|^2\gamma^2\big)|\downarrow\downarrow\rangle\langle\downarrow\downarrow|,
\end{aligned}
\tag{4.17}
$$

$$
\begin{aligned}
\rho_{13} = {} & \big(|G_6|^2\alpha^2\mu^2 + G_7G_6^*\alpha\gamma\lambda\mu e^{-i(\mathcal{E}_7-\mathcal{E}_6)t'} + G_6G_7^*\alpha\gamma\lambda\mu e^{-i(\mathcal{E}_6-\mathcal{E}_7)t'} + \\
& |G_7|^2\gamma^2\big)|\uparrow\uparrow\rangle\langle\uparrow\uparrow| + \big(2|G_6|^2\alpha^2 + 2G_7G_6^*\alpha\gamma e^{-i(\mathcal{E}_7-\mathcal{E}_6)t'} + \\
& 2G_6G_7^*\alpha\gamma e^{-i(\mathcal{E}_6-\mathcal{E}_7)t'} + 2|G_7|^2\gamma^2\big)|\uparrow\downarrow\rangle\langle\uparrow\downarrow| + \big(-2|G_6|^2\alpha^2 - \\
& 2G_7G_6^*\alpha\gamma e^{-i(\mathcal{E}_7-\mathcal{E}_6)t'} - 2G_6G_7^*\alpha\gamma e^{-i(\mathcal{E}_6-\mathcal{E}_7)t'} - 2|G_7|^2\gamma^2\lambda\big)|\downarrow\uparrow\rangle\langle\uparrow\downarrow| + \\
& \big(-2|G_6|^2\alpha^2 - 2G_7G_6^*\alpha\gamma e^{-i(\mathcal{E}_7-\mathcal{E}_6)t'} - 2G_6G_7^*\alpha\gamma e^{-i(\mathcal{E}_6-\mathcal{E}_7)t'} + \\
& 2|G_7|^2\gamma^2\lambda\big)|\uparrow\downarrow\rangle\langle\downarrow\uparrow| + \big(2|G_6|^2\alpha^2 + 2G_7G_6^*\alpha\gamma e^{-i(\mathcal{E}_7-\mathcal{E}_6)t'} + \\
& 2G_6G_7^*\alpha\gamma e^{-i(\mathcal{E}_6-\mathcal{E}_7)t'} + 2|G_7|^2\gamma^2\big)|\downarrow\uparrow\rangle\langle\downarrow\uparrow| + \big(|G_6|^2\alpha^2\mu^2 + \\
& G_7G_6^*\alpha\gamma\lambda\mu e^{-i(\mathcal{E}_7-\mathcal{E}_6)t'} + G_6G_7^*\alpha\gamma\lambda\mu e^{-i(\mathcal{E}_6-\mathcal{E}_7)t'} + \\
& |G_7|^2\gamma^2\lambda^2\big)|\downarrow\downarrow\rangle\langle\downarrow\downarrow|,
\end{aligned}
\tag{4.18}
$$

$$
\begin{aligned}
\rho_{14} = {} & \big(|G_6|^2\alpha^2 + G_7G_6^*\alpha\gamma e^{-i(\mathcal{E}_7-\mathcal{E}_6)t'} + G_6G_7^*\alpha\gamma e^{-i(\mathcal{E}_6-\mathcal{E}_7)t'} + |G_7|^2\gamma^2\big)|\uparrow\uparrow\rangle\langle\uparrow\uparrow| \\
& +\big(|G_6|^2\alpha^2(1+\mu^2) - G_7G_6^*\alpha\gamma e^{-i(\mathcal{E}_7-\mathcal{E}_6)t'} - G_6G_7^*\alpha\gamma e^{-i(\mathcal{E}_6-\mathcal{E}_7)t'} + \\
& |G_7|^2\gamma^2(1+\lambda^2)\big)|\uparrow\downarrow\rangle\langle\uparrow\downarrow| + \big(-2i|G_6|^2\alpha^2\mu - iG_7G_6^*\alpha\gamma(\lambda+\mu)e^{-i(\mathcal{E}_7-\mathcal{E}_6)t'} \\
& -iG_6G_7^*\alpha\gamma(\lambda+\mu)e^{-i(\mathcal{E}_6-\mathcal{E}_7)t'} - 2i|G_7|^2\gamma^2\lambda\big)|\downarrow\uparrow\rangle\langle\uparrow\downarrow| + \big(2i|G_6|^2\alpha^2\mu + \\
& iG_7G_6^*\alpha\gamma(\lambda+\mu)e^{-i(\mathcal{E}_7-\mathcal{E}_6)t'} + iG_6G_7^*\alpha\gamma(\lambda+\mu)e^{-i(\mathcal{E}_6-\mathcal{E}_7)t'} + \\
& 2i|G_7|^2\gamma^2\lambda\big)|\uparrow\downarrow\rangle\langle\downarrow\uparrow| + \big(|G_6|^2\alpha^2(1+\mu^2) - G_7G_6^*\alpha\gamma e^{-i(\mathcal{E}_7-\mathcal{E}_6)t'} - \\
& G_6G_7^*\alpha\gamma e^{-i(\mathcal{E}_6-\mathcal{E}_7)t'} + |G_7|^2\gamma^2(1+\lambda^2)\big)|\downarrow\uparrow\rangle\langle\downarrow\uparrow| + \big(|G_6|^2\alpha^2 + \\
& G_7G_6^*\alpha\gamma e^{-i(\mathcal{E}_7-\mathcal{E}_6)t'} + G_6G_7^*\alpha\gamma e^{-i(\mathcal{E}_6-\mathcal{E}_7)t'} + |G_7|^2\gamma^2\big)|\downarrow\downarrow\rangle\langle\downarrow\downarrow|.
\end{aligned}
\tag{4.19}
$$

The time dependence of the two-tangle is shown in Fig. 4.2. It shows oscillations as a function of time with the same time period $\pi/(\mathcal{E}_7 - \mathcal{E}_6)$ as that of the chirality, meaning that at the time when chirality rises to its peak, two-qubit entanglement also reaches the maximum and it is always less than one.

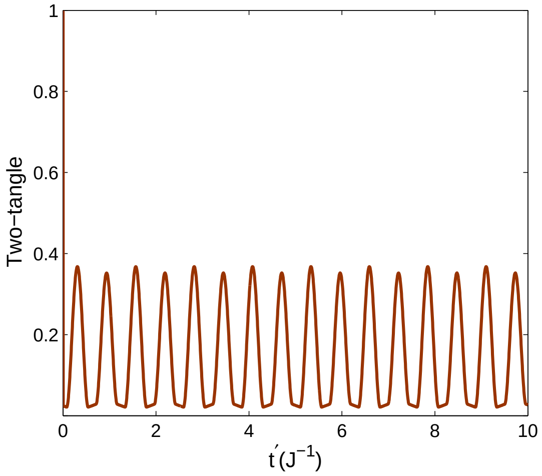

Figure 4.2. – Two-tangle in case of two-excitations ground state $|\phi_7\rangle$ for the following values of the parameters: $-J_1 = J_2 = 1, B = 0.25, d_0 = \wp_0 g_{ME} = 0.05, d_1 = d_0/0.1$.

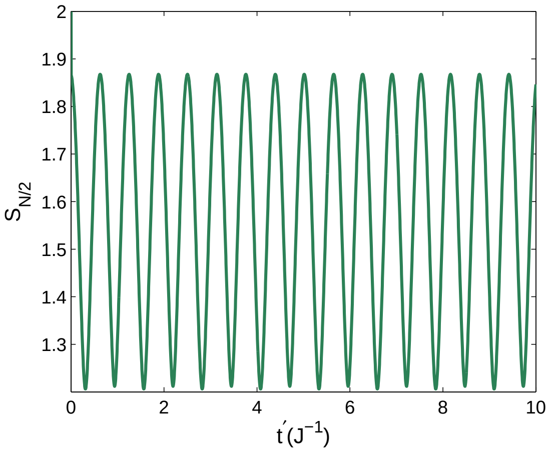

Figure 4.3. – Von Neumann entropy in case of two-excitations ground state $|\phi_7\rangle$ for the following values of the parameters: $-J_1 = J_2 = 1, B = 0.25, d_0 = \wp_0 g_{ME} = 0.05, d_1 = d_0/0.1$.

Fig. 4.3 shows the time dependence of von Neumann entropy $S_{L/2} = -\mathrm{Tr}_{1,\ldots,L/2}[\rho_{1,\ldots,L/2}\log_2(\rho_{1,\ldots,L/2})]$, where the reduced density matrix of first $L/2$ spins is given by $\rho_{1,\ldots,L/2} = \mathrm{Tr}_{L/2+1,\ldots L}(|\psi(t)\rangle\langle\psi(t)|)$. As for the two-tangle the von Neumann entropy is maximum at $t' = 0$. Afterwards the entropy oscillates with time and the period of oscillation is the same as as for the chirality and the two-tangle.

We also plot the von Neumann entropy for different values of the electric field pulse d_1. See Fig. 4.4.

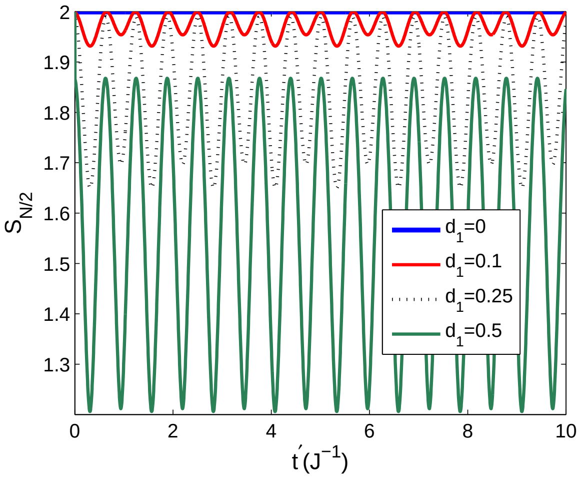

Figure 4.4. – Von Neumann entropy in case of two-excitations ground state $|\phi_7\rangle$ for different values of d_1.

From Fig. 4.4 we see that in the absence of the pulse at $t' = 0$, the von Neumann entropy at maximum value remains constant throughout the observation. By applying the pulse, the entropy decreases and oscillates with time. The amplitude of oscillations grows in proportion to the pulse strength, however its maximum is always less than $S_{N/2} = 2$.

4.2. Numerical simulations

In this section we show some numerical results obtained from exact diagonalization for different length of the chain $N > 4$. As pointed out in the previous section for the four spins case if the system is kept initially in one-excitation ground state, the chirality remains constant with time. The same is true for longer size chains also and the sum of expectation values of two correlation terms $\langle S_i^- S_{i+1}^+ \rangle$ and $\langle S_i^+ S_{i+1}^- \rangle$ add up to constant at any time. However, in the case of higher n-excitations ground states which are prepared with a proper choice of parameters d_0 and B, the chirality shows oscillations with time. We consider the two-excitations ground state for all spin chain length. The plots of Chirality, two-tangle and von Neuman entropy in case of $N = 8$ with two-excitations ground state is presented in Fig. 4.5.

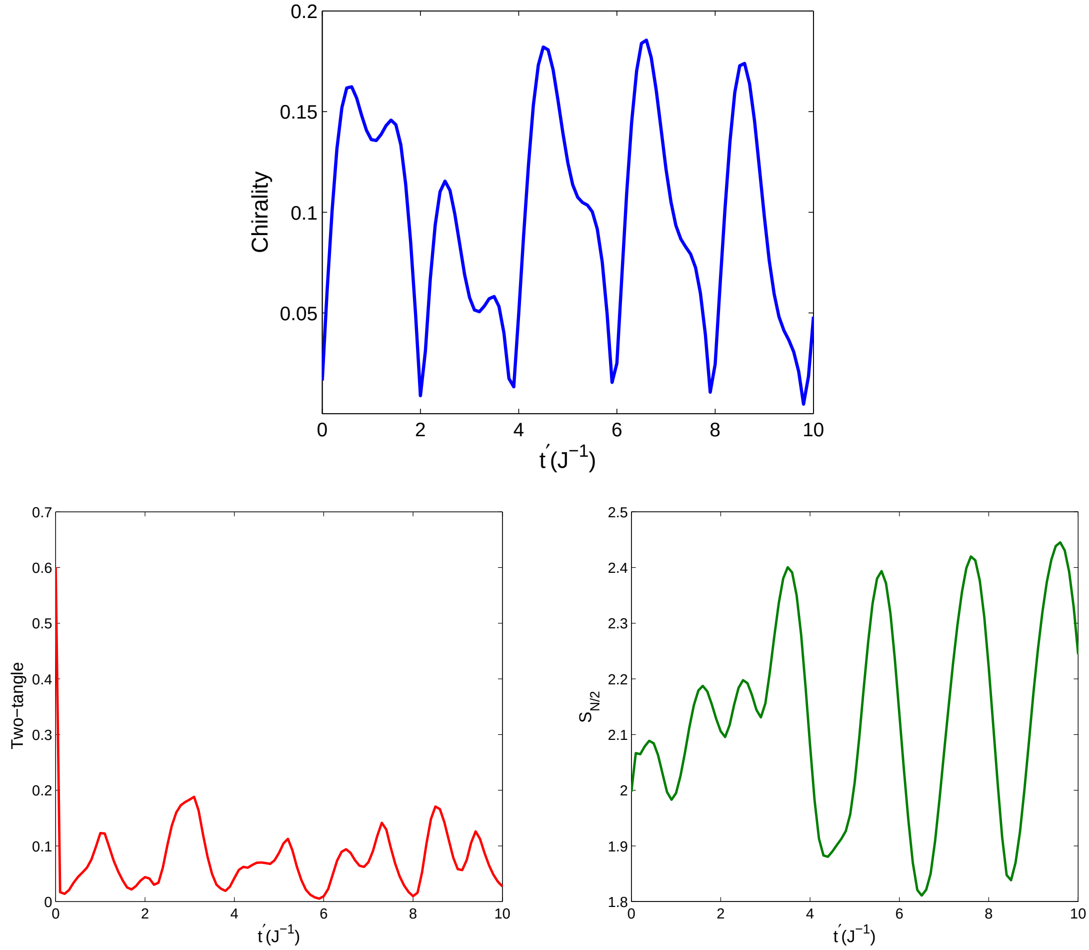

Figure 4.5. – Time dependence of chirality(up panel), two-tangle(down left panel) and von Neumann entropy(down right panel) for N=8, with the two-excitations initial state. The parameters are: $-J_1 = J_2 = 1, B = 0.25, d_0 = \wp_0 g_{ME} = 0.05, d_1 = d_0/0.1$.

Also in this case we analyze the evolution of the von Neuman entropy by varying the pulse strength d_1 in Fig. 4.6.

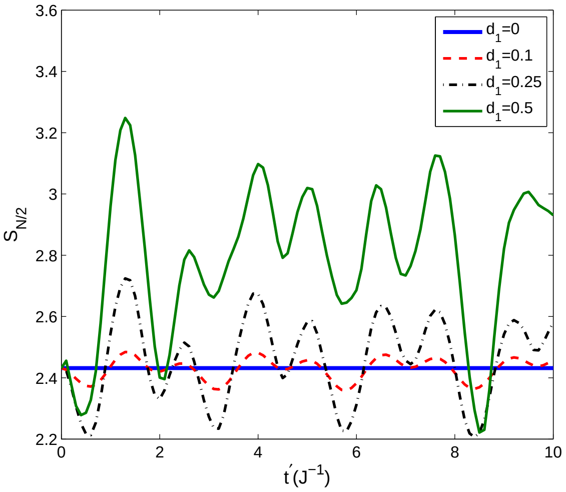

Figure 4.6. – Von Neumann entropy in case of $N = 8$, with the two-excitations ground state for different values of d_1.

From Fig. 4.6 we see that the von Neumann entropy in the absence of pulse is constant with time. However, the value is much less than the maximal entropy $S_{N/2} = N/2$. With increasing the pulse strength, the von Neumann entropy starts oscillating and the peak of entropy is higher than no pulse case i.e. $d_1 = 0$. For very large systems for example $N = 20$ with $N/2$ number of excitations, i.e. $S_z = 0$ sector, we see saturation of the entropy to a high value at a later time. See Fig. 4.7.

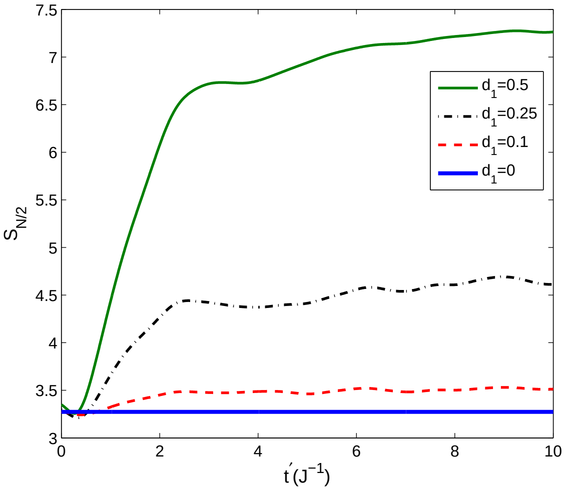

Figure 4.7. – Von Neumann entropy in case of $N = 20$, with $N/2$-excitations ground state for different values of d_1.

In Fig. 4.8 the time evolution of the two-tangle and von Neumann entropy for various sizes of the spin chain with two-excitations ground state are shown.

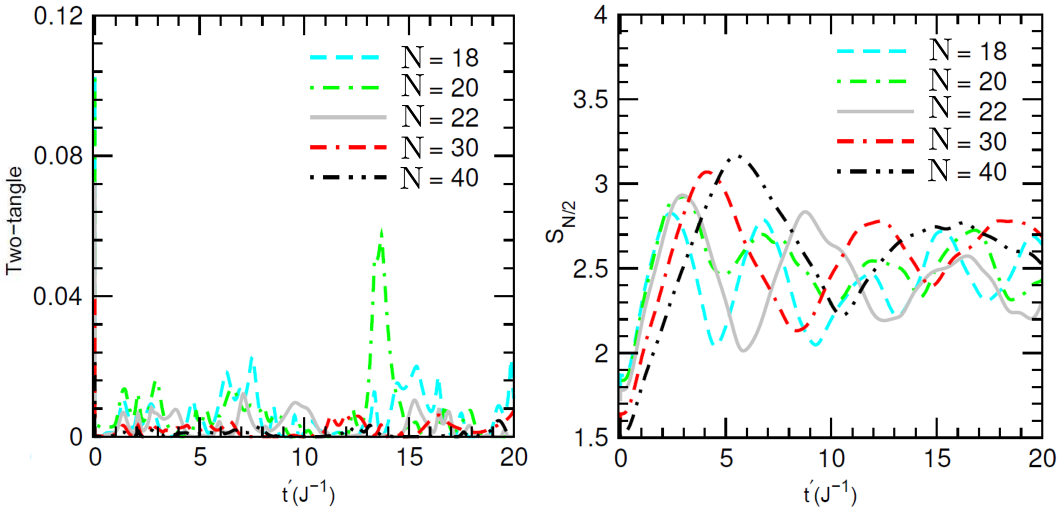

Figure 4.8. – Time dependence of the two-tangle (left panel) and the von Neumann entropy (right panel) for $N = 18, 20, 22, 30, 40$. In all cases the system is in a two-excitations ground state. The strength of the pulse is $d_1 = 0.5$. The spin-exchange couplings and initial electric-field strength are $-J_1 = J_2 = 1, d_0 = \wp_0 g_{ME} = 0.05$ respectively. Adapted from [105].

From the figures we notice that the two-tangle decreases significantly by increasing the size. For system size $N \geq 18$ the two-tangle starts to disappear during the pulse-free time evolution. The frequency of oscillations decreases significantly. For larger sizes when the two-tangles vanishes, we expect the entanglement to exist in pure multipartite form. This may be the reason for a large von Neumann entropy in large system sizes.

4.3. Dynamical phase transition

Recently Heyl et al [106] discussed the connection between canonical partition function $Z = \mathrm{Tr} e^{\beta H}$ and return probability of the system to the initial state while going through a non trivial time evolution. This return probability is known as Loschmidt echo and its amplitude is given by

$$G(t) = \langle \psi_0 | e^{-i\hat{H}t} | \psi_0 \rangle \tag{4.20}$$

The non-analyticity in time manifests a dynamical phase transition. The zeros of the partition function Z are searched in the complex inverse temperature β plane, while the zeros of the Loschmidt echo $G(t)$ lie on the real time axis. The quantity of interest is the rate function of the return probability given by

$$l(t) = -\lim_{N\to\infty} \frac{1}{N} \ln |G(t)|^2. \tag{4.21}$$

The nonanalytical points of $l(t)$ can be obtained by finding the zeros of $G(t)$. In the thermodynamic limit as the free energy density signifies the nonanalyticity accompanying to the phase transition the rate function $l(t)$ reflects the nonanalyticity associated with dynamical phase transition. Heyl et al. used this protocol to study quenches in a transverse field Ising spin model, which exhibits a quantum phase transition between ferromagnetic and paramagnetic ground states. In recent works the protocol set by Heyl et. al has been used to progress the study of dynamical phase transition in different models [107–114].

In this section we consider a sudden electric field quench and investigate the dynamical quantum phase transitions for the quenched dynamics. For this purpose, we combined the Weierstrass factorization technique for entire functions and Lanczos exact diagonalization method. The analytical results, including the rate function of Loschmidt echo for a system of $N = 4$, spins are obtained. The system is initially prepared in the ground state of $\hat{H} = \hat{H}_0 + \hat{H}_1$, and then at $t = 0$ it is suddenly quenched to $\hat{H} \to \hat{H}_0$ ($\hat{H}_1$ is absent for $t > 0$). The expression for the Loschmidt echo Eq. (4.20) can be written now as

$$G(t) = \langle \psi_0 | e^{-i\hat{H}_0 t} | \psi_0 \rangle = \sum_{n,m} Q_{0n} H_{nm} Q_{m0}, \tag{4.22}$$

where $Q_{n0} = \langle \phi_n | \psi_0 \rangle$, $H_{nm} = \langle \phi_n | \exp(-i\hat{H}_0 t) | \phi_m \rangle$, $|\psi_0\rangle$ and $|\phi_n\rangle$ are the ground state of Hamiltonian $\hat{H} = \hat{H}_0 + \hat{H}_1$ and the n-th eigenstate of the Hamiltonian $\hat{H}_0$ respectively. Based on the Weierstrass theorem for entire functions, an entire function $f(z)$ with the zeros z_j, $j = 1, 2, 3, \cdots$ can be written as

$$f(z) = e^{g(z)} \prod_j \left(1 - \frac{z}{z_j}\right), \tag{4.23}$$

where $g(z)$ is another entire function of z. The zeros of the Weierstrass factorization are related to a dynamical phase transition. The non-analytic part of the function $\ln|f(z)|$ in Eq. (4.23) is determined by zeros z_j. Assuming $z = it$ and $f(z)$ as $G(t)$(given by Eq. (4.20)), the rate function $l(t)$, Eq. (4.21) reads

$$l(t) = -\frac{2}{N}\left[|g(t)| + \sum_j \ln\left|1 - \frac{t}{t_j}\right|\right]. \tag{4.24}$$

For the system of four spins with two-excitations ground state $|\phi_7\rangle$, the return probability is determined by

$$G(t) = ae^{-i\mathcal{E}_6 t} + be^{-i\mathcal{E}_7 t},$$

$$a = [\alpha\gamma'(4+\mu\lambda')]^2,\ b = [\gamma\gamma'(4+\lambda\lambda')]^2. \tag{4.25}$$

Here λ,γ and λ' and γ' are obtained via substituting $\wp$ by d_0 and d_1+d_0 respectively in Eq. (3.8) in chapter 3. Therefore we can obtain the zeros of $G(t)$ by solving $G(t) = 0$ as follows

$$t_k = \frac{1}{\mathcal{E}_6 - \mathcal{E}_7}\left(i\ln\left(\frac{a}{b}\right) - \pi(2k+1)\right),\ \ k = 0, \pm1, \pm2, \cdots \tag{4.26}$$

Real and imaginary parts of $\theta_k = it_k$ can be separately written as

$$\Re(\theta_k) = -\frac{2}{\sqrt{(J_1-4J_2)^2+8d_0^2}}\ln\left(\frac{\alpha(2+\mu\lambda')}{\beta(2+\lambda\lambda')}\right),$$

$$\Im(\theta_k) = \frac{\pi(2n+1)}{\sqrt{(J_1-4J_2)^2+8d_0^2}}. \tag{4.27}$$

In Fig. 4.9 we plot the zeros for different values of quench strength.
As it is clear a very large electric field $d_1 = 100$ is needed for real part to approach zero.

Another interesting quantity which is related to the entanglement spectrum is Schmidt gap [107–114]. The entropy of entanglement shows a logarithmic behavior with the system size dependence at the quantum critical point $S \sim c\log l$ and close to critical point $S \sim c\log\xi$ where l is the size of the block, c is the central charge of the conformal field theory describing the quantum phase transition, and ξ is the correlation length [115]. Away from the critical point the system can be characterized by the entanglement spectrum [116, 117, 119, 120] i.e. the eigenvalues of the reduced density matrix of one of the two partitions while tracing out the degrees of freedom of the other partition. This entanglement spectrum is an accepted tool

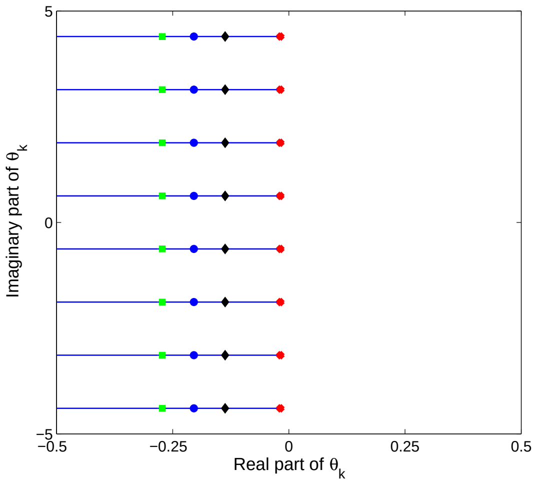

Figure 4.9. – Zeros of $\theta_k = it_k$ in case of 4-spins system with two-excitations ground state for $k = -4, -3, ..., 3$ and $J_1 = -J_2 = -1.0, B = 0.25, d0 = 0.05$. Green squares, blue circles, black diamonds, and red points correspond to $d_1 = 2.5, d_1 = 3.5, d_1 = 5.49$, and $d_1 = 100$ respectively.

to characterize the many body system. The gap between the two largest eigenvalues called Schmidt gap is considered to capture the phase transition. The zeros of the Schmidt gap can deliver information about the quantum critical point [117]. We study the time evolution of Schmidt gap $\Delta = \lambda_a - \lambda_b$ ($\lambda_a$and λ_b are the two largest eigenvalues of the reduced density matrix) for the quench protocol followed in this section.
Fig. 4.10 shows the quench protocol applied to 4-spin system with two-excitations ground state indicating an onset of a dynamical transition. However, small system of four spins do not possess a well-developed phase transition behavior, but kind of precursors.

Signature of quantum phase transition can be observed in the case of a pulse induced dynamics as well. See Fig. 4.11. In this case we used the following expression for Loschmidt echo

$$G(t) = |G_6|^2 e^{-i\mathcal{E}_6 t} + |G_7|^2 e^{-i\mathcal{E}_7 t} \tag{4.28}$$

The explicit form of G_6, G_7 were derived in Eq. (4.12).

As we see the non-analytic behavior of the rate function is correlated with the minimum of Schmidt gap and the Fisher zeros cross the real axis in this case.

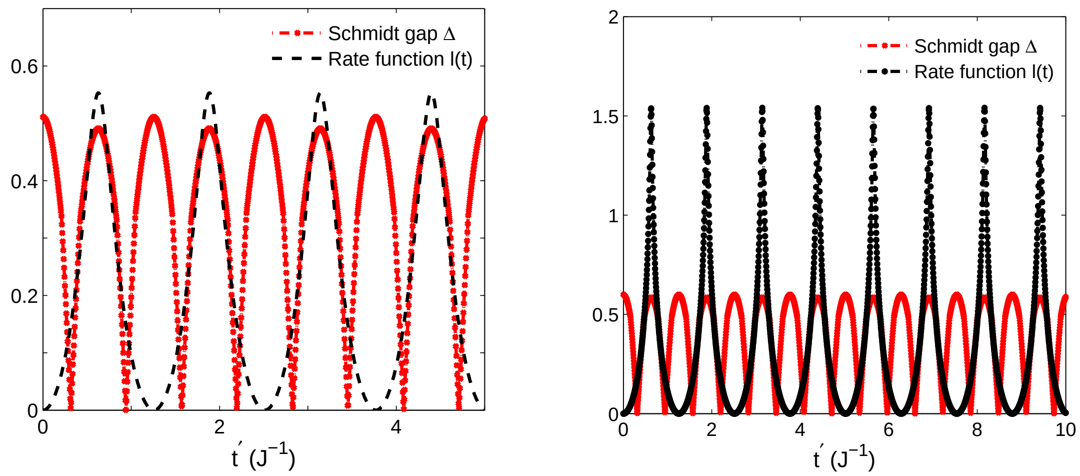

Figure 4.10. – Rate function and Schmidt gap in 4-spins system with two-excitations ground state. The parameters are $-J_1 = J_2 = 1, d_0 = \wp_0 g_{ME} = 0.05$. For left panel $d_1 = 5.49$ and for right panel $d_1 = 100$ correspond to black diamond points and red points in Fig. 4.9 respectively.

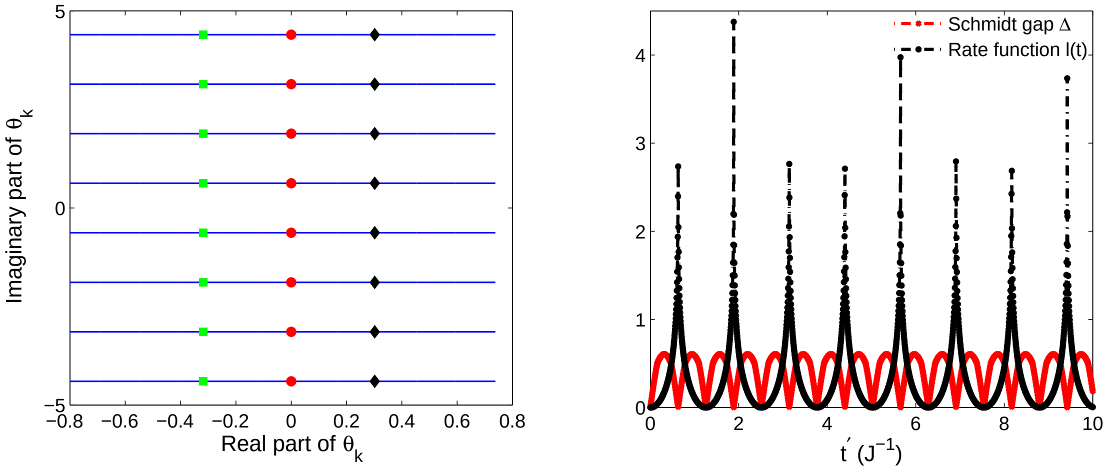

Figure 4.11. – Left panel: Zeros of $\theta_k = it_k$ in the case of applied pulses to 4-spins system with two-excitations ground state for $k = -4, -3, ..., 3$ and $J_1 = -J_2 = -1.0, B = 0.25, d0 = 0.001$. Green squares, red circles, black diamonds correspond to $d_1 = 0.3, d_1 = 0.5554$, and $d_1 = 0.8$ respectively. Right panel: Rate function and Schmidt gap for $d_1 = 0.5554$ (red circles).

In the following we show the exact numerical calculations for $N = 18$ and $N = 22$. In both cases the initial state taken to be the ground state in two-excitations sector. In order to detect the transition, the parameters d_1 and d_0 have to be chosen carefully. For the parameters d_1 and d_0, for which there is a dynamical phase transition, non-analyticity at the points t'' in the rate function, we see a nice pattern in the Schmidt gap too. We can see that at the onset of the dynamical phase transition, the Schmidt gap vanishes and remains zero in the time interval in which the system undergoes a dynamical phase transition. We can estimate the critical point by just looking at the pattern of the Schmidt gap. For example, in Fig. 4.12, left panel the Schmidt gap is zero for $4.75 < t' < 11.75$ and the critical point is just at the middle $t = 8.25$ of the interval or in right panel the Schmidt gap is zero for $5.56 < t' < 13.42$ and the critical point $t'' = 9.41$ is close to the middle $t' = 9.49$ of the interval. At times when the rate function touches the minimum, the Schmidt gap reaches its maximum.

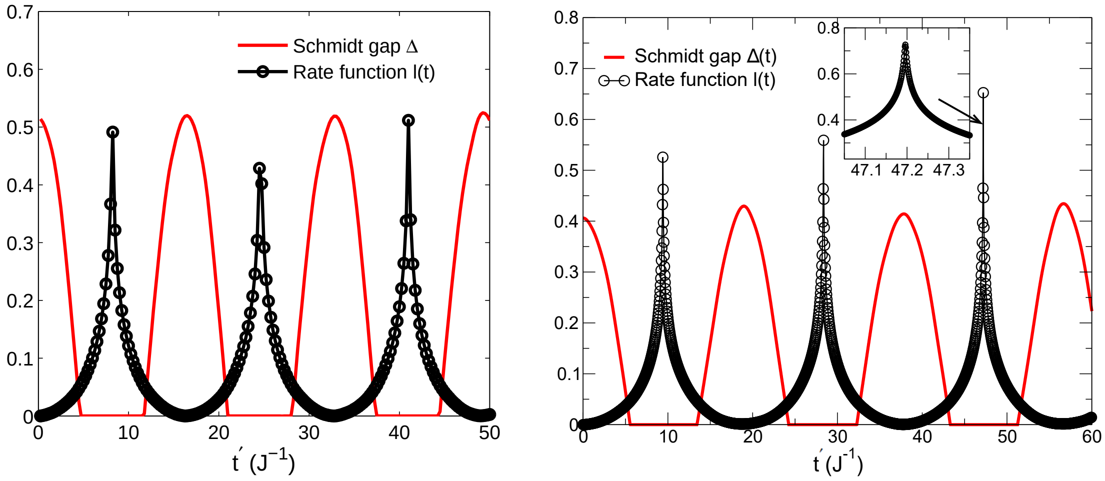

Figure 4.12. – Left panel: The rate function and the Schmidt gap for a periodic chain of size $N = 18$. The parameters are $J_2 = -J_1 = 1, d_1 = 2.34, d_0 = 0.098$. Right panel: The rate function and the Schmidt gap for a periodic chain of size $N = 22$ for the parameters $J_2 = -J_1 = 1, d_1 = 0.44, d_0 = 0.057$. The peaks of the rate function at time $t'' \approx 9.41, 28.36, 47.20, ...$ correspond to the dynamical phase transitions. The inset shows a zoom into the cusp region at one of the non-analytic point. Adapted from [105].

4.4. Summary

The influence of a short electric field pulse has been studied showing that an electric field pulse may switch the system into an incommensurate chiral phase. Time evolution of chirality shows a signature of the spin configuration in the new phase. We calculated the chirality, one-tangle, two-tangle and von Neumann entropy using one- and two-excitations ground states. We found that all the measured quantities are constant in one-excitation ground state and oscillating with time in n (> 1)-excitations ground state. We could also see that the chirality and two-tangle go together while two-tangle and von Neumann entropy are complementary to each other with the same period of oscillations. We extended our study of $N > 4$ spins by using exact diagonalization method. We found that two-tangle is vanishing as the size increases. Chirality oscillates with time but its peak value is not vanishing as compared to the case of two-tangle which vanishes for size $N > 18$ spins. We could see a large von Neumann entropy even for the size $N > 18$ spins. This confirms that the chirality goes along with mulipartite entanglement in these systems. In the end, we have used a protocol to calculate the Loschmidt echo and rate function which signifies a dynamical phase transition between commensurate to incommensurate spiral phases.

5. Constructing quantum Otto heat engine

In this chapter we study a quantum Otto heat engine operating on the basis of a helical spin-1/2 multiferroic chain introduced in chapter 2 as a working substance. See Fig. 5.1.

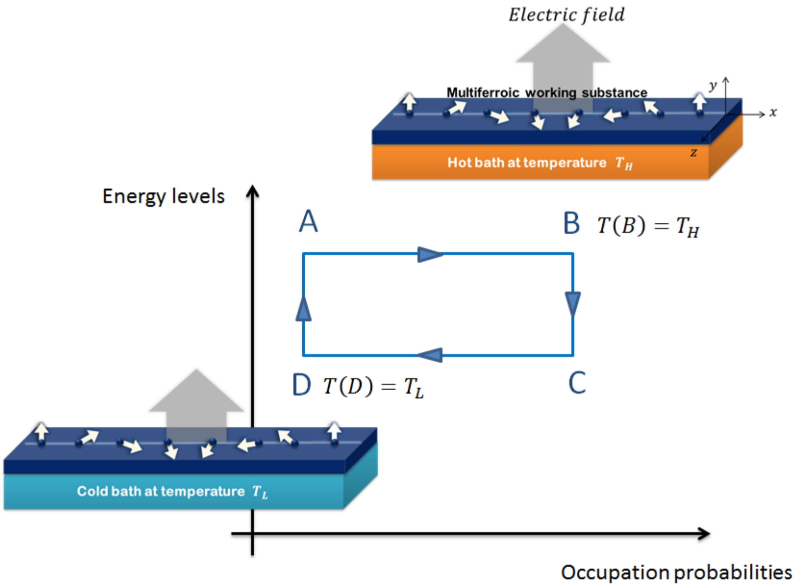
Electric field
Multiferroic working substance
y
x
z
Hot bath at temperature T_H
Energy levels
A
B $T(B) = T_H$
D $T(D) = T_L$
C
Cold bath at temperature T_L
Occupation probabilities

Figure 5.1. – Scheme of the quantum Otto cycle based on a spin-spiral multiferroic chain. Reproduced from [118].

The cycle consists of two isochoric strokes, $A \rightarrow B$, $C \rightarrow D$ and two quantum (or thermodynamic) adiabatic strokes, $B \rightarrow C$, $D \rightarrow A$. During the stroke $A \rightarrow B$ the system is attached to a hot bath with a temperature T_H absorbing energy and reaches to the thermodynamic equilibrium associated with the level populations $P_n^B\big(E_n(\wp), T_H\big)$. During the stroke $C \rightarrow D$ the interaction with a cold bath with a temperature T_L is done and the system releases energy and reaches to thermodynamic equilibrium state associated with the level populations $P_n^D\big(E_n(\wp_1), T_L\big)$. During the two thermodynamic adiabatic strokes the amplitude of the electric field is changed so that $\Delta E_n = E_n(\wp) - E_n(\wp_1)$, resulting in a change of energy levels and the system performs work.

In the next section we first analyze analytically the system of four spins and then in the other section we numerically generalize the treatment for larger systems.

5.1. Four spins

To study the thermal chirality, entanglement, and the cycle efficiency in the system of four spins first of all, we need to construct the density matrix $\hat{\rho}$ defined by the equilibrium Gibbs distribution

$$\hat{\rho} = Z^{-1} \sum_{n=1}^{16} \exp[-\beta E_n] |\psi_n\rangle\langle\psi_n|, \qquad Z = \sum_{n=1}^{16} \exp[-\beta E_n], \tag{5.1}$$

where $|\psi_n\rangle$ and E_n are the eigenfunctions and eigenvalues of Eq. (3.2) given explicitly in Eq. (3.6)-Eq. (3.9). The mean value of the z component of the vector chirality (VC) is obtained from

$$\begin{aligned} \langle \kappa_i \rangle = \langle (\vec{S}_i \times \vec{S}_{i+1})^z \rangle = \mathrm{Tr}(\hat{\rho}(\vec{S}_i \times \vec{S}_{i+1})^z) = \\ \frac{1}{Z}(e^{-\beta E_2} - e^{-\beta E_3} + 8\alpha^2 \mu e^{-\beta E_6} + 8\gamma^2 \lambda e^{-\beta E_7} - e^{-\beta E_{12}} + e^{-\beta E_{13}}). \end{aligned} \tag{5.2}$$

The dependence of the thermal chirality on T and B are plotted in Fig. 5.2 and Fig. 5.3.

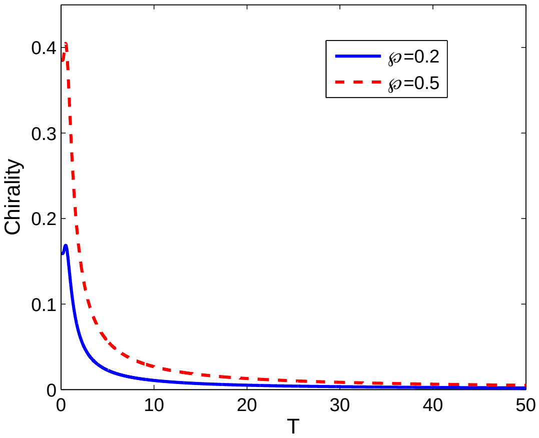

Figure 5.2. – Chirality as a function of the temperature for different values of the electric field. The parameters are: $-J_1 = J_2 = 1, B = 0.25$.

Fig. 5.2 shows that with increasing temperature the thermal chirality undergoes a strong change and it is almost zero at high enough temperatures.
From Fig. 5.3 one can see that with increasing the magnetic field B, the thermal chirality decreases. For calculating the pair concurrence between two arbitrary spins of the working substance based on Eq. (2.21) we derive three matrices R_{12}, R_{13}, R_{14} as follows

$$R_{12} = \frac{1}{Z^2} \begin{pmatrix} a_1 d_1 & 0 & 0 & 0 \\ 0 & b_1^2 + |c_1|^2 & 2b_1 c_1 & 0 \\ 0 & 2b_1 c_1^* & b_1^2 + |c_1|^2 & 0 \\ 0 & 0 & 0 & a_1 d_1 \end{pmatrix},$$

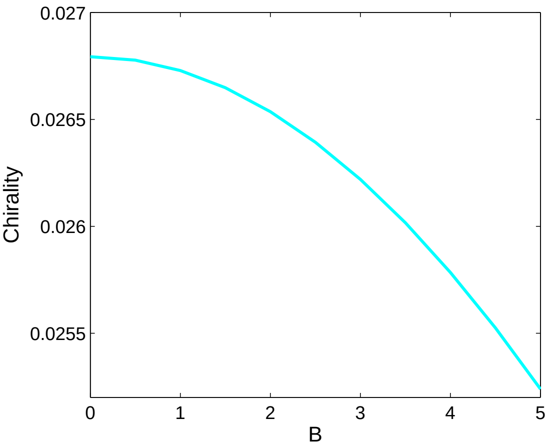

Figure 5.3. – Chirality as a function of B for the parameters $-J_1 = J_2 = 1, \wp = 0.5, T = 10$.

$$R_{13} = \frac{1}{Z^2}\begin{pmatrix} a_2 b_2 & 0 & 0 & 0 \\ 0 & c_2^2 + |d_2|^2 & 2c_2 d_2 & 0 \\ 0 & 2c_2 d_2^* & c_2^2 + |d_2|^2 & 0 \\ 0 & 0 & 0 & a_2 b_2 \end{pmatrix},$$

$$R_{14} = \frac{1}{Z^2}\begin{pmatrix} a_1 d_1 & 0 & 0 & 0 \\ 0 & b_1^2 + |c_1|^2 & 2b_1 c_1^* & 0 \\ 0 & 2b_1 c_1 & b_1^2 + |c_1|^2 & 0 \\ 0 & 0 & 0 & a_1 d_1 \end{pmatrix}, \tag{5.3}$$

where the parameters $a_{1,2}, b_{1,2}, c_{1,2}, d_{1,2}$ are defined as

$$\begin{aligned} a_1 = {} & e^{-\beta E_1} + \tfrac{1}{2}(e^{-\beta E_2} + e^{-\beta E_3} + e^{-\beta E_4} + e^{-\beta E_5}) + \alpha^2 e^{-\beta E_6} + \gamma^2 e^{-\beta E_7} \\ & + \tfrac{1}{6} e^{-\beta E_8} + \tfrac{1}{12} e^{-\beta E_9} + \tfrac{1}{2} e^{-\beta E_{10}}, \end{aligned}$$

$$\begin{aligned} b_1 = {} & \tfrac{1}{4}(e^{-\beta E_2} + e^{-\beta E_3} + e^{-\beta E_4} + e^{-\beta E_5}) + \alpha^2(1+\mu^2) e^{-\beta E_6} + \gamma^2(1+\lambda^2) e^{-\beta E_7} \\ & + \tfrac{1}{3} e^{-\beta E_8} + \tfrac{5}{12} e^{-\beta E_9} + \tfrac{1}{2} e^{-\beta E_{11}} + \tfrac{1}{4}(e^{-\beta E_{12}} + e^{-\beta E_{13}} + e^{-\beta E_{14}} + e^{-\beta E_{15}}), \end{aligned}$$

$$\begin{aligned} c_1 = {} & \tfrac{i}{4}(e^{-\beta E_2} - e^{-\beta E_3}) - \tfrac{1}{4}(e^{-\beta E_4} - e^{-\beta E_5}) + 2i\alpha^2 \mu e^{-\beta E_6} + 2i\gamma^2 \lambda e^{-\beta E_7} \\ & + \tfrac{1}{3}(e^{-\beta E_8} - e^{-\beta E_9}) - \tfrac{i}{4}(e^{-\beta E_{12}} - e^{-\beta E_{13}}) + \tfrac{1}{4}(e^{-\beta E_{14}} - e^{-\beta E_{15}}), \end{aligned}$$

$$\begin{aligned} d_1 = {} & \alpha^2 e^{-\beta E_6} + \gamma^2 e^{-\beta E_7} + \tfrac{1}{6} e^{-\beta E_8} + \tfrac{1}{12} e^{-\beta E_9} + \tfrac{1}{2} e^{-\beta E_{10}} \\ & + \tfrac{1}{2}(e^{-\beta E_{12}} + e^{-\beta E_{13}} + e^{-\beta E_{14}} + e^{-\beta E_{15}}) + e^{-\beta E_{16}}, \end{aligned}$$

$$
\begin{aligned}
a_2 = {} & e^{-\beta E_1} + \tfrac{1}{2}(e^{-\beta E_2} + e^{-\beta E_3} + e^{-\beta E_4} + e^{-\beta E_5}) + \alpha^2\mu^2 e^{-\beta E_6} \\
& + \gamma^2\lambda^2 e^{-\beta E_7} + \tfrac{1}{6}e^{-\beta E_8} + \tfrac{1}{3}e^{-\beta E_9},
\end{aligned}
$$

$$
\begin{aligned}
b_2 = {} & \alpha^2\mu^2 e^{-\beta E_6} + \gamma^2\lambda^2 e^{-\beta E_7} + \tfrac{1}{6}e^{-\beta E_8} + \tfrac{1}{3}e^{-\beta E_9} \\
& + \tfrac{1}{2}(e^{-\beta E_{12}} + e^{-\beta E_{13}} + e^{-\beta E_{14}} + e^{-\beta E_{15}}) + e^{-\beta E_{16}},
\end{aligned}
$$

$$
\begin{aligned}
c_2 = {} & \tfrac{1}{4}(e^{-\beta E_2} + e^{-\beta E_3} + e^{-\beta E_4} + e^{-\beta E_5}) + 2\alpha^2 e^{-\beta E_6} + 2\gamma^2 e^{-\beta E_7} + \tfrac{1}{3}e^{-\beta E_8} \\
& + \tfrac{1}{6}e^{-\beta E_9} + \tfrac{1}{2}e^{-\beta E_{10}} + \tfrac{1}{2}e^{-\beta E_{11}} + \tfrac{1}{4}(e^{-\beta E_{12}} + e^{-\beta E_{13}} + e^{-\beta E_{14}} + e^{-\beta E_{15}}),
\end{aligned}
$$

$$
\begin{aligned}
d_2 = {} & \tfrac{-1}{4}(e^{-\beta E_2} + e^{-\beta E_3}) + \tfrac{1}{4}(e^{-\beta E_4} + e^{-\beta E_5}) - 2\alpha^2 e^{-\beta E_6} - 2\gamma^2 e^{-\beta E_7} \\
& + \tfrac{1}{3}(e^{-\beta E_8} + e^{-\beta E_9}) - \tfrac{1}{4}(e^{-\beta E_{12}} + e^{-\beta E_{13}}) - \tfrac{1}{4}(e^{-\beta E_{14}} - e^{-\beta E_{15}}).
\end{aligned}
\tag{5.4}
$$

Therefore for the different pair concurrences we deduce

$$
\begin{aligned}
C_{12} = C_{14} &= \frac{2}{Z}\max\{|c_1| - \sqrt{a_1 d_1}, 0\}, \\
C_{13} &= \frac{2}{Z}\max\{|d_2| - \sqrt{a_2 b_2}, 0\}.
\end{aligned}
\tag{5.5}
$$

Taking into account Eq.(5.5) for the two-tangle defined by Eq. (2.22) we obtain

$$
\begin{aligned}
&|c_1| > \sqrt{a_1 d_1}, |d_2| > \sqrt{a_2 b_2}: \quad \tau_2 = \frac{8(|c_1| - \sqrt{a_1 d_1})^2 + 4(|d_2| - \sqrt{a_2 b_2})^2}{Z^2}, \\
&|c_1| > \sqrt{a_1 d_1},\ |d_2| < \sqrt{a_2 b_2}: \quad \tau_2 = \frac{8(|c_1| - \sqrt{a_1 d_1})^2}{Z^2}, \\
&|c_1| < \sqrt{a_1 d_1}, |d_2| > \sqrt{a_2 b_2}: \quad \tau_2 = \frac{4(|d_2| - \sqrt{a_2 b_2})^2}{Z^2}, \\
&|c_1| < \sqrt{a_1 d_1}, |d_2| < \sqrt{a_2 b_2}: \quad \tau_2 = 0.
\end{aligned}
\tag{5.6}
$$

As demonstrated from Eq.(5.6) the two-tangle depends on several inequalities between the parameters $a_{1,2}, b_{1,2}, c_1, d_{1,2}$ which are functions of the temperature T, driving electric field $\wp$ and magnetic field B. So depending on these parameters the system can be entangled or disentangled. For the given values of the electric and magnetic fields there is a threshold temperature $T_c(\wp, B)$ which defines the entangled and disentangled regimes. The dependence on the amplitude of the electric field $\wp$ is shown in Fig. 5.4.

As we see from Fig. 5.4, τ_2 is finite for large enough amplitude of the electric field $\wp$. Essentially it is zero until the electric field amplitude becomes quite significant.

In Fig. 5.5 the threshold temperatures for different values of the electric field $\wp$ are defined in a way that below these temperatures τ_2 is finite and above them $\tau_2 = 0$.

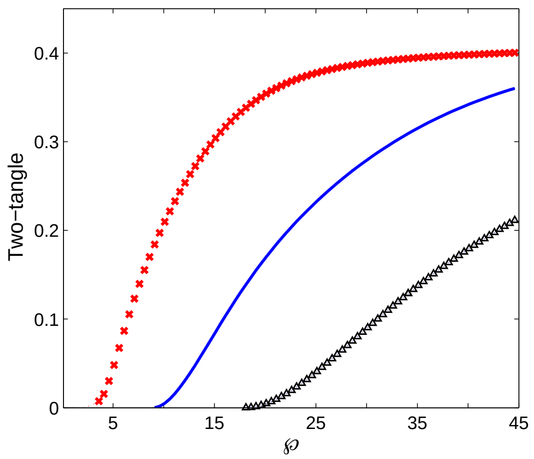

Figure 5.4. – Two-tangle as a function of the electric field ℘ for different temperatures $T = 2$(red cross line), $T = 5$(blue solid line), $T = 10$(black triangle line). The parameters are: $-J_1 = J_2 = 1, B = 0.25$.

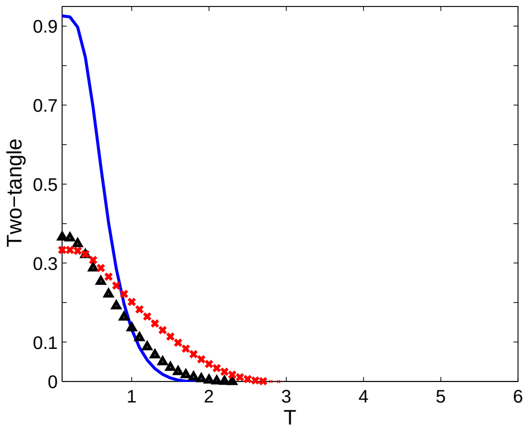

Figure 5.5. – Two-tangle as a function of the temperature for different values of the electric field $\wp = 0.5$(blue solid line), $\wp = 3$(black triangle line), $\wp = 5$(red cross line). The parameters are: $-J_1 = J_2 = 1, B = 0.25$. The threshold temperatures are $T_c = 1.9, \quad T_c = 2.3, \quad T_c = 2.9$, respectively.

For one-tangle $\tau_1 = 4\det\rho_1 = 4\det(\mathrm{Tr}_{2,3,4}(\hat{\rho}))$ which quantifies the nonlocal many-body correlations in the system we obtain

$$\begin{aligned}\tau_1 = \frac{4}{Z^2}\{&e^{-\beta E_1} + \frac{3}{4}(e^{-\beta E_2} + e^{-\beta E_3} + e^{-\beta E_4} + e^{-\beta E_5}) + \alpha^2(2+\mu^2)e^{-\beta E_6} \\ &+\gamma^2(2+\lambda^2)e^{-\beta E_7} + \frac{1}{2}(e^{-\beta E_8} + e^{-\beta E_9} + e^{-\beta E_{10}} + e^{-\beta E_{11}}) \\ &+\frac{1}{4}(e^{-\beta E_{12}} + e^{-\beta E_{13}} + e^{-\beta E_{14}} + e^{-\beta E_{15}})\}\times\end{aligned}$$

$$\begin{aligned}&\{\frac{1}{4}(e^{-\beta E_2}+e^{-\beta E_3}+e^{-\beta E_4}+e^{-\beta E_5})+\alpha^2(2+\mu^2)e^{-\beta E_6}\\&+\gamma^2(2+\lambda^2)e^{-\beta E_7}+\frac{1}{2}(e^{-\beta E_8}+e^{-\beta E_9}+e^{-\beta E_{10}}+e^{-\beta E_{11}})\\&+\frac{3}{4}(e^{-\beta E_{12}}+e^{-\beta E_{13}}+e^{-\beta E_{14}}+e^{-\beta E_{15}})+e^{-\beta E_{16}}\}.\end{aligned} \tag{5.7}$$

In the high temperature limit, the one-tangle is unit $\tau_1 = 1$. See Fig. 5.6. In fact the one-tangle is very robust and is practically not affected by the temperature.

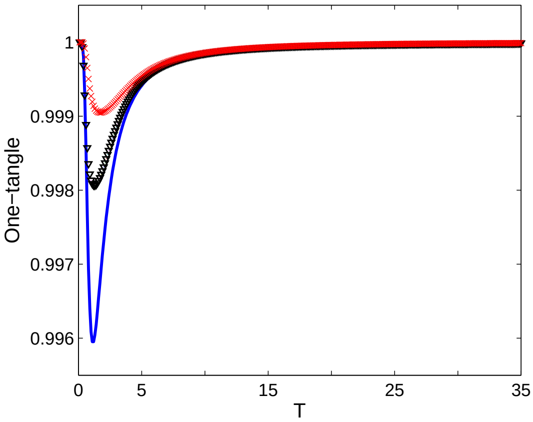

Figure 5.6. – One-tangle as a function of the temperature for different values of the electric field $\wp = 0.5$(blue solid line), $\wp = 3$(black triangle line), $\wp = 5$(red cross line). The parameters are: $-J_1 = J_2 = 1, B = 0.25$.

In contrast to the pair correlations, the collective entanglement τ_1 is different from zero for an arbitrary electric field. See Fig. 5.7. Another remarkable difference is that even very weak electric field is able to generate nonlocal entanglement τ_1.

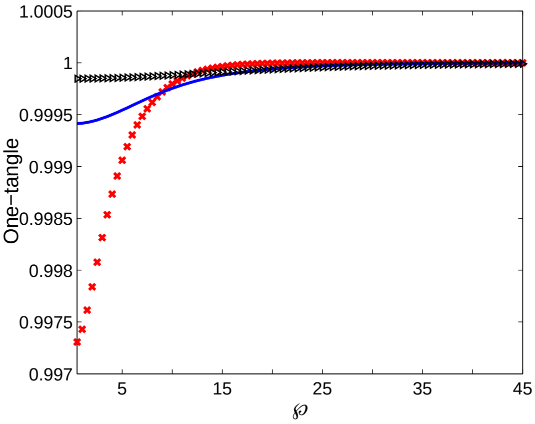

Figure 5.7. – One-tangle as a function of the electric field $\wp$ for different temperatures $T = 2$(red cross line), $T = 5$(blue solid line), $T = 10$(black triangle line). The parameters are: $-J_1 = J_2 = 1, B = 0.25$.

The ratio between two- and one-tangle is plotted in Fig. 5.8. It is clear that the amount of thermal entanglement stored in the nonlocal correlations τ_1 is always larger than the thermal entanglement of the pair correlations in the system i.e. $\tau_1 > \tau_2$. Also by increasing the electric field this ratio is increasing as well.

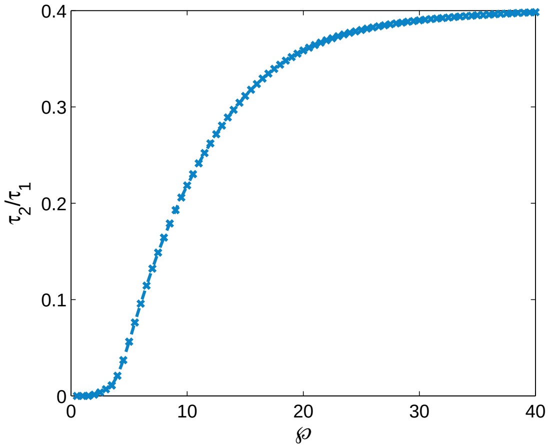

Figure 5.8. – Ratio between two- and one-tangle as a function of the external electric field for the following values of the parameters $-J_1 = J_2 = 1, B = 0.25, T = 1.9$.

Due to the coupling of the magnetic field to the magnetization which is a conserved quantity in the model, the magnetic field dependence of both types of entanglement, τ_1 and τ_2 is clear. With increasing B the entanglements decrease. See Fig. 5.9.

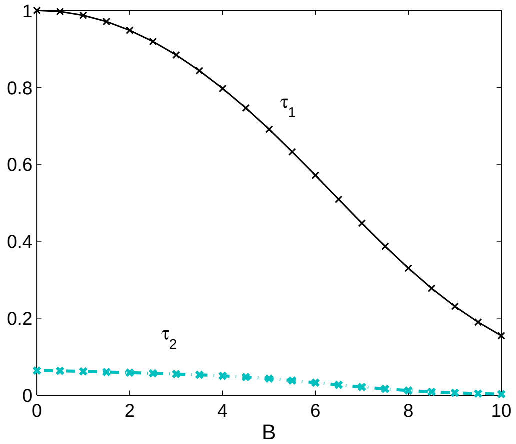

Figure 5.9. – One- and two-tangle as a function of the magnetic filed B. The parameters are: $-J_1 = J_2 = 1, T = 2, \wp = 5.5$.

5.1.1. Magnetic and electric susceptibilities

According to Eq. (2.17), the expressions for the fidelity related to the electric and magnetic fields can be written as

$$
\begin{aligned}
F_{\wp}(\beta,\wp,\wp+\delta\wp) &= \exp\Big[-\frac{\beta(\delta\wp)^2}{8}\chi(\wp)\Big],\\
F_{B}(\beta,B,B+\delta B) &= \exp\Big[-\frac{\beta(\delta B)^2}{8}\chi(B)\Big].
\end{aligned}
\tag{5.8}
$$

Here $\chi(\wp)=-\frac{\partial^2 F}{\partial\wp^2}, \chi(B)=-\frac{\partial^2 F}{\partial B^2}$ are the susceptibilities to an external electric and magnetic fields at constant temperature and $F=-\beta\ln Z$ is the free energy of the system.

After some calculations we obtain

$$
\begin{aligned}
\chi(B) = -\frac{\partial^2 F}{\partial B^2} =&\\
&\frac{\sum\limits_{n,m=1}^{16}[\beta(\frac{dE_n}{dB})^2-\beta(\frac{dE_n}{dB})(\frac{dE_m}{dB})-\frac{d^2E_n}{dB^2}]\exp[-\beta(E_n+E_m)]}{(\sum\limits_{n=1}^{16}\exp[-\beta E_n])^2}\\
= \frac{\beta}{Z^2}\big[&e^{-\beta E_1}(e^{-\beta E_2}+e^{-\beta E_3}+e^{-\beta E_4}+e^{-\beta E_5}+4e^{-\beta E_6}+4e^{-\beta E_7}+4e^{-\beta E_8}\\
&+4e^{-\beta E_9}+4e^{-\beta E_{10}}+4e^{-\beta E_{11}}+9e^{-\beta E_{12}}+9e^{-\beta E_{13}}+9e^{-\beta E_{14}}+9e^{-\beta E_{15}})\\
&+e^{-\beta E_{16}}(9e^{-\beta E_2}+9e^{-\beta E_3}+9e^{-\beta E_4}+9e^{-\beta E_5}+4e^{-\beta E_6}+4e^{-\beta E_7}+\\
&+4e^{-\beta E_8}+4e^{-\beta E_9}+4e^{-\beta E_{10}}+4e^{-\beta E_{11}}+e^{-\beta E_{12}}+e^{-\beta E_{13}}+e^{-\beta E_{14}}+e^{-\beta E_{15}})\\
&+(e^{-\beta E_2}+e^{-\beta E_3}+e^{-\beta E_4}+e^{-\beta E_5}+e^{-\beta E_{12}}+e^{-\beta E_{13}}+e^{-\beta E_{14}}+e^{-\beta E_{15}})\times\\
&(e^{-\beta E_6}+e^{-\beta E_7}+e^{-\beta E_8}+e^{-\beta E_9}+e^{-\beta E_{10}}+e^{-\beta E_{11}})+4(e^{-\beta E_2}+e^{-\beta E_3}\\
&+e^{-\beta E_4}+e^{-\beta E_5})\times(e^{-\beta E_{12}}+e^{-\beta E_{13}}+e^{-\beta E_{14}}+e^{-\beta E_{15}})\big],
\end{aligned}
\tag{5.9}
$$

$$
\begin{aligned}
\chi(\wp) = -\frac{\partial^2 F}{\partial \wp^2} =&\\
&\frac{\sum\limits_{n,m=1}^{16}[\beta(\frac{dE_n}{d\wp})^2-\beta(\frac{dE_n}{d\wp})(\frac{dE_m}{d\wp})-\frac{d^2E_n}{d\wp^2}]\exp[-\beta(E_n+E_m)]}{(\sum\limits_{n=1}^{16}\exp[-\beta E_n])^2}\\
= \frac{\beta}{Z^2}\big[&(e^{-\beta E_2}+e^{-\beta E_{13}})\times(e^{-\beta E_1}+2e^{-\beta E_3}+e^{-\beta E_4}+e^{-\beta E_5}\\
&+(1+\frac{4\wp}{\sqrt{(5J)^2+8\wp^2}})e^{-\beta E_6}+(1-\frac{4\wp}{\sqrt{(5J)^2+8\wp^2}})e^{-\beta E_7}+e^{-\beta E_8}+e^{-\beta E_9}+
\end{aligned}
$$

$$
\begin{aligned}
&+e^{-\beta E_{10}}+e^{-\beta E_{11}}+2e^{-\beta E_{12}}+e^{-\beta E_{14}}+e^{-\beta E_{15}}+e^{-\beta E_{16}})\\
&+(e^{-\beta E_{3}}+e^{-\beta E_{12}})\times(e^{-\beta E_{1}}+2e^{-\beta E_{2}}+e^{-\beta E_{4}}+e^{-\beta E_{5}}\\
&+(1-\frac{4\wp}{\sqrt{(5J)^2+8\wp^2}})e^{-\beta E_{6}}+(1+\frac{4\wp}{\sqrt{(5J)^2+8\wp^2}})e^{-\beta E_{7}}+e^{-\beta E_{8}}+e^{-\beta E_{9}}\\
&+e^{-\beta E_{10}}+e^{-\beta E_{11}}+2e^{-\beta E_{13}}+e^{-\beta E_{14}}+e^{-\beta E_{15}}+e^{-\beta E_{16}})\\
&+(\frac{16\wp^2}{(5J)^2+8\wp^2}-\frac{4(5J)^2}{\beta((5J)^2+8\wp^2)^{\frac{3}{2}}})e^{-\beta E_{6}}(e^{-\beta E_{1}}+e^{-\beta E_{4}}+e^{-\beta E_{5}}+e^{-\beta E_{8}}+\\
&+e^{-\beta E_{9}}+e^{-\beta E_{10}}+e^{-\beta E_{11}}+e^{-\beta E_{14}}+e^{-\beta E_{15}}+e^{-\beta E_{16}})+(\frac{16\wp^2}{(5J)^2+8\wp^2}\\
&+\frac{4\wp}{\sqrt{(5J)^2+8\wp^2}}-\frac{4(5J)^2}{\beta((5J)^2+8\wp^2)^{\frac{3}{2}}})e^{-\beta E_{6}}(e^{-\beta E_{2}}+e^{-\beta E_{13}})\\
&+(\frac{16\wp^2}{(5J)^2+8\wp^2}-\frac{4\wp}{\sqrt{(5J)^2+8\wp^2}}-\frac{4(5J)^2}{\beta((5J)^2+8\wp^2)^{\frac{3}{2}}})e^{-\beta E_{6}}(e^{-\beta E_{3}}+e^{-\beta E_{12}})\\
&-\frac{4(5J)^2}{\beta((5J)^2+8\wp^2)^{\frac{3}{2}}}e^{-2\beta E_{6}}+(\frac{32\wp^2}{(5J)^2+8\wp^2}-\frac{4(5J)^2}{\beta((5J)^2+8\wp^2)^{\frac{3}{2}}})e^{-\beta E_{6}}e^{-\beta E_{7}}\\
&+(\frac{16\wp^2}{(5J)^2+8\wp^2}+\frac{4(5J)^2}{\beta((5J)^2+8\wp^2)^{\frac{3}{2}}})e^{-\beta E_{7}}(e^{-\beta E_{1}}+e^{-\beta E_{4}}+e^{-\beta E_{5}}+e^{-\beta E_{8}}\\
&+e^{-\beta E_{9}}+e^{-\beta E_{10}}+e^{-\beta E_{11}}+e^{-\beta E_{14}}+e^{-\beta E_{15}}+e^{-\beta E_{16}})\\
&+(\frac{16\wp^2}{(5J)^2+8\wp^2}-\frac{4\wp}{\sqrt{(5J)^2+8\wp^2}}+\frac{4(5J)^2}{\beta((5J)^2+8\wp^2)^{\frac{3}{2}}})e^{-\beta E_{7}}(e^{-\beta E_{2}}+e^{-\beta E_{13}})\\
&+(\frac{16\wp^2}{(5J)^2+8\wp^2}+\frac{4\wp}{\sqrt{(5J)^2+8\wp^2}}+\frac{4(5J)^2}{\beta((5J)^2+8\wp^2)^{\frac{3}{2}}})e^{-\beta E_{7}}(e^{-\beta E_{3}}+e^{-\beta E_{12}})\\
&+(\frac{32\wp^2}{(5J)^2+8\wp^2}+\frac{4(5J)^2}{\beta((5J)^2+8\wp^2)^{\frac{3}{2}}})e^{-\beta E_{7}}e^{-\beta E_{6}}+\\
&\frac{4(5J)^2}{\beta((5J)^2+8\wp^2)^{\frac{3}{2}}})e^{-2\beta E_{7}}].
\end{aligned}
\tag{5.10}
$$

In above expressions $-J_1 = J_2 = J$ was considered.

The dependence of the magnetic $\chi(B)$ and electric $\chi(\wp)$ susceptibilities on the temperature is shown in Fig. 5.10 and Fig. 5.11.

According to the definition Eq. (5.8) the maximum of the susceptibilities corresponds to the minimum of the fidelity related to the electric and magnetic fields. Comparing Fig. 5.10 and Fig. 5.11 with Fig. 5.5 we see a direct correlation between the threshold temperature of the pair entanglement τ_2 and the minimum of the fidelities related to the electric and magnetic fields. Namely, we see that the maximum of the magnetic and electric susceptibilities are observed to be in correlation with the corresponding threshold temperatures of the pair correlations. For larger threshold temperatures of the pair correlations, maxima of the magnetic and electric susceptibilities are shifted towards higher temperature. Interestingly in the case of the electric susceptibility,

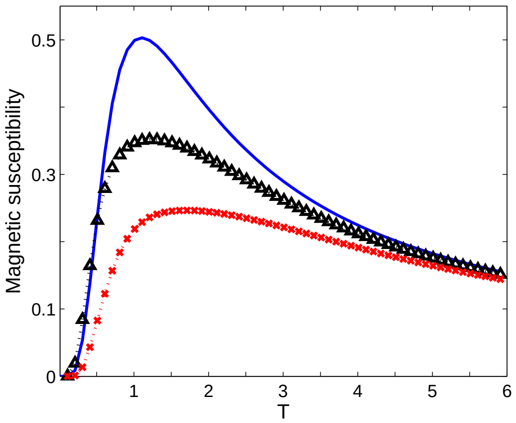

Figure 5.10. – Magnetic susceptibility as a function of the temperature for different values of the electric field $\wp = 0.5$(blue solid line), $\wp = 3$(black triangle line), $\wp = 5$(red cross line). The parameters are: $-J_1 = J_2 = 1, B = 0.25$.

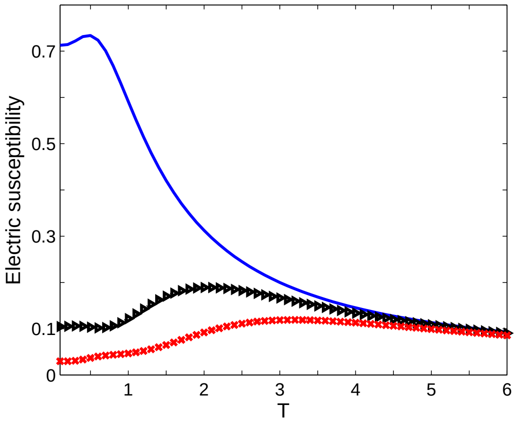

Figure 5.11. – Electric susceptibility as a function of the temperature for different values of the electric field $\wp = 0.5$(blue solid line), $\wp = 3$(black triangle line), $\wp = 5$(red cross line). The parameters are: $-J_1 = J_2 = 1, B = 0.25$.

correlation between threshold temperature of the pair entanglement τ_2 and the minimum of the fidelity is not only qualitative but quantitative as well. As we see the maximum of the electric susceptibility for large enough electric field is observed almost on the threshold temperatures $T_c = 2.1, \quad T_c = 3.1$ of the pair entanglement τ_2.

5.1.2. Efficiency of the Otto cycle

Here we study the dependence of the cycle efficiency on the modulation of the electric field amplitude. For this purpose we consider two different scenarios for adiabatic processes. One is quantum adiabatic in which level populations are fixed $P_n^A = P_n^D, \quad P_n^B = P_n^C$, and the heat absorbed by working substance and re-

leased read $Q_{\text{in}} = \sum_{n=1}^{16} E_n(\wp)\big(P_n^B - P_n^A\big)$ and $Q_{\text{out}} = \sum_{n=1}^{16} E_n(\wp_1)\big(P_n^B - P_n^A\big)$, where $P_n^B = Z^{-1}(T_H, \wp)\exp\big[-\frac{E_n(\wp)}{T_H}\big]$ and $P_n^A = Z^{-1}(T_L, \wp_1)\exp\big[-\frac{E_n(\wp_1)}{T_L}\big]$.

Then the expression for the cycle efficiency reads

$$\eta = \frac{Q_{\text{in}} - Q_{\text{out}}}{Q_{\text{in}}}. \tag{5.11}$$

In Fig. 5.12 the dependence of the efficiency on the modulation of the electric field $\wp$ is presented.

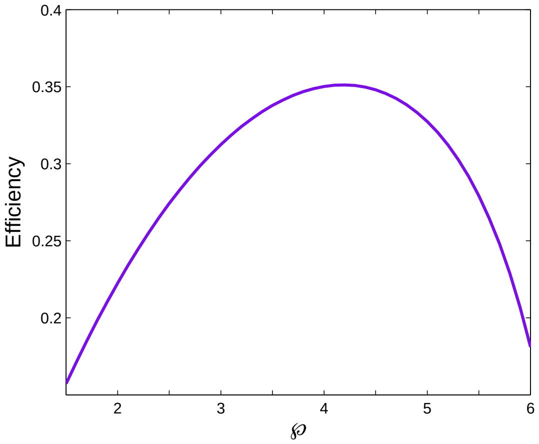

Figure 5.12. – The efficiency of the quantum adiabatic Otto cycle as a function of the modulation of the electric field amplitude for the following values of the parameters $-J_1 = J_2 = 1,\ B = 0.25,\ \wp_1 = 0.5,\ T_H = 10,\ T_L = 2.$

In another scenario quantum adiabatic strokes of the cycle are replaced by thermodynamic adiabatic strokes. The first law of thermodynamics is written as

$$dU\big(E_n, T\big) = \sum_n \Bigg(E_n dP_n + P_n dE_n + E_n \Big(\frac{\partial P_n}{\partial E_n}\Big)_{T=const} dE_n\Bigg), \tag{5.12}$$

where dU is the change of the total energy of the system $U\big(E_n, T\big) = \text{Tr}\big(\hat{\rho}\hat{H}\big) = \sum_{n=1}^{16} E_n P_n\big(E_n, T\big)$. The first term on the right hand side of Eq. 5.12 i.e. $\delta Q = E_n dP_n$, corresponds to the heat exchange and is related to the change of the level populations $P_n\big(E_n, T\big)$ occurred due to the change of the temperature for $E_n = const$, while second and third terms correspond to the produced work. If the adiabatic strokes of the cycle are quantum adiabatic then $\big(\frac{\partial P_n}{\partial E_n}\big)_{T=const} = 0$ and Eq. 5.12 reduces to the form given in Eq. 2.27.

The heat absorbed by the working substance Q_{in} and the heat released in the quantum isochoric cooling process Q_{out} in the case of the thermodynamic adiabatic cycle are defined in the following form

$$\begin{aligned} Q_{\text{in}} &= \sum_{n=1}^{16} E_n(\wp)\big(Z^{-1}(T_H,\wp)\exp\big[-\frac{E_n(\wp)}{T_H}\big] - Z^{-1}(T_L,\wp)\exp\big[-\frac{E_n(\wp)}{T_L}\big]\big), \\ Q_{\text{out}} &= \sum_{n=1}^{16} E_n(\wp_1)\big(Z^{-1}(T_H,\wp_1)\exp\big[-\frac{E_n(\wp_1)}{T_H}\big] - Z^{-1}(T_L,\wp_1)\exp\big[-\frac{E_n(\wp_1)}{T_L}\big]\big). \end{aligned} \tag{5.13}$$

Fig. 5.13 shows the dependence of the quantum Otto cycle efficiency on the modulation of the electric field amplitude $\wp$.

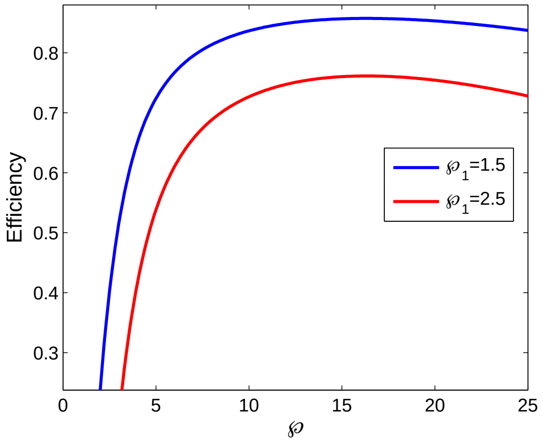

Figure 5.13. – The efficiency of the quantum Otto cycle as a function of the modulation of the electric field amplitude, for the following values of the parameters $-J_1 = J_2 = 1,\ B = 0.25,\ T_H = 10,\ T_L = 2$.

The saturation of the cycle efficiency with further increasing of the electric field amplitude is also observed. From the figures Fig. 5.12 and Fig. 5.13 one can see in both cases the maximal efficiency is reached for certain optimal values of the modulation of the electric field amplitude. However, the maximal efficiency obtained for the thermodynamic adiabatic cycle is higher compared to the efficiency corresponding to the quantum adiabatic case. A reasonably high efficiency around 86 percent can be reached already for $\wp/\wp_1 \approx 10$. So depending on the values of electric field, the efficiency can be larger or smaller than the Carnot cycle efficiency $\eta_C = 1 - T_L/T_H$. The reason for exceeding the Carnot cycle efficiency is of entirely quantum origin, which can be related to the entanglement of the working substance. To illustrate this the efficiency of the cycle as a function of the pair correlations is plotted in Fig. 5.14 which proves that the increase of the entanglement in the system results in enhanced cycle efficiency.

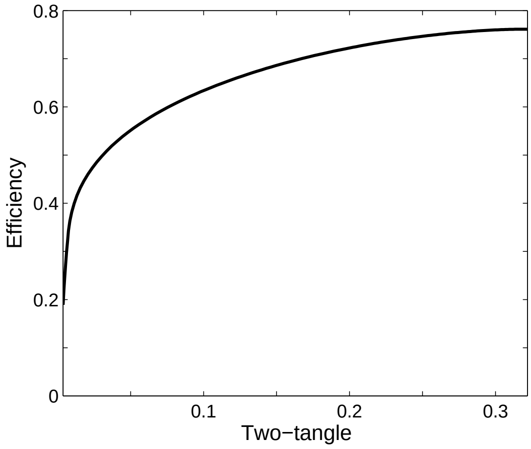

Figure 5.14. – The efficiency of the quantum Otto cycle as a function of the pair entanglement for the following values of the parameters $-J_1 = J_2 = 1,\ B = 0.25,\ \wp_1 = 2.5$.

5.1.3. Semi-classical limit

In this subsection by using the canonical thermodynamic perturbation theory [121] the semi-classical limit is investigated. Assuming $\wp$ as a small parameter we can consider the electric field part of the total Hamiltonian as a perturbed term

$$\begin{aligned}
&\hat{H} = \hat{\mathcal{H}}_0 + \hat{V}, \\
&\hat{\mathcal{H}}_0 = -\sum_{i=1}^{N} \vec{S}_i.\vec{S}_{i+1} + \sum_{i=1}^{N} \vec{S}_i.\vec{S}_{i+2} - B\sum_{i=1}^{N} S_i^z, \\
&\hat{V} = \wp \sum_i (\vec{S}_i \times \vec{S}_{i+1})^z, \qquad (5.14)
\end{aligned}$$

where $-J_1 = J_2 = J$, $B \to \gamma_e \hbar B/J$, $\wp \to g_{ME}|\vec{\wp}|/J)$ are concerned. The eigenvalues E_n^0 and eigenfunctions $|\Phi_n\rangle$ of the Hamiltonian $\hat{\mathcal{H}}_0$ are

$$\begin{aligned}
&|\Phi_1\rangle = |\uparrow\uparrow\uparrow\uparrow\rangle,\ |\Phi_2\rangle = \frac{1}{\sqrt{2}}(-|\uparrow\downarrow\uparrow\uparrow\rangle + |\uparrow\uparrow\uparrow\downarrow\rangle),\ |\Phi_3\rangle = \frac{1}{\sqrt{2}}(-|\downarrow\uparrow\uparrow\uparrow\rangle + |\uparrow\uparrow\downarrow\uparrow\rangle), \\
&|\Phi_4\rangle = \frac{1}{2}(|\downarrow\uparrow\uparrow\uparrow\rangle - |\uparrow\downarrow\uparrow\uparrow\rangle + |\uparrow\uparrow\downarrow\uparrow\rangle - |\uparrow\uparrow\uparrow\downarrow\rangle), \\
&|\Phi_5\rangle = \frac{1}{2}(|\downarrow\uparrow\uparrow\uparrow\rangle + |\uparrow\downarrow\uparrow\uparrow\rangle + |\uparrow\uparrow\downarrow\uparrow\rangle + |\uparrow\uparrow\uparrow\downarrow\rangle), \\
&|\Phi_6\rangle = \frac{1}{\sqrt{2}}(-|\downarrow\uparrow\downarrow\uparrow\rangle + |\uparrow\downarrow\uparrow\downarrow\rangle),\ |\Phi_7\rangle = \frac{1}{2}(|\downarrow\downarrow\uparrow\uparrow\rangle - |\downarrow\uparrow\uparrow\downarrow\rangle - |\uparrow\downarrow\downarrow\uparrow\rangle + |\uparrow\uparrow\downarrow\downarrow\rangle), \\
&|\Phi_8\rangle = \frac{1}{\sqrt{6}}\big(|\downarrow\downarrow\uparrow\uparrow\rangle + |\downarrow\uparrow\downarrow\uparrow\rangle + |\downarrow\uparrow\uparrow\downarrow\rangle + |\uparrow\downarrow\downarrow\uparrow\rangle + |\uparrow\downarrow\uparrow\downarrow\rangle + |\uparrow\uparrow\downarrow\downarrow\rangle\big), \\
&|\Phi_9\rangle = \frac{1}{\sqrt{12}}\big(|\downarrow\downarrow\uparrow\uparrow\rangle - 2|\downarrow\uparrow\downarrow\uparrow\rangle + |\downarrow\uparrow\uparrow\downarrow\rangle + |\uparrow\downarrow\downarrow\uparrow\rangle - 2|\uparrow\downarrow\uparrow\downarrow\rangle + |\uparrow\uparrow\downarrow\downarrow\rangle\big),
\end{aligned}$$

$$\begin{aligned}
&|\Phi_{10}\rangle = \frac{1}{\sqrt{2}}(|\downarrow\downarrow\uparrow\uparrow\rangle - |\uparrow\uparrow\downarrow\downarrow\rangle),\ |\Phi_{11}\rangle = \frac{1}{\sqrt{2}}(|\downarrow\uparrow\uparrow\downarrow\rangle - |\uparrow\downarrow\downarrow\uparrow\rangle),\\
&|\Phi_{12}\rangle = \frac{1}{\sqrt{2}}(-|\downarrow\downarrow\downarrow\uparrow\rangle + |\downarrow\uparrow\downarrow\downarrow\rangle),\ |\Phi_{13}\rangle = \frac{1}{\sqrt{2}}(-|\downarrow\downarrow\uparrow\downarrow\rangle + |\uparrow\downarrow\downarrow\downarrow\rangle),\\
&|\Phi_{14}\rangle = \frac{1}{2}(|\downarrow\downarrow\downarrow\uparrow\rangle + |\downarrow\downarrow\uparrow\downarrow\rangle + |\downarrow\uparrow\downarrow\downarrow\rangle + |\uparrow\downarrow\downarrow\downarrow\rangle),\\
&|\Phi_{15}\rangle = \frac{1}{2}(-|\downarrow\downarrow\downarrow\uparrow\rangle + |\downarrow\downarrow\uparrow\downarrow\rangle - |\downarrow\uparrow\downarrow\downarrow\rangle + |\uparrow\downarrow\downarrow\downarrow\rangle,\ |\Phi_{16}\rangle = |\downarrow\downarrow\downarrow\downarrow\rangle, \qquad (5.15)\\
&E_1^0 = -2B,\quad E_2^0 = J - B,\quad E_3^0 = J - B,\\
&E_4^0 = -2J - B,\quad E_5^0 = -B,\quad E_6^0 = -2J,\\
&E_7^0 = 3J,\quad E_8^0 = 0,\quad E_9^0 = -3J,\quad E_{10}^0 = J,\\
&E_{11}^0 = J,\quad E_{12}^0 = J + B,\quad E_{13}^0 = J + B,\\
&E_{14}^0 = B,\quad E_{15}^0 = -2J + B,\quad E_{16}^0 = 2B.
\end{aligned}$$

Taking the derivative of the normalization condition $\sum_n \exp\big[\frac{F - E_n}{T}\big] = 1$ where $F = -T\ln\big(\sum_n \exp\big[-\frac{E_n}{T}\big]\big)$ is the free energy of the system we obtain

$$\begin{aligned}
\Delta F &= \big(\frac{\partial F}{\partial T}\big)_{\wp}\delta T + \langle\frac{\partial \hat{H}}{\partial \wp}\rangle\delta\wp,\\
S &= -\big(\frac{\partial F}{\partial T}\big)_{\wp}.
\end{aligned} \tag{5.16}$$

The entropy of the system is defined by the partial derivative of the free energy with respect to the temperature at constant values of the electric field. This means that the dependence of the entropy on the electric field is parametric. If the temperature is constant the entropy is also constant.

Utilizing canonical thermodynamic perturbation theory in the semi-classical high temperature limit $E_n^0 - E_m^0 < T$ results

$$F(T,\wp) = F_0(T,0) + \big\langle V(\wp)\big\rangle - \frac{1}{2T}\{\sum_{m\neq n}\big\langle|V_{nm}(\wp)|^2\big\rangle + \big\langle(V(\wp) - \big\langle V(\wp)\big\rangle)^2\big\rangle\}, \tag{5.17}$$

where $\big\langle V_{nn}(\wp)\big\rangle = \sum_n P_n V_{nn}(\wp)$ is the mean value of the matrix element of the perturbation $\hat{V}$ evaluated in the basis of the unperturbed Hamiltonian $\hat{\mathcal{H}}_0$ and $\big\langle|V_{nm}(\wp)|^2\big\rangle = \sum_n P_n|V_{nm}(\wp)|^2$, $\big\langle(V(\wp) - \big\langle V(\wp)\big\rangle)^2\big\rangle = \sum_n P_n\big(V_{nn} - \sum_k P_k V_{kk}\big)^2$. Level populations are described in terms of the Gibbs distribution function P_n. After some straightforward calculations based on the Eq. 5.17 we obtain

$$F(T,\wp) = -T\ln(\sum_{n=1}^{16} e^{-\frac{E_n^0}{T}}) - \frac{\wp^2(e^{-\frac{E_2^0}{T}} + e^{-\frac{E_{12}^0}{T}} + e^{-\frac{E_6^0}{T}} + e^{-\frac{E_7^0}{T}})}{T\sum_{n=1}^{16} e^{-\frac{E_n^0}{T}}}. \tag{5.18}$$

And for the entropy of the system we get

$$\begin{aligned} S(T,\wp) = \ln\big(\sum_{n=1}^{16} e^{-\frac{E_n^0}{T}}\big) + \frac{\sum_{n=1}^{16} E_n^0 e^{-\frac{E_n^0}{T}}}{T\sum_{n=1}^{16} e^{-\frac{E_n^0}{T}}} - \wp^2\Bigg(\frac{e^{-\frac{E_2^0}{T}} + e^{-\frac{E_{12}^0}{T}} + e^{-\frac{E_6^0}{T}} + e^{-\frac{E_7^0}{T}}}{T^2\sum_{n=1}^{16} e^{-\frac{E_n^0}{T}}} - \\ \frac{\big(E_2^0 e^{-\frac{E_2^0}{T}} + E_{12}^0 e^{-\frac{E_{12}^0}{T}} + E_6^0 e^{-\frac{E_6^0}{T}} + E_7^0 e^{-\frac{E_7^0}{T}}\big)\sum_{n=1}^{16} e^{-\frac{E_n^0}{T}}}{T^3(\sum_{n=1}^{16} e^{-\frac{E_n^0}{T}})^2} - \\ \frac{\big(e^{-\frac{E_2^0}{T}} + e^{-\frac{E_{12}^0}{T}} + e^{-\frac{E_6^0}{T}} + e^{-\frac{E_7^0}{T}}\big)\sum_{n=1}^{16} E_n^0 e^{-\frac{E_n^0}{T}}}{T^3(\sum_{n=1}^{16} e^{-\frac{E_n^0}{T}})^2}\Bigg). \end{aligned} \tag{5.19}$$

The entropy as a function of the temperature for different values of the parameters is plotted in Fig. 5.15

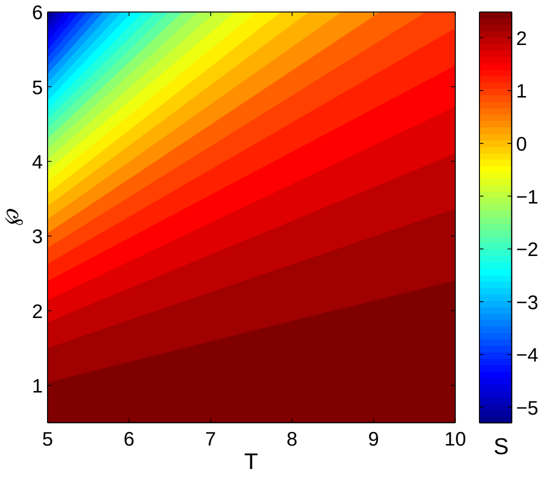

Figure 5.15. – Contour plot of entropy as a function of the modulation of the electric field amplitude and the temperature.

As is clear from Fig. 5.15 the maximum of the entropy is observed for small values of the electric field and in the high temperature limit. It's worthy to mention that Eq. 5.19 is obtained via a thermodynamic perturbation theory and negative values of the entropy correspond to the values of the parameters beyond the range where perturbation theory is viable.

Taking into account Eq. 5.19 the semi-classical efficiency in terms of the electric field can be expressed as

$$\eta_{sc} = 1 - \frac{\displaystyle\int_{T_L}^{T_H} T \frac{\partial S(T,\wp)}{\partial T} dT}{\displaystyle\int_{T_L}^{T_H} T \frac{\partial S(T,\wp_1)}{\partial T} dT}. \tag{5.20}$$

The semi-classical efficiency Eq. 5.20 as a function of the electric field $\wp$ and the temperature difference between the hot and cold baths $\Delta T = T_H - T_L$ for $T_L = 30$ are presented in Fig. 5.16.

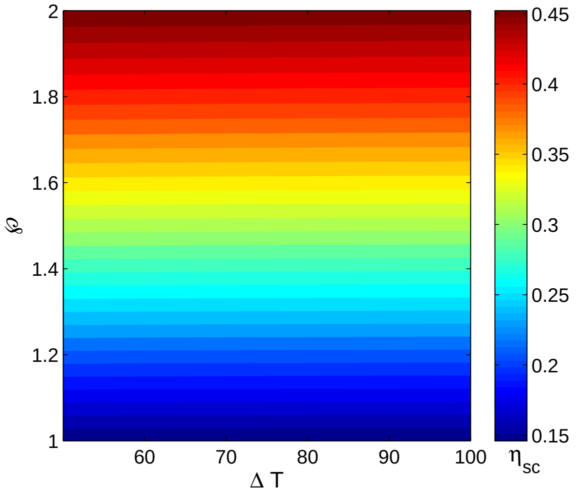

Figure 5.16. – The semi-classical efficiency η_{sc} as a function of the electric field $\wp$ and temperature difference between hot and cold baths $\Delta T = T_H - T_L$ for $T_L = 30$, $\wp_1 = 0.5$.

As we see semi-classical efficiency is more sensitive to the values of the electric field, rather than the temperature difference ΔT.

5.2. Quantum size effects

In this section we consider the role of the system size. First for the spin chain of $N = 8$, the ratio between two- and one-tangle is investigated. See Fig. 5.17.

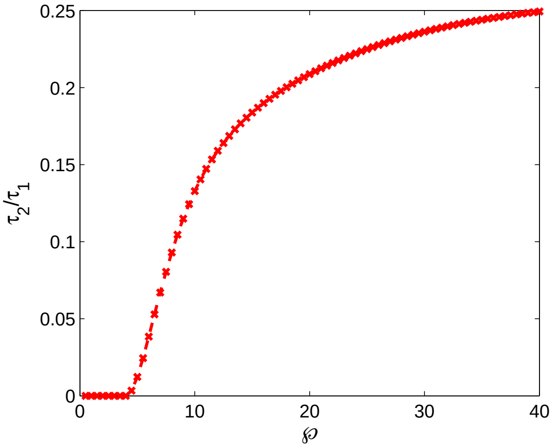

Figure 5.17. – Ratio between two- and one-tangle as a function of the external electric field for the system of 8 spins and the following values of the parameters $-J_1 = J_2 = 1, B = 0.25, T = 1.9$.

Comparing Fig. 5.17 with Fig. 5.8 shows that with increasing the size of the working substance, the ratio between two- and one-tangle τ_2/τ_1 becomes smaller indicating that the many-body entanglement τ_1 is increasing with the size of the system N faster than the pair correlations τ_2.

The magnetic and electric susceptibilities are also presented in Fig. 5.18 and Fig. 5.19.

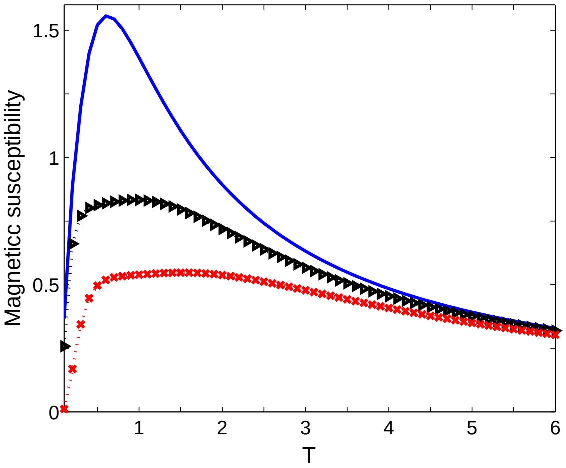

Figure 5.18. – Magnetic susceptibility as a function of the temperature for the system of 8 spins and different values of the electric field $\wp = 0.5$(blue solid line), $\wp = 3$(black triangle line), $\wp = 5$(red cross line). The parameters are: $-J_1 = J_2 = 1, B = 0.25$.

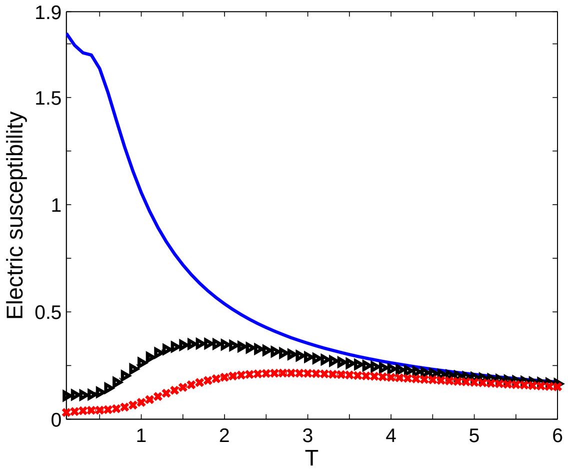

Figure 5.19. – Electric susceptibility as a function of the temperature for the system of 8 spins and different values of the electric field $\wp = 0.5$(blue solid line), $\wp = 3$(black triangle line), $\wp = 5$(red cross line). The parameters are: $-J_1 = J_2 = 1, B = 0.25$.

Comparing these two figures with Fig. 5.10 and Fig. 5.11 it is clear that the heights of the peaks of the electric and magnetic susceptibilities increase with the system size and shift towards lower temperature regime for $N = 8$ case with compared to $N = 4$ case. A similar peak in the magnetic susceptibility at finite temperatures was also observed in [122] for zero fields and $N = 24$ which interpreted as resulting of a competition between antiferromagnetic and ferromagnetic correlations in the system.

Finally we investigate the scaling of the Otto cycle efficiency with the size of the working substance for different values of the electric field. See Fig. 5.20.

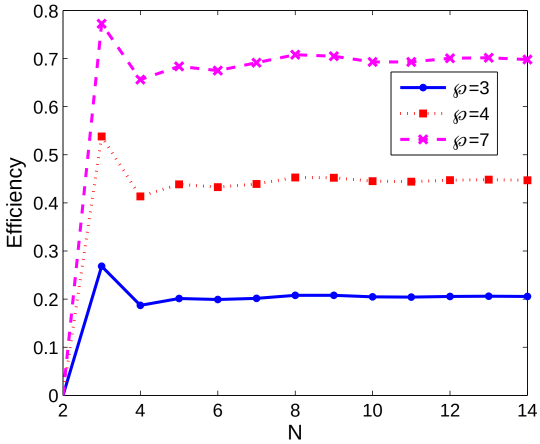

Figure 5.20. – The efficiency of the quantum Otto cycle as a function of the system size N for three different values of the electric field. The other parameters are $-J_1 = J_2 = 1,\ B = 0.25,\ T_H = 10,\ T_L = 2$.

A different behavior is found for a smaller size of the working substance in comparison to a large system size case. We find a sudden increase in the efficiency for $N = 3$. For $N > 4$, no significant variation in the efficiency is observed when increasing the system size N. Therefore we see the saturation of the efficiency.

5.3. Summary

The quantum Otto heat engine operating with the working substance of one-dimensional frustrated ferromagnetic spin-1/2 chain has been studied. The presence of the finite spin chirality in the working substance allows to drive a cycle by the external electric field. A direct connection between chirality, entanglement and the efficiency of the engine is observed. We found the electric field dependent threshold temperature above which the pair correlations in the system as quantified by thermal entanglement decay. These threshold temperatures scale with the electric field and become higher if the amplitude of the electric field is increased. Opposite to the pair correlations the collective many body thermal entanglement which can be generated by arbitrary small electric field, is extremely robust to the field and survives even in the high temperature limit. We also identified a direct correlation between threshold temperature of pair entanglement, with the spin chirality and the minimum of the fidelities related to the electric and magnetic fields. The efficiency of the studying quantum Otto cycle shows a saturation plateau with increasing the electric field amplitude.

6. Superadiabatic quantum Otto heat engine

In this chapter, we present the recent technique [123–125] named as shortcuts to quantum adiabaticity, to obtain a finite output power of the quantum Otto heat engine. In general this technique quenches the effect of inter-level transitions which are of purely quantum origin. Such transitions naturally accompany the fast driving process. Nevertheless shortcut to quantum adiabaticity eliminates the effect of those inter-level transitions. After using shortcuts to quantum adiabaticity, a quantum heat engine with non-zero output power is realized.

6.1. Introducing the technique

Here we will follow Berry's transitionless driving [125] which is equivalent to the counterdiabatic formulation of Demirplak and Rice [123, 124]. Consider an arbitrary time dependent Hamiltonian $\hat{H}(t)$. In the adiabatic approximation a general state $|\Psi_n(t)\rangle$ driven by $\hat{H}(t)$ is

$$|\Psi_n(t)\rangle = \exp\left[-\frac{i}{\hbar}\int_0^t dt' E_n(t') - \int_0^t dt' \langle\Phi_n(t')|\partial_{t'}\Phi_n(t')\rangle\right]|\Phi_n(t)\rangle. \quad (6.1)$$

Here $|\Phi_n(t)\rangle$ and $E_n(t)$ are the instantaneous states and energies of the Hamiltonian $\hat{H}(t)$. The idea of the reverse engineering approach is to look for an auxiliary (counterdiabatic) Hamiltonian $\hat{H}_{CD}(t)$ for which the above states are the exact evolving states i.e.

$$i\hbar\partial_t|\Psi_n(t)\rangle = \hat{H}_{CD}(t)|\Psi_n(t)\rangle. \quad (6.2)$$

We know that any time-dependent unitary operator $\hat{U}(t)$ is the solution of the equation

$$i\hbar\partial_t\hat{U}(t) = \hat{H}_{CD}(t)\hat{U}(t). \quad (6.3)$$

Therefore

$$\hat{H}_{CD}(t) = i\hbar\big(\partial_t\hat{U}(t)\big)\hat{U}^\dagger(t). \quad (6.4)$$

With the aid of the unitary time-evolution operator

$$\hat{U}(t) = \sum_n \exp\Big[-\frac{i}{\hbar}\int_0^t dt' E(t') \\ - \int_0^t dt' \langle \Phi_n(t')|\partial_{t'}\Phi_n(t')\rangle \Big] |\Phi_n(t)\rangle\langle\Phi_n(0)|, \tag{6.5}$$

the auxiliary counter-diabatic (CD) Hamiltonian $\hat{H}_{CD}(t)$ in Eq. (6.4) is obtained

$$\hat{H}_{CD}(t) = \hat{H}(t) + \hat{H}_1(t), \tag{6.6}$$

where

$$\hat{H}_1(t) = i\hbar \sum_{m\neq n} \frac{|\Phi_m\rangle\langle\Phi_m|\partial_t \hat{H}(t)|\Phi_n\rangle\langle\Phi_n|}{E_n - E_m}. \tag{6.7}$$

In this way, even for a fast driving, transitions between the eigenstates $|\Phi_n(t)\rangle$ are prevented. Adopting initial conditions $\hat{H}_{CD}(0) = \hat{H}(0)$, $\hat{H}_{CD}(\tau) = \hat{H}(\tau)$, yields fast adiabatic dynamics in the time interval $t \in [0, \tau]$.

6.2. Driving the cycle

In order to drive the cycle, we consider time dependent electric field in Eq. (3.1) and choose a particular type of it as

$$\wp(t) = \epsilon\left(\frac{t^3}{3\tau} - \frac{t^2}{2}\right) + \wp_0. \tag{6.8}$$

As it is described in Chapter 5 the cycle consists of two quantum isochoric and two adiabatic strokes. The quantum isochoric strokes correspond to heat exchange between the working substance and the cold and the hot heat baths. During these strokes the level populations are altered. Changing the amplitude of the applied external electric field modifies the energy spectrum of the system and the working substance produces work. The working parameter $\wp(t)$ during the adiabatic strokes varies from $\wp_0 \longrightarrow \wp_1$ (stroke $B \to C$) and $\wp_1 \longrightarrow \wp_0$ (stroke $D \to A$). See Fig. 5.1. It is evident that in this case the requirement for the shortcuts to adiabaticity i.e.

$$\hat{H}_{CD}(0) = \hat{H}(0),\ \hat{H}_{CD}(\tau) = \hat{H}(\tau),$$

is fulfilled. Therefore, we can drive the cycle quite fast. Using Eq. (6.7) we obtain

$$\hat{H}_1(t) = i\hbar A(t)\big(|\Phi_6(t)\rangle\langle\Phi_7(t)| - |\Phi_7(t)\rangle\langle\Phi_6(t)|\big), \tag{6.9}$$

where $A(t) = \frac{4\dot{\wp}(t)(\lambda+\mu)\alpha\gamma}{\wp(t)(\lambda-\mu)}$. In fact the time dependence in the model appears through the external electric field $\wp(t)$ and its time derivative $\dot{\wp}(t)$. The explicit form of the eigenfunctions and eigenvalues of the Hamiltonian H_{CD} are presented in the appendix. In the following we mostly focus on the output power of the cycle and the irreversible work.

6.3. The output power and irreversible work

For a finite time thermodynamic process, the output power of the quantum Otto cycle can be written as [126–129]

$$\Re = \frac{-\big(\langle W_2\rangle_{\rm ad} + \langle W_4\rangle_{\rm ad}\big)}{\tau_1(T_H) + \tau_2 + \tau_3(T_L) + \tau_4}. \tag{6.10}$$

$\tau_1(T_H)$, $\tau_3(T_L)$ are the relaxation times of the working substance in contact with the hot and the cold thermal baths, τ_2 and τ_4 correspond to the duration of the adiabatic strokes as well $\langle W_2\rangle_{\rm ad}$ and $\langle W_4\rangle_{\rm ad}$ correspond to the work produced during the quantum adiabatic strokes. The expression for the total quantum mean work reads [130, 131]

$$\langle W\rangle = \sum_{n,m} \big(E_n(t) - E_m(0)\big) P_{mn}(t) P_m^{(0)}(\beta), \tag{6.11}$$

where

$$P_{mn}(t) = |\langle\Phi_n(t)|\hat{U}(t)|\Phi_m(0)\rangle|^2,$$

is the transition probability between the eigenstates of the Hamiltonian $\hat{H}(t)$, and $P_m^{(0)}(\beta)$ describes the level populations in the equilibrium at the temperature β. After the counter-diabatic driving the cycle is reversible and at the end of the stroke the transition probability simplifies to $P_{mn}(\tau) = \delta_{mn}$. Therefore, the expressions of the adiabatic work for the cycle strokes are

$$\begin{aligned} \langle W_2\rangle_{\rm ad} &= \sum_n \big[E_n(\tau) - E_n(0)\big] P_n^{(1)}(\beta_H), \\ \langle W_4\rangle_{\rm ad} &= \sum_n \big[E_n(0) - E_n(\tau)\big] P_n^{(3)}(\beta_L). \end{aligned} \tag{6.12}$$

Here $P_n^{(1)}(\beta_H) = \frac{e^{-\beta_H E_n(0)}}{\sum_n e^{-\beta_H E_n(0)}}$, $P_n^{(3)}(\beta_L) = \frac{e^{-\beta_L E_n(\tau)}}{\sum_n e^{-\beta_L E_n(\tau)}}$ are the level populations in equilibrium at the temperatures $\beta_H = 1/T_H$, $\beta_L = 1/T_L$ respectively. To quantify the mean square fluctuations $\Delta W_{\rm ad} = \big[\langle W^2\rangle_{\rm ad} - \langle W\rangle_{\rm ad}^2\big]^{\frac{1}{2}}$ for the work $W = W_2 + W_4$, we utilize the following ansatz

$$\begin{aligned} \langle W^2\rangle_{\rm ad} &= \langle W_2^2\rangle_{\rm ad} + \langle W_4^2\rangle_{\rm ad} + 2\langle W_2\rangle_{\rm ad}\langle W_4\rangle_{\rm ad}, \\ \langle W\rangle_{\rm ad}^2 &= \langle W_2\rangle_{\rm ad}^2 + \langle W_4\rangle_{\rm ad}^2 + 2\langle W_2\rangle_{\rm ad}\langle W_4\rangle_{\rm ad}. \end{aligned} \tag{6.13}$$

The mean values of the work are defined as

$$\begin{aligned}\langle W^2_{2,(4)}\rangle_{\rm ad} &= \sum_n \big[E_n(\tau) - E_n(0)\big]^2 P_n^{(1),(3)}(\beta_H,\beta_L),\\ \langle W_{2,(4)}\rangle^2_{\rm ad} &= \left(\sum_n \big[E_n(0) - E_n(\tau)\big] P_n^{(1),(3)}(\beta_H,\beta_L)\right)^2.\end{aligned} \tag{6.14}$$

In Fig. 6.1 the work mean square fluctuations and the output power are plotted. As is clear from the figure the work mean square fluctuations increase with the stroke duration τ. The modulation depth of the driving parameter $\wp(t,\tau) = \epsilon\big(t^3/3\tau - t^2/2\big) + d_0,\ \dot{\wp}(0,\tau) = \dot{\wp}(\tau,\tau)$ enhances the work mean square fluctuations for longer duration of the adiabatic strokes τ.Enhancement of the cycle duration has an adverse effect on the output power. These two factors compete resulting in the optimal time length of the adiabatic strokes $\tau_{op} = 0.35$[ps]. We also observe that a strong magnetic field is counterproductive for the output power.

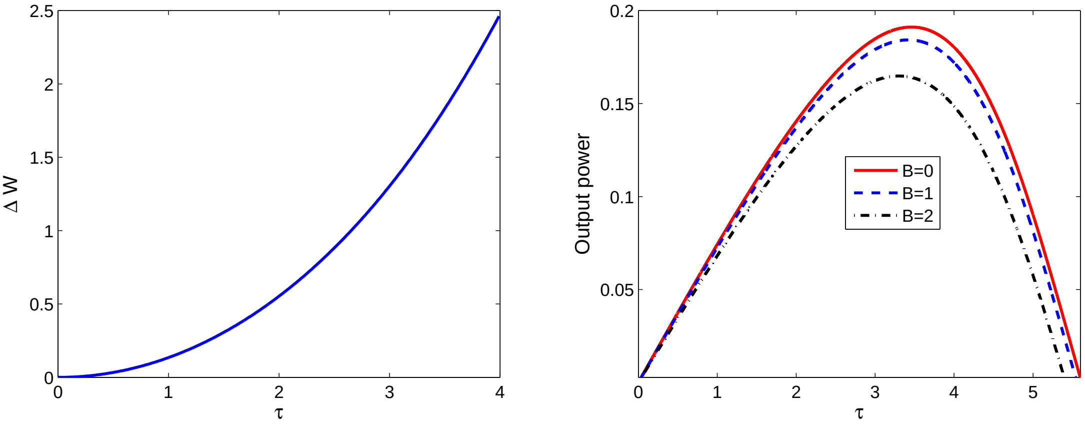

Figure 6.1. – Left panel: The work mean square fluctuations for $B = 0.25$. Right panel: The output power for different magnetic fields. The other considered parameters are $J_1 = -1, J_2 = 1, \wp_0 = 5, \epsilon = 1, T_H = 15, T_L = 2$.

Irreversibility of classical thermodynamical processes are quantified in terms of Clausius inequality

$$\Delta S = S_{\rm re} + S_{\rm irr}, \tag{6.15}$$

where $S_{\rm re} = \beta Q$, is the equilibrium entropy, Q is the transferred heat and $\beta = 1/T$ is the inverse temperature. For irreversible processes $S_{\rm irr} > 0$. In quantum thermodynamics the situation is more delicate. E.g., the concept of work for mesoscopic systems has been revisited recently [132, 133]. The work performed on a finite quantum system is not an observable but a randomly distributed quantity [131, 134]. Any sudden abrupt change, fast driving or a quench, drags the system into a non-equilibrium state. Hence, recipes of the equilibrium thermodynamics need to be re-inspected. A fast transformation leads to the "parasitic" irreversible work $\Delta S_{\text{irr}} = \beta\big\langle W_{\text{irr}}\big\rangle$ which amounts to the difference between the total work and the change of the free energy $\big\langle W_{\text{irr}}\big\rangle = \big\langle W\big\rangle - \Delta F$. We use the quantum Kullback-Leibler divergence

$$S\big(\varrho_A \parallel \varrho_B\big) = Tr\big(\varrho_A \ln \varrho_A - \varrho_A \ln \varrho_B\big),$$

and rewrite the expression for the irreversible work in the following form [131]

$$\big\langle W_{\text{irr}}\big\rangle = \big\langle W\big\rangle - \Delta F = \frac{1}{\beta} S\big(\rho_t \| \rho_t^{\text{eq}}\big). \tag{6.16}$$

Here

$$\begin{aligned} S\big(\rho_t \| \rho_t^{\text{eq}}\big) &= -\sum_{n,k} P_n^0 P_{kn}^t \ln P_k^t + \sum_n P_n^0 \ln P_n^0, \\ \Delta F &= -\frac{1}{\beta} \ln\left(\frac{\sum_n \exp\big[-\beta E_n(t)\big]}{\sum_m \exp\big[-\beta E_m(0)\big]}\right). \end{aligned} \tag{6.17}$$

$P_n^0 = \exp[-\beta E_n]/\sum_n \exp[-\beta E_n]$, $P_k^t = \exp[-\beta E_k^{CD}]/\sum_k \exp[-\beta E_k^{CD}]$ correspond to the level populations and $P_{kn}^t = |\langle \Psi_n(t)|\hat{U}(t)|\Phi_k(0)\rangle|^2$ corresponds to the transition amplitudes.

In Fig. 6.2 we see a non-monotonic behavior of the irreversible work. For larger times the system tends to equilibrium.

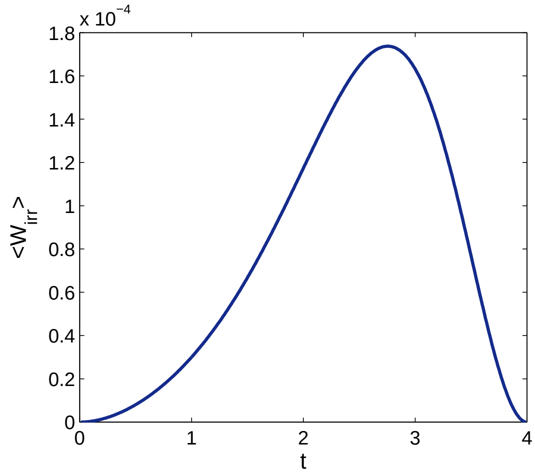

Figure 6.2. – $\big\langle W_{\text{irr}}\big\rangle$ for the values of parameters $J_1 = -1, J_2 = 1, B = 0.25, \wp_0 = 5, \epsilon = 1, \tau = 4, T_H = 15, T_L = 2$.

6.4. Summary

Shortcuts to adiabaticity are employed to achieve an efficient, finite time quantum thermodynamic cycle. We determined the work mean square fluctuations, the irreversible work, and the output power of the cycle. We observed that the work mean square fluctuations are increased with the duration of the adiabatic strokes while the irreversible work and the output power of the cycle show a non-monotonic behavior. In particular the irreversible work vanishes at the end of the quantum adiabatic strokes and confirms that the cycle is reversible.

7. Conclusion and Outlook

The present thesis has focused on a theoretical investigation of spin-spiral multiferroics. Such multiferroic systems are under intensive study both experimentally and theoretically. In particular, we analyzed the one-dimensional frustrated ferromagnetic spin-1/2 chain in which the appearance of the chirality enables us to drive the system by external electric field. Let us summarize the main results obtained in this work.

- In chapter three we saw that the electric field leads to the formation of the chiral spin structure in the multiferroic spin chain and simultaneously generates entanglement characterized by many spin correlations rather than local two spin concurrence. In the case of nonzero expectation values of the chirality we evaluated the fidelity susceptibility and proved that the system is sensitive to tiny changes of the amplitude of the electric field while a slight change of the magnetic field has no significant impact on the system. In addition, we have shown that quantum state transfer fidelity also can be controlled via the applied external electric field. By proper tuning of the external electric driving field one can transmit quantum state through the multiferroic spin chain with higher fidelity. These findings endorse the suitability of electric field controlled quantum information processing in spin-spiral multiferroics.

- We studied the influence of short electric field pulses on a multiferroic spin chain in chapter four. Chirality as a function of time was calculated analytically for four spins case and numerically for higher spins. For the one-excitation initial state chirality is independent of time, but for the higher n-excitations initial state the chirality oscillates with the time. A qualitative measure of one-tangle, two-tangle and von Neumann entropy have also been calculated analytically for four spins case and numerically for the higher spins case. For a given excitation number basis the two-tangle decays with increasing the number of spins in the chain, however multi-party entanglement sharing is significant. We also noticed a signature of dynamical phase transitions from commensurate to incommensurate chiral phase in the system.

- In chapter five we considered a quantum Otto heat engine operating with the working substance of multiferroic spin chain. It has been shown that due to the existence of nonzero spin chirality in the working substance which is coupled to the induced electric polarization, the efficiency of the cycle is sensitive to the applied external electric field. We analyzed the dependence of the cycle efficiency on the system size. Particularly the efficiency reaches extremely high values (slightly below 80%) for small working substance consisting of $N = 3$ spins. Increasing size of the working substance yields a saturation plateau of the efficiency of the quantum Otto cycle. We also observed a robustness of the many body collective entanglement versus the temperature. Many body entanglement is quantified in terms of the one-tangle τ_1 and is always larger than the total pair concurrence quantified by the two-tangle τ_2 indicating that a major amount of the entanglement of multiferroic working substance is stored in long range multi-spin correlations. In contrast to the one-tangle, the pair correlation is sensitive to the increase of the temperature. In particular, we identified the existence of the threshold temperature for the two-tangle τ_2. The stronger electric field amplitude, the threshold temperature is higher. The same behavior is observed for the chirality as well. Outstandingly with the increase of the temperature, the thermal chirality undergoes dramatic changes and for the threshold temperature T_C of the two-tangle τ_2, thermal chirality, reaches its minima. Thus can be concluded that the thermal chirality, is related to the pair correlations in the system rather than to the nonlocal entanglement. The dependence of the magnetic and electric susceptibilities on the temperature is also studied. Maximum of the susceptibilities corresponds to the minimum of the fidelity related to the electric and magnetic fields. We saw a direct correlation between the threshold temperature of the pair entanglement τ_2 and the minimum of the fidelities related to the electric and magnetic fields. The maximum of the electric and magnetic susceptibilities are observed to be in correlation with the corresponding threshold temperatures of the pair correlations. For larger threshold temperatures of the pair correlations maximum of the electric and magnetic susceptibilities are shifted towards higher temperature. Interestingly, in the case of the electric susceptibility, correlation between the threshold temperature of pair entanglement τ_2 and the minimum of the fidelity is not only qualitative but quantitative as well. The maximum of the electric susceptibility is observed almost on the threshold temperatures $T_c = 2.1$, $T_c = 3.1$ of the pair entanglement τ_2.

- We implemented shortcuts to adiabaticity in chapter 6 and realized transitionless fast quantum adiabatic dynamics in order to construct a finite time quantum heat engine with a reasonable output power. We studied an exact solvable model and obtained analytical expressions for the counterdiabatic Hamiltonian. Using the analytical results the mean square fluctuation for the work, the irreversible work and output power of the cycle are evaluated. We observed that the work mean square fluctuations is increasing with the duration of the adiabatic strokes. While, the irreversible work shows non-monotonic behavior. At the end of adiabatic stroke the irreversible work becomes zero, confirming that the cycle is reversible. The output power of the cycle also shows a non-monotonic behavior. This theoretical finding evidences the existence of an inherent maximal output power.

A natural extension of this work would be to expand the quantum Otto heat engine to Diesel- or Stirling-type quantum heat engines and investigate the efficiency of the cycle as well as the output power.

A. Appendix

- Eigen functions of the Hamiltonian $\hat{H}_{CD}(t)$

$$
\begin{aligned}
&|\Psi_1\rangle = |\uparrow\uparrow\uparrow\uparrow\rangle,\\
&|\Psi_2\rangle = \frac{i}{2}|\downarrow\uparrow\uparrow\uparrow\rangle + \frac{-1}{2}|\uparrow\downarrow\uparrow\uparrow\rangle + \frac{-i}{2}|\uparrow\uparrow\downarrow\uparrow\rangle + \frac{1}{2}|\uparrow\uparrow\uparrow\downarrow\rangle,\\
&|\Psi_3\rangle = \frac{-i}{2}|\downarrow\uparrow\uparrow\uparrow\rangle + \frac{-1}{2}|\uparrow\downarrow\uparrow\uparrow\rangle + \frac{i}{2}|\uparrow\uparrow\downarrow\uparrow\rangle + \frac{1}{2}|\uparrow\uparrow\uparrow\downarrow\rangle,\\
&|\Psi_4\rangle = \frac{1}{2}|\downarrow\uparrow\uparrow\uparrow\rangle + \frac{-1}{2}|\uparrow\downarrow\uparrow\uparrow\rangle + \frac{1}{2}|\uparrow\uparrow\downarrow\uparrow\rangle + \frac{-1}{2}|\uparrow\uparrow\uparrow\downarrow\rangle,\\
&|\Psi_5\rangle = \frac{1}{2}|\downarrow\uparrow\uparrow\uparrow\rangle + \frac{1}{2}|\uparrow\downarrow\uparrow\uparrow\rangle + \frac{1}{2}|\uparrow\uparrow\downarrow\uparrow\rangle + \frac{1}{2}|\uparrow\uparrow\uparrow\downarrow\rangle,\\
&|\Psi_6\rangle =\\
&\frac{i\alpha C_1\big(-J_1-2J_2+\sqrt{4A^2+J_1^2+16J_2^2-8J_1J_2+8\wp^2}\big)}{2A}\big(|\downarrow\downarrow\uparrow\uparrow\rangle - i\mu|\downarrow\uparrow\downarrow\uparrow\rangle - |\downarrow\uparrow\uparrow\downarrow\rangle - |\uparrow\downarrow\downarrow\uparrow\rangle\\
&+ i\mu|\uparrow\downarrow\uparrow\downarrow\rangle + |\uparrow\uparrow\downarrow\downarrow\rangle\big) + C_1\gamma\big(|\downarrow\downarrow\uparrow\uparrow\rangle - i\lambda|\downarrow\uparrow\downarrow\uparrow\rangle - |\downarrow\uparrow\uparrow\downarrow\rangle - |\uparrow\downarrow\downarrow\uparrow\rangle + i\lambda|\uparrow\downarrow\uparrow\downarrow\rangle + |\uparrow\uparrow\downarrow\downarrow\rangle\big),\\
&|\Psi_7\rangle =\\
&\frac{i\alpha C_2\big(-J_1-2J_2-\sqrt{4A^2+J_1^2+16J_2^2-8J_1J_2+8\wp^2}\big)}{2A}\big(|\downarrow\downarrow\uparrow\uparrow\rangle - i\mu|\downarrow\uparrow\downarrow\uparrow\rangle - |\downarrow\uparrow\uparrow\downarrow\rangle - |\uparrow\downarrow\downarrow\uparrow\rangle\\
&+ i\mu|\uparrow\downarrow\uparrow\downarrow\rangle + |\uparrow\uparrow\downarrow\downarrow\rangle\big) + C_1\gamma\big(|\downarrow\downarrow\uparrow\uparrow\rangle - i\lambda|\downarrow\uparrow\downarrow\uparrow\rangle - |\downarrow\uparrow\uparrow\downarrow\rangle - |\uparrow\downarrow\downarrow\uparrow\rangle + i\lambda|\uparrow\downarrow\uparrow\downarrow\rangle + |\uparrow\uparrow\downarrow\downarrow\rangle\big),\\
&|\Psi_8\rangle = \frac{1}{\sqrt{6}}\big(|\downarrow\downarrow\uparrow\uparrow\rangle + |\downarrow\uparrow\downarrow\uparrow\rangle + |\downarrow\uparrow\uparrow\downarrow\rangle + |\uparrow\downarrow\downarrow\uparrow\rangle + |\uparrow\downarrow\uparrow\downarrow\rangle + |\uparrow\uparrow\downarrow\downarrow\rangle\big),\\
&|\Psi_9\rangle = \frac{1}{\sqrt{12}}\big(|\downarrow\downarrow\uparrow\uparrow\rangle - 2|\downarrow\uparrow\downarrow\uparrow\rangle + |\downarrow\uparrow\uparrow\downarrow\rangle + |\uparrow\downarrow\downarrow\uparrow\rangle - 2|\uparrow\downarrow\uparrow\downarrow\rangle + |\uparrow\uparrow\downarrow\downarrow\rangle\big),\\
&|\Psi_{10}\rangle = \frac{-1}{\sqrt{2}}|\downarrow\downarrow\uparrow\uparrow\rangle + \frac{1}{\sqrt{2}}|\uparrow\uparrow\downarrow\downarrow\rangle,\\
&|\Psi_{11}\rangle = \frac{-1}{\sqrt{2}}|\downarrow\uparrow\uparrow\downarrow\rangle + \frac{1}{\sqrt{2}}|\uparrow\downarrow\downarrow\uparrow\rangle,\\
&|\Psi_{12}\rangle = \frac{i}{2}|\downarrow\downarrow\downarrow\uparrow\rangle + \frac{-1}{2}|\downarrow\downarrow\uparrow\downarrow\rangle + \frac{-i}{2}|\downarrow\uparrow\downarrow\downarrow\rangle + \frac{1}{2}|\uparrow\downarrow\downarrow\downarrow\rangle,\\
&|\Psi_{13}\rangle = \frac{-i}{2}|\downarrow\downarrow\downarrow\uparrow\rangle + \frac{-1}{2}|\downarrow\downarrow\uparrow\downarrow\rangle + \frac{i}{2}|\downarrow\uparrow\downarrow\downarrow\rangle + \frac{1}{2}|\uparrow\downarrow\downarrow\downarrow\rangle,\\
&|\Psi_{14}\rangle = \frac{1}{2}|\downarrow\downarrow\downarrow\uparrow\rangle + \frac{1}{2}|\downarrow\downarrow\uparrow\downarrow\rangle + \frac{1}{2}|\downarrow\uparrow\downarrow\downarrow\rangle + \frac{1}{2}|\uparrow\downarrow\downarrow\downarrow\rangle,\\
&|\Psi_{15}\rangle = \frac{1}{2}|\downarrow\downarrow\downarrow\uparrow\rangle + \frac{-1}{2}|\downarrow\downarrow\uparrow\downarrow\rangle + \frac{1}{2}|\downarrow\uparrow\downarrow\downarrow\rangle + \frac{-1}{2}|\uparrow\downarrow\downarrow\downarrow\rangle,\\
&|\Psi_{16}\rangle = |\downarrow\downarrow\downarrow\downarrow\rangle.
\end{aligned}
\tag{A.1}
$$

Here

$$\begin{aligned}
C_1 &= \left\{1 + \left(\frac{-J_1 - 2J_2 + \sqrt{4A^2 + J_1^2 + 16J_2^2 - 8J_1J_2 + 8\wp^2}}{2A}\right)^2\right\}^{-1/2}, \\
C_2 &= \left\{1 + \left(\frac{-J_1 - 2J_2 - \sqrt{4A^2 + J_1^2 + 16J_2^2 - 8J_1J_2 + 8\wp^2}}{2A}\right)^2\right\}^{-1/2}, \\
A &= \frac{4\dot{\wp}(\lambda + \mu)\alpha\gamma}{\wp(\lambda - \mu)}.
\end{aligned} \tag{A.2}$$

- Eigenvalues of the Hamiltonian $\hat{H}_{CD}(t)$

$$\begin{aligned}
&\Xi_1 = J_1 + J_2 - 2B, \Xi_2 = -J_2 - B - \wp, \Xi_3 = -J_2 - B + \wp, \\
&\Xi_4 = -J_1 + J_2 - B, \Xi_5 = J_1 + J_2 - B, \\
&\Xi_6 = \frac{-J_1 - 2J_2 + \sqrt{4A^2 + J_1^2 + 16J_2^2 - 8J_1J_2 + 8\wp^2}}{2}, \\
&\Xi_7 = \frac{-J_1 - 2J_2 - \sqrt{4A^2 + J_1^2 + 16J_2^2 - 8J_1J_2 + 8\wp^2}}{2}, \\
&\Xi_8 = J_1 + J_2, \Xi_9 = -2J_1 + J_2, \Xi_{10} = -J_2, \Xi_{11} = -J_2, \\
&\Xi_{12} = -J_2 + B + \wp, \Xi_{13} = -J_2 + B - \wp, \\
&\Xi_{14} = J_1 + J_2 + B, \Xi_{15} = -J_1 + J_2 + B, \Xi_{16} = J_1 + J_2 + 2B.
\end{aligned} \tag{A.3}$$

Since the electric field is time dependent i.e. $\wp(t)$, All parameters $\alpha, \gamma, \mu, \lambda, C_1, C_2, A$ are also time dependent.

Bibliography

[1] H. Schmid. Multiferroic magnetoelectrics. *Ferroelecrrics*, 162:317-338, 1994.

[2] D. Higashiyama, S. Miyasaka,N.Kida, T. Arima, and Y. Tokura. Control of the ferroelectric properties of $DyMn_2O_5$ by magnetic fields. *Phys. Rev. B*, 70:174405, 2004.

[3] H. Sagayama, K. Taniguchi, N. Abe, T. H. Arima, M. Soda, M. Matsuura, K. Hirota. Correlation between ferroelectric polarization and sense of helical spin order in multiferroic $MnWO_4$. *Phys. Rev. B*, 77:220407, 2008.

[4] M. Bibes and A. Barthélémy. Multiferroics: Towards a magnetoelectric memory. *Nat. Mater.*, 7:425-426, 2008.

[5] M. Gajek, M. Bibe, S. Fusil, K. Bouzehouane, J. Fontcuberta, A. Barthélémy, and A. Fert. Tunnel junctions with multiferroic barriers. *Nat. Mater.* 6:296-302, 2007.

[6] C.-L. Jia, and J. Berakdar. Multiferroic oxides-based flash memory and spin-field-effect transistor. *Appl. Phys. Lett.*, 95:012105, 2009.

[7] M. Azimi, L. Chotorlishvili, S. K. Mishra, S. Greschner, T. Vekua, and J. Berakdar. Helical multiferroics for electric field controlled quantum information processing. *Phys. Rev. B*, 89:024424, 2014.

[8] S. Seki, Y. Yamasaki, M. Soda, M. Matsuura, K. Hirota, and Y. Tokura. Correlation between Spin Helicity and an Electric Polarization Vector in Quantum-Spin Chain Magnet $LiCu_2O_2$. *Phys. Rev. Lett.*, 100:127201, 2008.

[9] G. De Chiara, D. Rossini, S. Montangero, and R. Fazio. From perfect to fractal transmission in spin chains. *Phys. Rev. A*, 72:012323, 2005.

[10] P. Karbach and J. Stolze. Spin chains as perfect quantum state mirrors. *Phys. Rev. A*, 72:030301(R), 2005.

[11] M. -H. Yung and S. Bose. Perfect state transfer, effective gates, and entanglement generation in engineered bosonic and fermionic networks. *Phys. Rev. A*, 71:032310, 2005.

[12] D. Burgarth and S. Bose. Perfect quantum state transfer with randomly coupled quantum chains. *New J. Phys.*, 7:135, 2005.

[13] P. Hänggi, F. Marchesoni, and F. Nori. Brownian motors. *Ann. Phys. (Leipzig)*, 14:51-70, 2005.

[14] T. E. Humphrey, R. Newbury, R. P. Taylor, and H. Linke. Reversible Quantum Brownian Heat Engines for Electrons. *Phys. Rev. Lett.*, 89:116801, 2002.

[15] P. Skrzypczyk, N. Brunner, N. Linden, and S. Popescu. The smallest refrigerators can reach maximal efficiency. *J. Phys. A: Math. Theor.*, 44:492002, 2011.

[16] M. Campisi, P. Hänggi, and P. Talkner. Colloquium: Quantum fluctuation relations: Foundations and applications. *Rev. Mod. Phys.*, 83:771, 2011.

[17] M. Campisi1, R. Blattmann, S. Kohler, D. Zueco, and P. Hänggi. Employing circuit QED to measure non-equilibrium work fluctuations. *New J. Phys.*, 15:105028, 2013.

[18] S. N. Shevchenko, S. Ashhab, and F. Nori. LandauZenerStckelberg interferometry. *Phys. Rep.*, 492:1, 2010.

[19] R. Dillenschneider and E. Lutz. Energetics of quantum correlations. *Europhys. Lett.*, 88:50003, 2009.

[20] D. Khomskii. Classifying multiferroics: Mechanisms and effects. *Physics*, 2:20, 2009.

[21] W. C. Röntgen. Über die durch Bewegung eines im homogenen electrischen Felde befindlichen Dielektrikums hervorgerufene electrodynamische Kraft. *Ann. Phys. Chem*, 35:264-270, 1888.

[22] H. A. Wilson. On the electric effect of rotating dielectric in a magnetic field. *Phil. Trans. R. Soc. A*, 204:121-137, 1905

[23] P. Curie. First consideration of an intrinsic correlation of magnetic and electric properties in a solid. *J. de Physique(3rd series)*, 3:393-415, 1894.

[24] L. D. Landau and E. M. Lifshitz. *Electrodynamics of Continuous Media.* Oxford: Pergamon Press, 1960.

[25] I. E. Dzyaloshinskii. On the magneto-electrical effect in antiferromagnets. *J. Exptl. Theoret. Phys.(USSR)*, 37:881-882, 1959. [English transl.: *Sov. phys. JETP*, 10:628-629, 1960.]

[26] D. N. Astrov. The magnetoelectric effect in antiferromagnetics. *Sov. Phys. JETP*, 11:708-709, 1960.

[27] T. H. O'Dell. *The Electrodynamics of Magneto-Electric Media.* Amsterdam: North-Holland Publishing Co., 1970.

[28] N. A. Hill. Why are there so few magnetic ferroelectrics. *J. Phys. Chem. B*, 104:6694-6709, 2000.

[29] T. Kimura, T. Goto, H. Shintani, K. Ishizaka, T. Arima, and Y. Tokura. Magnetic control of ferroelectric polarization. *Nature*, 426:55-58, 2003.

[30] N. Hur, S. Park, P. A. Sharma, J. S. Ahn, S. Guha, and S. W. Cheong. Electric polarization reversal and memory in a multiferroic material induced by magnetic fields. *Nature*, 429:392-395, 2004.

[31] B. B. Van Aken, T. T. M. Palstra, A. Filippetti, and N. A. Spaldin. The origin of ferroelectricity in magnetoelectric $YMnO_3$. *Nat. Mater.*, 3:164-170, 2004.

[32] G. Lawes, A. B. Harris, T. Kimura, N. Rogado, R. J. Cava, A. Aharony, O. Entin-Wohlman, T. Yildirim, M. Kenzelmann, C. Broholm, and A. P. Ramirez. Magnetically driven ferroelectric order in $Ni_3V_2O_8$. *Phys. Rev. Lett.*, 95:1-4, 2005.

[33] M. Fiebig. Revival of the magnetoelectric effect. *J. Phys. D: Appl. Phys.*, 38:123-152, 2005.

[34] W. Ehrenstein, N. D. Mathur, and J. F. Scott. Multiferroic and magnetoelectric materials. *Nature*, 442:759-765, 2006.

[35] S. W. Cheong and M. Mostovoy. Multiferroics: a magnetic twist for ferroelectricity. *Nat. Mater.*, 6:13-20, 2007.

[36] H. Schmid. Some symmetry aspects of ferroics and single phase multiferroic. *J. Phys.: Condens. Matter*, 20:434201-434220, 2008.

[37] D. I. Khomskii. Multiferroics: Different ways to combine magnetism and ferroelectricity. *J. Magn. Magn. Mater.*, 306:1-8, 2006.

[38] R. E. Cohen. Origin of ferroelectricity in perovskite oxides. *Nature*, 358:136-138, 1992.

[39] R. Seshadri and N. A. Hill. Visualizing the role of Bi 6*s* "Lone Pairs" in the off center distortion in ferromagnetic $BiMnO_3$. *Chemistry of Materials*, 13:2892-2899, 2001.

[40] J. Neaton, C. Ederer, U. Waghmare, N. Spaldin, and K. Rabe. First-principles study of spontaneous polarization in multiferroic $BiFeO_3$. *Physical Review B*, 71:014113, 2005.

[41] R. E. Cohen and H. Krakauer. Electronic structure studies of the differences in ferroelectric behavior of $BaTiO_3$ and $PbTiO_3$. *Ferroelectrics*, 136:65-83, 1992.

[42] K. Uusi-Esko, J. Malm, N. Imamura, H. Yamauchi, and M. Karppinen. Characterization of $RMnO_3$ (R = Sc, Y, Dy-Lu): High-pressure synthesized metastable perovskites and their hexagonal precursor phases. *Materials Chemistry and Physics*, 112:1029-1034, 2008.

[43] T. Choi, Y. Horibe, H. T. Yi, Y. J. Choi, W. Wu, and S. W. Cheong. Insulating interlocked ferroelectric and structural antiphase domain walls in multiferroic $YMnO_3$. *Nat. Mater.*, 9:253-258, 2010.

[44] K. F. Wang, J. M. Liu, and Z. F. Ren. Multiferroicity: the coupling between magnetic and polarization orders. *Advances in Physics*, 58:321-448, 2009.

[45] M. Kenzelman, A. B. Harris, S. Jonas, C. Broholm, J. Schefer, S. B. Kim, C. L. Zhang, S.-W. Cheong, O. P. Vajk, and J.W. Lynn. Magnetic Inversion Symmetry Breaking and Ferroelectricity in $TbMnO_3$. *Phys. Rev. Lett.*, 95:087206, 2005.

[46] T. Kimura, G. Lawes, T. Goto, Y. Tokura, and A. P. Ramirez. Magnetoelectric phase diagrams of orthorhombic MnO_3 (R=Gd, Tb, and Dy). *Phys. Rev. B*, 71:224425, 2005.

[47] T. Kimura, J. C. Lashley, and A. P. Ramirez. Inversion-symmetry breaking in the noncollinear magnetic phase of the triangular-lattice antiferromagnet $CuFeO_2$. *Phys. Rev. B*, 73:220401(R), 2006.

[48] K. Taniguchi, N. Abe, T. Takenobu, Y. Iwasa, and T. Arima. Ferroelectric Polarization Flop in a Frustrated Magnet $MnWO_4$ Induced by a Magnetic Field. *Phys. Rev. Lett.*, 97:097203, 2006.

[49] T. Kimura, Y. Sekio, H. Nakamura, T. Siegrist, and A. P. Ramirez. Cupric oxide as an induced-multiferroic with high-T_C. *Nat. Mater.*, 7:291-294, 2008.

[50] T. Kimura, S. Ishihara, H. Shintani, T. Arima, K. T. Takahashi, K. Ishizaka, and Y. Tokura. Distorted perovskite with e_g^1 configuration as a frustrated spin system. *Phys. Rev. B*, 68:060403(R), 2003.

[51] Y. J. Choi, H. T. Yi, S. Lee, Q. Huang, V. Kiryukhin, and S.-W. Cheong. Ferroelectricity in an Ising Chain Magnet. *Phys. Rev. Lett.*, 100:047601, 2008.

[52] H. Katsura, N. Nagaosa, and A. V. Balatsky. Spin Current and Magnetoelectric Effect in Noncollinear Magnets. *Phys. Rev. Lett.*, 95:057205, 2005.

[53] M. Mostovoy. Ferroelectricity in Spiral Magnets. *Phys. Rev. Lett.*, 96:067601, 2006.

[54] I. A. Sergienko and E. Dagotto. Role of the dzyaloshinskii-moriya interaction in multiferroic perovskites. *Phys. Rev. B*, 73:094434, 2006.

[55] V. G. Baryachtar, V. A Lvov, and D. A. Jablonskii. Theory of inhomogeneous magnetoelectric effect. *JETP Lett.*, 37:673, 1983.

[56] A. A. Gippius, E. N. Morozova, A. S. Moskvin, A. V. Zalessky, A. A. Bush, M. Baenitz, H. Rosner, and S.-L. Drechsler. NMR and local-density-approximation evidence for spiral magnetic order in the chain cuprate $LiCu_2O_2$. *Phys. Rev. B*, 70:020406(R), 2004.

[57] T. Masuda, A. Zheludev, A. Bush, M. Markina, and A. Vasiliev. Competition between Helimagnetism and Commensurate Quantum Spin Correlations in $LiCu_2O_2$. *Phys. Rev. Lett.*, 92:177201, 2004.

[58] T. Masuda, A. Zheludev, B. Roessli, A. Bush, M. Markina, and A. Vasiliev. Spin waves and magnetic interactions in $LiCu_2O_2$. *Phys. Rev. B*, 72:014405, 2005.

[59] L. Mihály, B. Dóra, A. Ványolos, H. Berger, and L. Forró. Spin-Lattice Interaction in the Quasi-One-Dimensional Helimagnet $LiCu_2O_2$. *Phys. Rev. Lett.*, 97:067206, 2006.

[60] S. Park, Y. J. Choi, C. L. Zhang, and S-W. Cheong. Ferroelectricity in an $S = 1/2$ Chain Cuprate. *Phys. Rev. Lett.*, 98:057601, 2007.

[61] L. Zhao, K.-W. Yeh, S. Muralidhara Rao, T.-W. Huang, P. Wu, W.-H. Chao, C.-T. Ke, C.-E. Wu and M.-K. Wu. Anisotropic dielectric and ferroelectric response of multiferroic $LiCu_2O_2$ in magnetic field. *EPL*, 97:37004, 2012.

[62] M. N. Nielsen and I. L. Chuang. *Quantum Computation and Quantum Information.* Cambridge University Press, Cambridge, England, 2000.

[63] S. Bose. Quantum Communication through an Unmodulated Spin Chain. *Phys. Rev. Lett*, 91:207901, 2003.

[64] M. Christandl, N. Datta, A. Ekert, and A. J. Landahl. Perfect State Transfer in Quantum Spin Networks. *Phys. Rev. Lett*, 92:187902, 2004.

[65] M. B. Plenio, J. Hartley, and J. Eisert. Dynamics and manipulation of entanglement in coupled harmonic systems with many degrees of freedom. *New J. Phys.*, 6:36, 2004.

[66] D. Burgarth and S. Bose. Conclusive and arbitrarily perfect quantum-state transfer using parallel spin-chain channels. *Phys. Rev. A*, 71:052315, 2005.

[67] M. Christandl, N. Datta, T. C. Dorlas, A. Ekert, A. Kay, and A. J. Landahl. Perfect transfer of arbitrary states in quantum spin networks. *Phys. Rev. A*, 71:032312, 2005.

[68] T. Shi, Y. Li, Z. Song, and C. P. Sun. Quantum-state transfer via the ferromagnetic chain in a spatially modulated field. *Phys. Rev. A*, 71:032309, 2005.

[69] S. Yang, Z. Song, and C. P. Sun. Wave-packet transmission of Bloch electrons manipulated by magnetic field. *Phys. Rev. A*, 73:022317, 2006.

[70] G. Vidal, J. I. Latorre, E. Rico, and A. Kitaev. Entanglement in Quantum Critical Phenomena. *Phys. Rev. Lett*, 90:227902, 2003.

[71] L. Amico, A. Osterloh, F. Plastina, R. Fazio, and G. M. Palma. Dynamics of entanglement in one-dimensional spin systems. *Phys. Rev. A*, 69:022304, 2004.

[72] F. Verstraete, M. Popp, and J. I. Cirac. Entanglement versus Correlations in Spin Systems. *Phys. Rev. Lett*, 92:027901, 2004.

[73] P. Zanardi and N. Paunković. Ground state overlap and quantum phase transitions. *Phys. Rev. E*, 74:031123, 2006.

[74] W.L. You, Y. W. Li, and S. J. Gu. Fidelity, dynamic structure factor, and susceptibility in critical phenomena. *Phys. Rev. E*, 76:022101, 2007.

[75] L. Wang, Y.H. Liu, J. Imriška, P. N. Ma, and M. Troyer. Fidelity Susceptibility Made Simple: A Unified Quantum Monte Carlo Approach. *Phys. Rev. X*, 5:031007, 2015.

[76] M. A. Nilesen and I. L. Chuang. *Quantum Computation and Quantum Information.* Cambridge University Press, Cambridge, England, 2000.

[77] P. Zanardi, H. T. Quan, X. Wang, and C. P. Sun. Mixed-state fidelity and quantum criticality at finite temperature. *Phys. Rev. A*, 75:032109, 2007.

[78] N. Paunković, P. D. Sacramento, P. Nogueira, V. R. Vieira, and V. K. Dugaev. Fidelity between partial states as a signature of quantum phase transitions. *Phys. Rev. A*, 77:052302, 2008.

[79] D. Deutsch. *Quantum computational networks.* Proc. R. Soc. Lond. A 425, 1989.

[80] C. H. Bennet and G. Brassard. Quantum cryptography: public key distribution and coin tossing. *Proceedings of IEEE International Conference on Computers, Systems and Signal Processing*, 1984.

[81] C. H. Bennett and S. J. Wiesner. Communication via one-and two-particle operators on Einstein-Podolsky-Rosen states. *Phys. Rev. Lett.*, 69:2881-2884, 1992.

[82] C. H. Bennett, G. Brassard, C. Crépeau, R. Jozsa, A. Peres, and W.K.Wootters. Teleporting an unknown quantum state via dual classical and Einstein-Podolsky-Rosen channels. *Phys. Rev. Lett.*, 70:1895-1899, 1993.

[83] W.K. Wootters. Entanglement of Formation of an Arbitrary State of Two Qubits. *Phys. Rev. Lett.*, 80:2245, 1998.

[84] F. Mintert, A. R.R. Carvalhoa, M. Kuś, A. Buchleitnera. Measures and dynamics of entangled states. *Phys. Rep.*, 415:207, 2005.

[85] L. Amico, R. Fazio, A. Osterloh, and V. Vedral. Entanglement in many-body systems. *Rev. Mod. Phys.*, 80:517, 2008.

[86] V. C. Usenko, B. Heim, C. Peuntinger, C. Wittmann, C. Marquardt, G. Leuchs, and R. Filip. Entanglement of Gaussian states and the applicability to quantum key distribution over fading channels. *New J. Phys.*, 14:093048, 2012.

[87] C. Peuntinger, V. Chille, L. Mišta, Jr., N. Korolkova, M. Förtsch, J. Korger, C. Marquardt, and G. Leuchs. Distributing Entanglement with Separable States. *Phys. Rev. Lett.*, 111:230506, 2013.

[88] F. Lucas, F. Mintert, and A. Buchleitner. Tailoring many-body entanglement through local control. *Phys. Rev. A*, 88:032306, 2013.

[89] V. Coffman, J. Kundu, and W. K. Wootters. Distributed entanglement. *Phys. Rev. A* 61:052306, 2000.

[90] T. Roscilde, P. Verrucchi, A. Fubini, S. Haas, and V. Tognetti. Studying Quantum Spin Systems through Entanglement Estimators. *Phys. Rev. Lett.*, 93:167203, 2004.

[91] M. J. Henrich, G. Mahler, and M. Michel. Driven Spin Systems as Quantum Thermodynamic Machines: Fundamental Limits. *Phys. Rev. E*, 75:051118, 2007.

[92] H. T. Quan, Y. D. Wang, Yu-xi Liu, C. P. Sun, and Franco Nori. Maxwells Demon Assisted Thermodynamic Cycle in Superconducting Quantum Circuits. *Phys. Rev. Lett*, 97:180402, 2006.

[93] H. T. Quan, Yu-xi Liu, C. P. Sun, and F. Nori. Quantum thermodynamic cycles and quantum heat engines. *Phys. Rev. E*, 76:031105, 2007.

[94] H. T. Quan and F. M. Cucchietti. Quantum fidelity and thermal phase transitions. *Phys. Rev. E*, 79:031101, 2009.

[95] N. Linden, S. Popescu, and P. Skrzypczyk. How small can thermal machines be? The smallest possible refrigerator. *Phys. Rev. Lett.*, 105:130401, 2010.

[96] O. Abah, J. Ronagel, G. Jacob, S. Deffner, F. Schmidt-Kaler, K. Singer, and E. Lutz. Single-Ion Heat Engine at Maximum Power. *Phys. Rev. Lett.*, 109:203006, 2012.

[97] R. Wang, J. Wang, J. He, and Y. Ma. Performance of a multilevel quantum heat engine of an ideal N-particle Fermi system. *Phys. Rev. E*, 86:021133, 2012.

[98] H. Wang and G. Wu. Performance analysis and optimum criteria of a quantum dot engine with two discrete energy levels. *Phys. Lett. A*, 376:2209, 2012.

[99] H. Wang. Chiral anomaly, charge density waves, and axion strings from Weyl semimetals. *Phys. Scr.*, 87:055009, 2013.

[100] J. Wang, Y. Ma, and J. He. Quantum-mechanical engines working with an ideal gas with a finite number of particles confined in a power-law trap. *EPL*, 111:20006, 2015.

[101] M. Born and V. Fock. Beweis des adiabatensatzes. *Z. Phys.*, 51:165, 1928.

[102] D. J. Griffiths. *Introduction to Quantum Mechanics.* Prentice Hall, 1995.

[103] T. Kato. On the adiabatic theorem of quantum mechanics. *Journal of the Physical Society of Japan*, 5(6):435, 1950.

[104] T. Kubacka, J. A. Johnson, M. C. Hoffmann, C. Vicario, S. de Jong, P. Beaud, S. Grübel, S.-W. Huang, L. Huber, L. Patthey, Y.-D. Chuang, J. J. Turner, G. L. Dakovski, W.-S. Lee, M. P. Minitti, W. Schlotter, R. G. Moore, C. P. Hauri, S. M. Koohpayeh, V. Scagnoli, G. Ingold, S. L. Johnson, and U. Staub. Large-Amplitude Spin Dynamics Driven by a THz Pulse in Resonance with an Electromagnon. *Science*, 343: 1333-1336, 2014.

[105] M. Azimi, M. Sekania, S. K. Mishra, L. Chotorlishvili, Z. Toklikishvili, and J. Berakdar. Pulse and quench induced dynamical phase transition in a chiral multiferroic spin chain. *Phys. Rev B*, 94:064423, 2016.

[106] M. Heyl, A. Polkovnikov, and S. Kehrein. Dynamical Quantum Phase Transitions in the Transverse-Field Ising Model. *Phys. Rev. Lett.*, 110:135704, 2013.

[107] C. Karrasch and D. Schuricht. Dynamical phase transitions after quenches in nonintegrable models. *Phys. Rev. B*, 87:195104, 2013.

[108] S. Vajna and B. Dóra. Disentangling dynamical phase transitions from equilibrium phase transitions. *Phys. Rev. B*, 89:161105, 2014.

[109] J. M. Hickey, S. Genway, and J. P. Garrahan. Dynamical phase transitions, time-integrated observables, and geometry of states. *Phys. Rev. B*, 89:054301, 2014.

[110] E. Canovi, E. Ercolessi, P. Naldesi, L. Taddia, and D. Vodola. Dynamics of entanglement entropy and entanglement spectrum crossing a quantum phase transition. *Phys. Rev. B*, 89:104303, 2014.

[111] E. Canovi, P. Werner, and M. Eckstein. First-Order Dynamical Phase Transitions. *Phys. Rev. Lett.*, 113:265702, 2014.

[112] G. Torlai, L. Tagliacozzo, and G. De Chiara. Dynamics of the entanglement spectrum in spin chains. *J. Stat. Mech.*, P06001, 2014.

[113] A. Bayat, H. Johannesson, S. Bose, and P. Sodano. An order parameter for impurity systems at quantum criticality. *Nature Communications*, 5:3784, 2014.

[114] Q. Hu, S. Yin, and F. Zhong. Scaling of the entanglement spectrum in driven critical dynamics. *Phys. Rev. B*, 91:184109, 2015.

[115] J. Eisert, M. Cramer, and M. B. Plenio. Colloquium: Area laws for the entanglement entropy. *Rev. Mod. Phys.*, 82:277-306, 2010.

[116] H. Li and F. D. M. Haldane. Entanglement Spectrum as a Generalization of Entanglement Entropy: Identification of Topological Order in Non-Abelian Fractional Quantum Hall Effect States. *Phys. Rev. Lett.*, 101:010504, 2008.

[117] G. De Chiara, L. Lepori, M. Lewenstein, and A. Sanpera. Entanglement Spectrum, Critical Exponents, and Order Parameters in Quantum Spin Chains. *Phys. Rev. Lett.*, 109:237208, 2012.

[118] M. Azimi, L. Chotorlishvili, S. K. Mishra, T. Vekua, W. Hübner, and J. Berakdar. Quantum Otto heat engine based on a multiferroic chain working substance. *New J. Phys.*, 16:063018, 2014.

[119] L. Lepori, G. De Chiara, and A. Sanpera. Scaling of the entanglement spectrum near quantum phase transitions. *Phys. Rev. B*, 87:235107, 2013.

[120] A. Chandran, V. Khemani, and S. L. Sondhi. How Universal Is the Entanglement Spectrum? *Phys. Rev. Lett.*, 113:060501, 2014.

[121] L. D. Landau and E. M. Lifshitz. *A Course of Theoretical Physics Statistical Physics*. Oxford: Pergamon Press, 1969.

[122] F. Heidrich-Meisner, A. Honecker, and T. Vekua. Frustrated ferromagnetic spin-$\frac{1}{2}$ chain in a magnetic field: The phase diagram and thermodynamic properties. *Phys. Rev. B*, 74:020403(R), 2006.

[123] M. Demirplak and S. A. Rice. Adiabatic Population Transfer with Control Fields. *J. Phys. Chem. A*, 107:9937-9945, 2003.

[124] M. Demirplak and S. A. Rice. Assisted Adiabatic Passage Revisited. *J. Phys. Chem. B*, 109:6838-6844, 2005.

[125] M. V. Berry, *J. Phys. A: Math. Theor.*, 42:365303, 2009.

[126] M. Esposito, R. Kawai, K. Lindenberg, and C. Van den Broeck. Quantum-dot Carnot engine at maximum power. *Phys. Rev. E*, 81:041106, 2010.

[127] A. del Campo, J. Goold, and M. Paternostro. More bang for your buck: Towards super-adiabatic quantum engines. *Sci. Rep.*, 4:6208, 2014.

[128] E. A. Ivanchenko. Quantum Otto cycle efficiency on coupled qudits. *Phys. Rev. E*, 92:032124, 2015.

[129] A. Alecce, F. Galve, N. Lo. Gullo, L. Dell'Anna, F. Plastina, and R. Zambrini. Quantum Otto cycle with inner friction: finite-time and disorder effects. *New J. Phys.*, 17:075007, 2015.

[130] P. Talkner, E. Lutz, and P. Hänggi. Fluctuation theorems: Work is not an observable. *Phys. Rev. E*, 75:050102(R), 2007.

[131] S. Deffner and E. Lutz. Generalized Clausius Inequality for Nonequilibrium Quantum Processes. *Phys. Rev. Lett.*, 105:170402, 2010.

[132] C. Jarzynski. Generating shortcuts to adiabaticity in quantum and classical dynamics. *Phys. Rev. A*, 88:040101(R), 2013.

[133] A. del Campo. Shortcuts to Adiabaticity by Counterdiabatic Driving. *Phys. Rev. Lett.*, 111:100502, 2013.

[134] C. Jarzynski. Nonequilibrium Equality for Free Energy Differences. *Phys. Rev. Lett.*, 78:2690, 1997.

List of Publications

1. Maryam Azimi, Levan Chotorlishvili, Sunil Kumar Mishra, Sebastian Greschner, Teimuraz Vekua, and Jamal Berakdar. *Helical multiferroics for electric field controlled quantum information processing.* Phys. Rev. B **89**, 024424 (2014).
2. Maryam Azimi, Levan Chotorlishvili, Sunil Kumar Mishra, Teimuraz Vekua, Wolfgang Hübner, and Jamal Berakdar. *Quantum Otto heat engine based on a multiferroic chain working substance.* New Journal of Physics **16**, 063018 (2014).
3. Maryam Azimi, Michael Sekania, Sunil Kumar Mishra, Levan Chotorlishvili, Zaza Toklikishvili, and Jamal Berakdar. *Pulse and quench induced dynamical phase transition in a chiral multiferroic spin chain.* Phys. Rev B **94**, 064423 (2016).
4. Levan Chotorlishvili, Maryam Azimi, Stefan Stagraczyński, Zaza Toklikishvili, Michael Schüler, and Jamal Berakdar. *Superadiabatic quantum heat engine with a multiferroic working medium.* Phys. Rev. E **94**, 032116 (2016).

Earlier published papers:

5. Mohamad Ali Jafarizadeh, Rahime Sufiani, Maryam Azimi, and Faghiheh Eghbali Fam. *Perfect state transfer over interacting boson networks associated with group schemes.* Quantum Information Processing **11**, 171-187 (2011).
6. Mohamad Ali Jafarizadeh, Rahime Sufiani, Seyyed Farid Taghavi, Ehsan Barati, Faghiheh Eghbali Fam, and Maryam Azimi. *Generating a GHZ state in 2m-qubit spin network.* Journal of Statistical Mechanics: Theory and Experiment **05**, P05014 (2011).

Presentations

1. 6th European School on Multiferroics (ESMF6), (21-26 July 2013):*Quantum information processing in 1-D Multiferroic chain.* (Poster), Wittenberg, Germany.
2. Joint IMPRS/SFB Workshop on Nanoscience and -technology (30 September-02 October 2013): *Sensitivity of quantum information processing and quantum phase transitions in 1D multiferroic chain to electric field.* (Poster), Halle, Germany.
3. Collaborative Research Centre SFB 762: Functionality of Oxide Interfaces, (10-14 March 2014): *Operating of quantum heat engine with multiferroic chain working substance.* (Poster), Irsee/Augsburg, Germany.
4. DPG Spring Meeting, (30 March-04 April 2014): *Quantum heat engine operating with multiferroic chain working substance.* (Poster), Dresden, Germany.
5. DPG Spring Meeting, (15-20 March 2015): *Quantum information processing based on multiferroic helical spin chain.* (Poster), Berlin, Germany.
6. The European school on magnetism, (24 August-04 September 2015): *Quantum information processing in multiferroic spiral spin chain.* (Poster), Cluj-Napoca, Romania.

Eidesstattliche Erklärung

Hiermit erkläre ich gemäß §5 Abs. 2b der Promotionsordnung der Naturwissenschaftlichen Fakultät II der Martin-Luther-Universität Halle-Wittenberg vom 13.06.2012, dass ich die vorliegende Arbeit

Quantum dynamics and quantum information processing based on helical multiferroics

selbständig und ohne fremde Hilfe verfasst, sowie keine anderen als die von mir angegebenen Quellen und Hilfsmittel verwendet und die den verwendeten Werken wörtlich oder inhaltlich entnommenen Stellen als solche kenntlich gemacht habe. Weiterhin erkläre ich die Angaben wahrheitsgemäß gemacht und die vorliegende Dissertation in gleicher oder ähnlicher Form bisher bei keiner anderen wissenschaftlichen Einrichtung zur Erlangung des Doktorgrades eingereicht sowie keine vorherigen Promotionsversuche unternommen zu haben.

Halle(Saale), den 02. August 2016

Maryam Azimi

Acknowledgments

This dissertation would not have been possible without the guidance and the help of several individuals.

First and foremost, my sincere appreciation to my supervisor, Prof. Dr. Jamal Berakdar, for his continual assistance throughout my Ph.D.

I would like to acknowledge the enormous support and invaluable advices of Dr. Levan Chotorlishvili, and I am indebted to him.

I am extremely grateful to all our current and former group members, Stefan Stagraczyński, Michael Schüler, Dr. Alexander Sukhov, Dr. Yaroslav Pavlyukh, Seyyed Ruhollah Etesami and Jonas Wätzel, for the useful discussions and technical helps.

I would like to thank Dr. Sunil Kumar Mishra, Prof. Wolfgang Hübner, Dr. Teimuraz Vekua and Dr. Michael Sekania, for great collaborations.

I sincerely thank Dr. Arthur Ernst, International Max Planck Research School (IMPRS) coordinator and Prof. Dr. Eberhard Gross, director of Max Planck Institute of Microstructure Physics (MPI), Halle (Germany).

I also heartily thank Ina Goffin, secretary of MPI for her kind help in all administrative related issues.

I am very thankful for my parents, brother, sister and my husband, for their constant motivation and spiritually support.

Curriculum Vitae

Personal information:

Last name: Azimi

First name: Maryam

Date of birth: 21.09.1985

Place of birth: Marand-Iran

Nationality: Iranian

Gender: Female

Address: Institut für Physik, Karl-Freiherr-von-Fritsch Str. 3,
06120-Halle, Germany

Telephone: 0049 345 5528526

Fax: 0049 345 5527114

Email: mazimi@mpi-halle.mpg.de

Education:

1999-2003: High School Diploma in Mathematics and Physics, Bagherolulum Nemune Dolati Heighschool, Tabriz, Iran

2003-2007: Bachelor of Science, Solid State Physics, University of Tabriz, Tabriz, Iran

2008-2011: Master of Science, Theoretical Physics, University of Tabriz, Tabriz, Iran

2012-2016: Doctor rerum naturalium (Expected degree), International Max Planck Research School for Science and Thechnology of Nanostructures and Martin-Luther Universität Halle-Wittenberg, Halle, Germany

Halle (Saale), 02 August 2016

Maryam Azimi